MOLECULAR BEAM CHEMISTRY OF ALKALINE EARTH ATOMS

Charles Arthur Mims
(Ph. D. Thesis)

May 1973

Prepared for the U. S. Atomic Energy Commission
under Contract W-7405-ENG-48

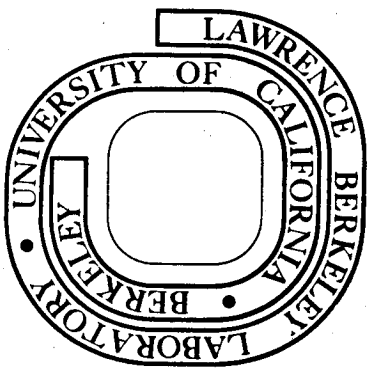

LBL-1159
c.1

DISCLAIMER

MOLECULAR BEAM CHEMISTRY OF ALKALINE EARTH ATOMS

Charles Arthur Mims

Inorganic Materials Research Division, Lawrence Berkeley Laboratory
and Department of Chemistry; University of California,
Berkeley, California

ABSTRACT

An apparatus has been constructed for measuring laboratory (LAB) angular distributions of reactively scattered products from crossed neutral molecular beams. Products are detected by electron bombardment ionization and subsequent mass analysis. The reactions of the alkaline earth (Group IIA) metals with HI, ICl, BrCN, SF_6, $SnCl_4$, PCl_3, NO_2, and SO_2 have been studied. In all but the HI reactions, product center of mass (CM) recoil energy and angular distributions have been fit to the measured LAB distributions by averaging over the measured (non-thermal) beam velocity distributions.

Kinematic restraints in the HI reactions which preclude determination of CM scattering behavior allow the measurement of the premium which the reaction places on incident relative kinetic energy.

The chemical behaviors evidenced in the CM distributions of the other reactions share similarities to and interesting differences from those of the analogous alkali metal reactions. There is evidence in the mixed halogen reaction that the reactive collisions sample the deep chemical well due to the stability of the alkaline earth dihalides. Observed CM behavior in the remaining reactions ranges from forward scattering for NO_2 and SO_2 to that predicted from intermediate complex formation for SF_6.

I. INTRODUCTION

Since the first measurement of a product angular distribution in a crossed molecular beam experiment,[1] understanding of the molecular dynamics of chemical reactions has increased dramatically.[2] A large variety of chemical behavior has been observed in the reactive differential cross sections that have been measured.

The earlier studies and the majority of neutral-neutral scattering experiments have been confined to the reactions of alkali metals because of the ease of detection of alkalis and their salts by positive surface ionization.[1] Therefore, a large variety of alkali metal reactions have been observed and are well understood. Most are pictured as proceding by transfer of an electron from the easily ionizable alkali to any electrophilic reaction partner at rather large reactant separations. The subsequent dynamical behavior is usually correlated with the electronic structure of the negative ion.[3]

Molecular beam studies of alkali metal reactions are still being purused vigorously, but, with the development of sensitive "universal" molecular beam detectors,[4] the technique has now been applied to many other reactive systems. Reaction dynamics of H atoms,[5] halogen atoms,[6] oxygen atoms,[7] and polyatomic free radicals[8] have been studied. Within certain practical experimental limitations, any bimolecular reaction of interest can now be studied by the molecular beam experimentalist.

With the entire periodic chart theoretically at one's disposal, why choose to study alkaline earth atom reactions? The answer lies in

the potential similarities to and differences from the well studied alkali metal reactions. The ionization potential of Ba is low (5.2 eV), and many of its reactions thus should be initiated by an electron transfer mechanism similar to that of alkali metal reactions. The lighter alkaline earth metals have higher ionization potentials (7.6 eV for Mg), and, as one progresses up the group, the simple electron transfer picture becomes less and less realistic. This change from ionic to more covalent behavior could be reflected in the reaction dynamics.

Moreover, the fact that the group IIA metals are divalent introduces other interesting possibilities. A deep chemical well in the potential hypersurface exists for M + halogen reactions by virtue of the stability of the alkaline earth dihalides. The extent to which this well influences the scattering should be of interest to people doing Monte Carlo trajectory studies. This divalent nature also raises the possibility of extraction of two halogens from polyhalides, and so on.

It should also be mentioned that the mass spectrometric situation is quite favorable when the product being detected is an alkaline earth monohalide. Electron bombardment of MX (X = halogen) produces mostly MX^+.[9] Furthermore, there should be little dependence of the cracking pattern or ionization efficiency on MX vibrational state due to very favorable placement of the MX^+ potential curve.[10]

Conventional studies of alkaline earth reactions have been confined mostly to heterogeneous systems[11] so that very little data on their gas phase kinetics is available. Recent interest in these

reactions, however, has prompted molecular beam,[12-16] chemiluminescence,[17] and laser induced fluorescence[18] studies of these reactions. The results of these studies and subsequent ones should provide instructive comparisons to and extensions of the theories which have been used to explain the dynamics of alkali metal reactions.

References

1. E. H. Taylor and S. Datz, J. Chem. Phys. 23, 1711 (1955).
2. For a recent review of progress in molecular beam kinetics, see J. L. Kinsey, Ch. 6, MTP International Review of Science, Phys. Chem. Series One, Vol. 9, Chemical Kinetics (Butterworth's, London, 1972).
3. D. R. Herschbach has probably been the leader in emphasizing this correlation with electronic structure. For examples, see: D. R. Herschbach, Adv. Chem. Phys. 10, 3191 (1966); R. Grice, M. R. Cosandey, and D. R. Herschbach, Ber. Bunsenges. Phys. Chem. 72, 975 (1968); and S. J. Riley and D. R. Herschbach, J. Chem. Phys. 58, 27 (1973).
4. Y. T. Lee, J. D. McDonald, P. R. LeBreton and D. R. Herschbach, Rev. Sci. Instr. 40, 1402 (1969).
5. a. J. P. McDonald, P. R. LeBreton, Y. T. Lee, and D. R. Herschbach, J. Chem. Phys. 56, 769 (1972).
   b. T. Geddes, H. F. Krause, and W. L. Fite, J. Chem. Phys. 52, 3296 (1970).
   c. J. Grosser and H. Haberland, Chem. Phys. Lett. 7, 442 (1970).
6. a. N. C. Blais and J. B. Cross, J. Chem. Phys. 52, 3580 (1970); J. Chem. Phys. 55, 3970 (1971).
   b. Y. T. Lee, J. D. McDonald, P. R. LeBreton, and D. R. Herschbach, J. Chem. Phys. 49, 2447 (1968); 51, 455 (1969).
   c. T. P. Schafer, P. E. Siska, J. M. Parson, F. P. Tully, Y. C. Wong and Y. T. Lee, J. Chem. Phys. 53, 3385 (1970).

d. D. Beck, F. Engelke, and J. H. Loesch, Ber. Bunsenges Phys. Chem. 72, 1105 (1968).

7. a. D. D. Parrish, Harvard University, private communication.

b. P. L. Moore, P. N. Clough, and J. Geddes, Chem. Phys. Lett. 17, 608 (1972).

8. a. D. L. McFadden, Jr., F. Kalos, W. R. Gentry, and J. Ross, J. Chem. Phys. 57, 1351 (1972).

b. C. F. Carter, M. R. Levy and R. Grice, Chem. Phys. Lett. 17, 414 (1972).

9. D. L. Hildebrand, J. Chem. Phys. 48, 3657 (1968); 52, 5751 (1970).

10. W. H. Hamill, J. Chem. Phys. 56, 4191 (1972).

11. For example see, H. F. Sullivan and I. Glassman, Comb. Science and Tech. 4, 241 (1972) and references cited therein.

12. J. A. Haberman, K. G. Anlauf, R. B. Bernstein and F. J. Van Itallie, Chem. Phys. Lett. 16, 442 (1972).

13. C. Batalli-Cosmovici and K. W. Michel, Chem. Phys. Lett. 11, 245 (1971).

14. J. Fricke, B. Kim, and W. L. Fite, Abstracts of Papers of the 7th International Conference on the Physics of Electronic and Atomic Collisions (North Holland Publishing Company, Amsterdam, 1971), pp. 37-38.

15. F. Engelke, Universität Freiburg (private communication).

16. D. R. Herschbach, Harvard University (private communication).

17. a. Ch. Ottinger and R. N. Zare, Chem. Phys. Lett. 5, 243 (1970).

b. C. D. Jonah and R. N. Zare, Chem. Phys. Lett. 9, 65 (1971).

c. C. D. Jonah, R. N. Zare and Ch. Ottinger, J. Chem. Phys. 56, 263 (1972).

18. A. Schultz, H. W. Cruse, and R. N. Zare, J. Chem. Phys. 57, 1354 (1972).

II. APPARATUS AND EXPERIMENTAL CONSIDERATIONS

A. Introduction

The design and construction of this molecular beam scattering apparatus was begun five years ago. The apparatus gradually "evolved" into the configuration described in this chapter. The configuration, happily enough, is a working one, and the apparatus was used to collect the reactive scattering data presented in Chapters III, IV, and V of this thesis and in References 1, 2, and 3.

An electron bombardment ionizer-quadrupole mass filter "universal" detector is employed, although early in the evolution of the machine the possibility of using negative surface ionization detection was briefly investigated. An excellent discussion of the considerations involved in the construction of such a machine is in the literature.[4] Basically, one attempts to increase signal (as always), while reducing the background pressure of interfering species at the mass of the product. The means by which this was accomplished are detailed in the apparatus description which follows.

Theoretically, any bimolecular reaction of interest could be studied with this machine; but in practice, in its present configuration, it is less sensitive and versatile than other "supermachines" now extant and reactions with cross sections of less than 5-10 $Å^2$ can be studied only with great difficulty. The reasons for this inferiority are limitations in the beam sources, and size limitations on the configuration and amount of differential pumping available for the

detector. There are no provisions for velocity analysis of the product, so that the apparatus lends itself towards the systematic qualitative study of a class of reactions rather than the more detailed study of individual differential cross sections.

All work on this machine was done in collaboration with Shen-Maw Lin, and his thesis[1] contains detailed descriptions of parts of the apparatus. A list of mechanical and electrical drawings are listed in appendices A and B.

B. Vacuum System and Beam Sources

A schematic of the apparatus is shown in Fig. II-1, and Fig. II-2 presents a block diagram of the vacuum system. Figure II-3 shows the electronics associated with the beam sources. Since the beam sources and vacuum system are described in detail in Ref. 1, only a cursory description is given here. Table I gives the positions and geometries of the beam and detector slits, Table II lists typical operating conditions, and beam widths are indicated in Fig. II-1.

The apparatus consists of two large aluminum high vacuum chambers, bolted together by a common flange, and a third, stainless steel UHV chamber which houses the detector. The two aluminum chambers are pumped by 10" oil diffusion pumps and are lined with liquid nitrogen cooled walls for high speed pumping of condensible species. One chamber houses the high temperature oven which is the source of the alkaline earth atomic beam (beam 1) in the studies presented in Chapters III, IV, and V and References 1, 2 and 3. The source oven

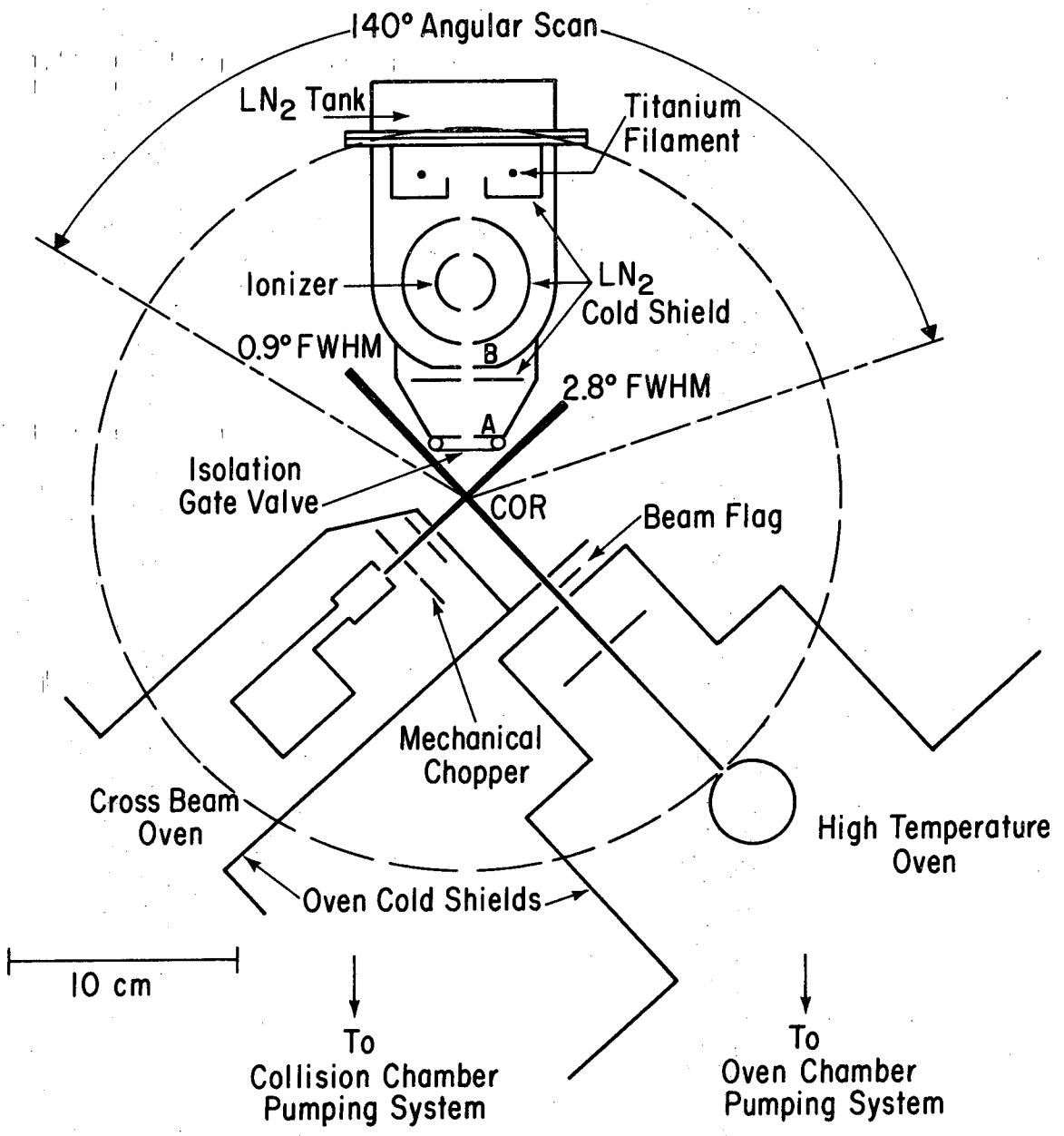

Fig. II-1. Schematic of the apparatus, viewed from above. The Laboratory (LAB) angle Θ is defined as 0° along the high temperature beam (beam 1) and 90° along the gas beam. The oven assemblies are stationary, and the detector can scan a range of Θ from -20° to 120°.

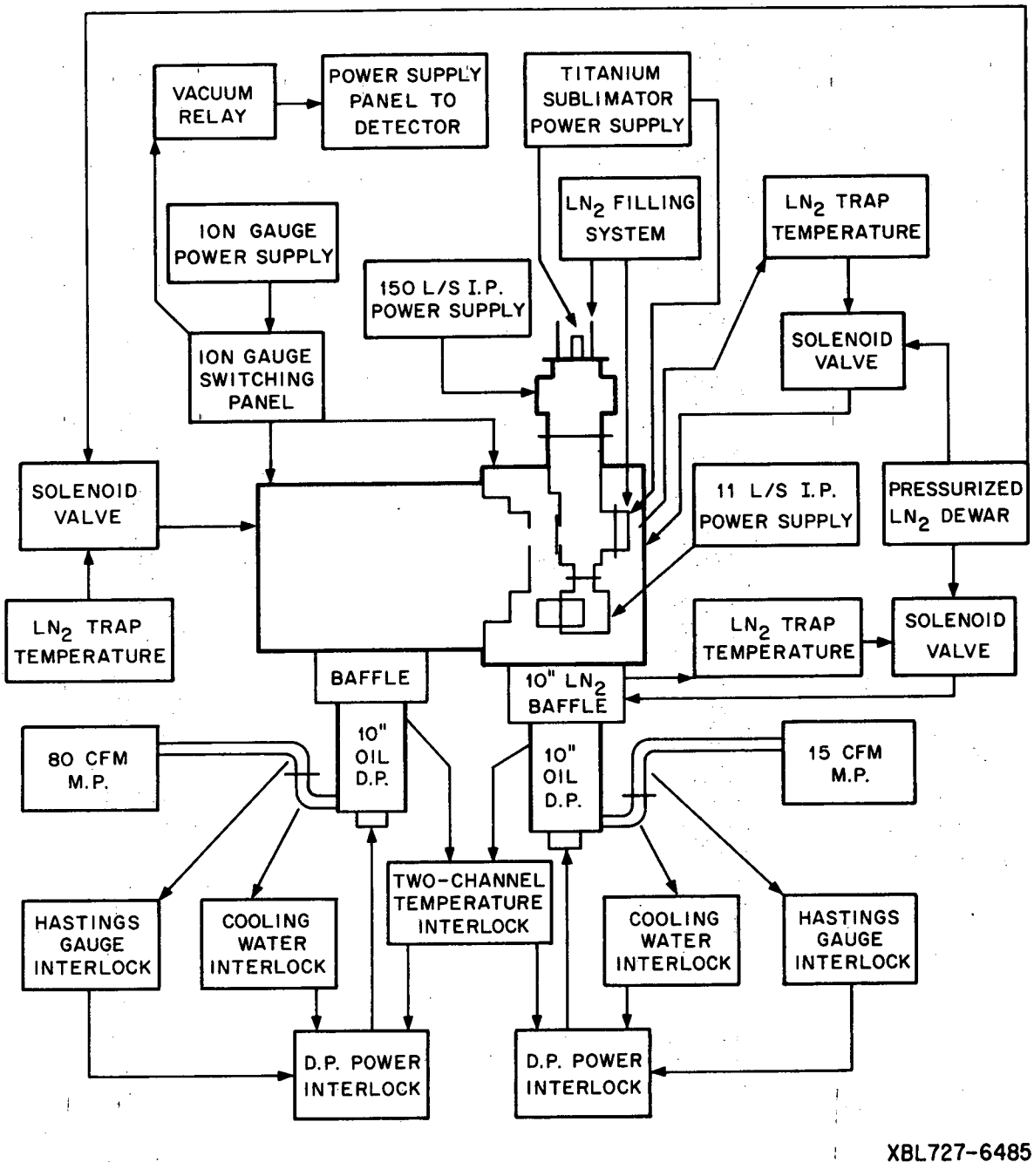

Fig. II-2. Block diagram of the apparatus vacuum system.

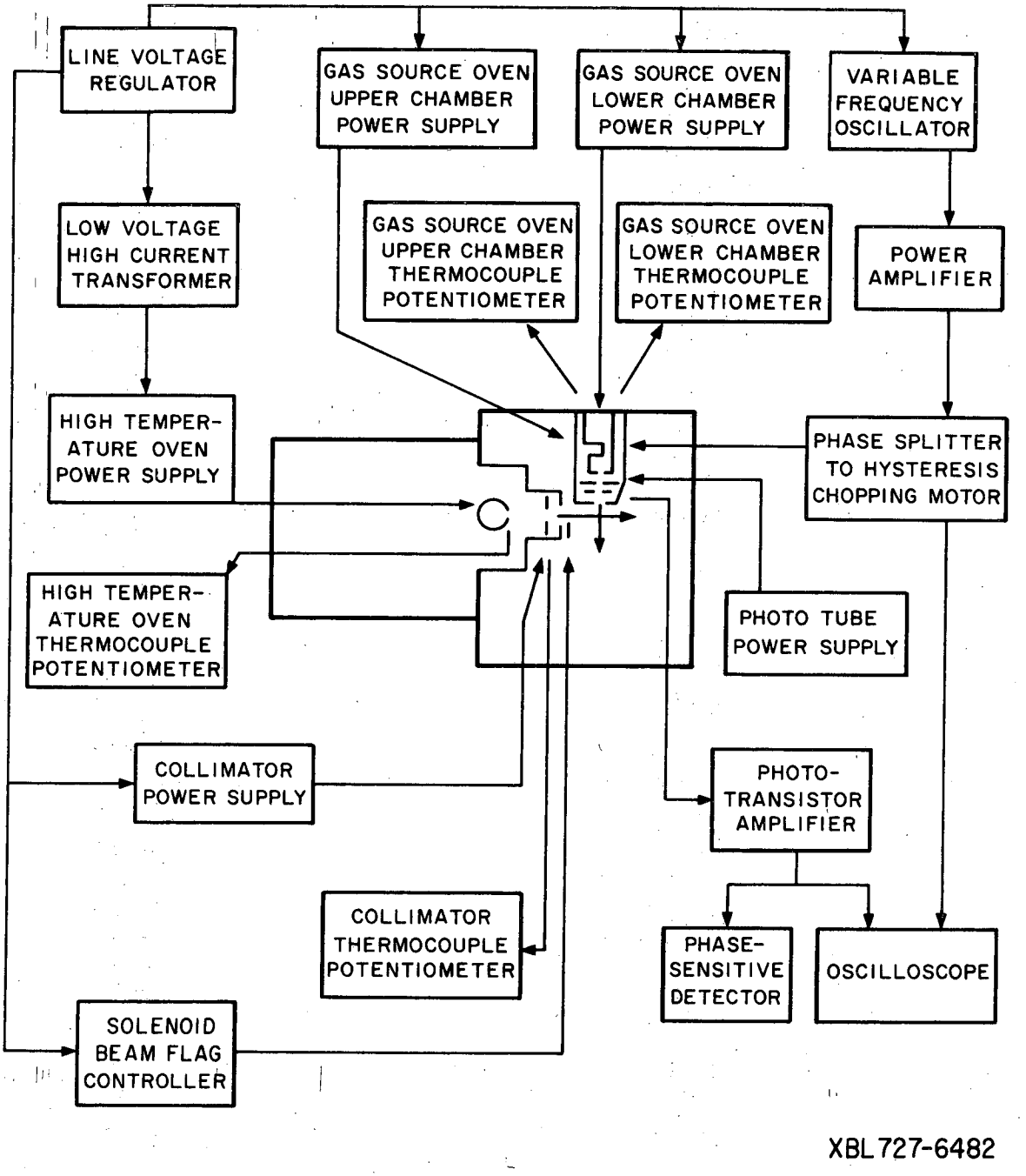

Fig. II-3. Block diagram of the beam sources and associated electronics.

Table I. Slit geometries and positions

Slit	width (cm)	height (cm)	distance from collision zone (cm)
Beam 1 source	.051	.48	17.1
Beam 1 collimator	.115	.71	9.5
Beam 2 source	.160	.71	5.1
Beam 2 collimator	.079	.71	2.5
Detector collimator	.206	.95	2.5
Detector slit	.051	.41	6.3

Table II. Typical operating conditions

Beam 1 source pressure	0.1-1.0 torr
Beam 1 source chamber pressure	$\sim 10^{-6}$ torr
Beam 1 oven temperature	900-1100°K
Calculated beam 1 number density at S.C.	$\sim 1.5 \times 10^{10}$ cm^{-3}
Beam 2 source pressure	1-4 torr
Beam 2 oven temperature	300-400°K
Beam 2 gas load	~10 torr ℓ/min
Calculated beam 2 number density at S.C.	$\sim 8 \times 10^{12}$
Collision chamber pressure	$\lesssim 10^{-6}$ torr
Detector chamber pressure	$\lesssim 10^{-8}$ torr

for the gas beam (beam 2) is mounted in the second aluminum chamber. The beams intersect in this chamber on the axis of rotation of a rotating lid onto which the detection chamber is welded. Thus, the detector, which is situated in the plane of the intersecting beams, can scan an angular range of 140° (see Fig. II-1) about the collision zone.

The alkaline earth source oven is a single-chambered crucible with standard knife edge slits, capable of holding 65 cm^3 of metal. At a source pressure of ~0.5 torr, this charge provided ~30 hours of metal beam. The crucible is heated by radiation from a resistively heated stainless steel tube which surrounds it. The beam is collimated and allowed to enter the collision chamber; it may be interrupted by a solenoid activated mechanical beam flag which is affixed to the flange connecting the two chambers. Although differential pumping of a metal beam might not seem necessary, the oven was placed in this first chamber because the high temperature and power requirements resulted in an outgassing rate which would have resulted in too high an ambient background pressure had it been situated in the collision chamber.

Beam 2 emerges from a "crinkly foil" multichannel slit[5] mounted on a standard double chambered oven. Since the gas beam source is mounted in the collision chamber, beam 2 materials are limited to those which are condensible at liquid nitrogen temperature. To provide rapid pumping of uncollimated molecules, the oven is surrounded by more liquid nitrogen cooled surfaces. The source can be charged by an external gas line, or the first oven chamber can accommodate a

thimble to hold compounds with insufficient vapor pressure at room temperature. In the latter case, the double chamber design allows one to establish the beam temperature independently of the vapor pressure. All gases used in these studies were introduced to the source via the external gas line. Pressure was monitored by a Datametrics Barocel capacitance manometer.

The multichannel array was prepared by stacking alternate layers of corrugated and flat stainless steel foil (thickness ~0.025 mm) resulting in channels roughly 0.012 cm in diameter and ~0.5 cm long. The calculated porosity of the array is ~50%. After emerging from this array, the beam is chopped (typically ~41 Hz) and collimated. It then intersects beam 1 at right angles, resulting in 1-5% attenuation of beam 1 and a negligible attenuation of beam 2. The resulting collision zone is approximately 0.3 cm full width on each side and ~2.0 cm full height.

The pumping in the collision chamber must be sufficient to provide a mean collision-free path much greater than the dimensions of the apparatus. Measurements of the intensity of beam 1 as a function of background pressure indicated that this is insured at a total pressure of $\sim 10^{-6}$ torr. A second requirement is that the background pressure of the product being detected be very low. To insure this, the background reactant pressures in the collision chamber must be low so that reaction takes place only in the collision zone. Also, any product formed must be pumped rapidly enough to prevent the accumulation of a large steady state concentration. Both beam sources are enclosed by

surfaces which should effectively pump any particle which is not in the beam. So, in effect, both beams are in differentially pumped chambers with extremely high pumping speeds. Also, the products and reactants are rapidly pumped by liquid nitrogen cooled surfaces after collision to prevent buildup of their partial pressures.

Beam 1 could be improved simply by reducing the distance from the source to the collision zone. The beam 2 source pressures exceeded the optimum pressures[5] for channels of these dimensions and the source could be improved by using an array with smaller channel dimensions.[6] The ultimate improvement, however, would be the use of a differentially pumped nozzle source.

C. Detector

1. Design Considerations

The products are detected by electron bombardment ionization. This method has two disadvantages when compared to the positive surface ionization technique used in alkali metal studies. The first is its low sensitivity. The best electron bombardment ionizers[7,8] are only a few percent efficient, compared to the approximately 100% efficiency for the positive surface ionization of the heavier alkalis.[9] The second disadvantage of the method is also its big attraction; that of non-specificity. While this enables one to detect any product, it also requires discrimination against the much larger ion signals due to background in the apparatus.

There isn't much one can do to improve the sensitivity except search for new ionization techniques, but the problem of sorting out the true product ion signal can be attacked systematically. One first sends the ions through a mass filter. This reduces the ion signals with incorrect charge-mass ratios to about 10^{-6} of their original values.[10] This residual background can be reduced further by keeping the total pressure as low as possible. This is done by clean ultra-high vacuum techniques and usually by one or more stages of differential pumping. One must still discriminate against the residual background at the product mass setting and guard against a build-up of product concentration in the detector during the experiment. The first of these is accomplished by clean vacuum techniques and sufficient pumping, along with the judicious choice of a product mass which differs from any large background components. The build-up of background product within the detector is minimized by adopting a "fly-through" design wherein the product molecules which are not ionized fly out of the detector region before they are pumped. Finally, one usually discriminates the true product from the residual background by chopping one or more of the beams and using either lock-in techniques or suitably gated scalars to retrieve the modulated signal.

A variety of ingenious techniques has been used in the past few years to enable experimenters to obtain scattering data on non-alkali systems. Although one study[11] employed an apparatus with no differential pumping for the detector, most utilize, in some form, the considerations presented here.

The detector consists of an ionizer, quadrupole mass filter, and electron multiplier, mounted vertically in the detection chamber. Figure II-4 shows a schematic of the detector along with its associated electronics, and Fig. II-5 is a cutaway drawing that will become clearer in the following discussion. The entire assembly is held by a clamp which is bolted to the chamber wall.

2. Ionizer

Because of space limitations, it was necessary to construct an ionizer which extracts the ions perpendicularly from the beam path. It was decided to use a design similar to Brink's,[8] but with slits out to allow it to function in the cross beam mode. A diagram of the ionizer and its electronics is given in Fig. II-6. The ionizing region consists of a grid, made by winding 0.025 cm dia. platinum wire around a stainless steel shell with six vertical posts. Two of the posts incorporated the entrance and exit slits, and the platinum wire was cut out of these slits. Two 1% thoriated tungsten ribbons (0.0005" × 0.025" cross section, Rembar Co., Inc., Dobbs Ferry, N.Y.) are mounted outside the grid as close as is practicable (~0.7 mm) in order to produce the most electrons at a given filament temperature. A stainless steel cylinder surrounds the grid and filaments and serves as a shield to reflect electrons back through the grid many times before they are collected by it. At one end the filaments are spot-welded to the shield while the other ends are spot-welded to a tungsten strip which serves as a leaf spring to keep the filaments taut when hot.

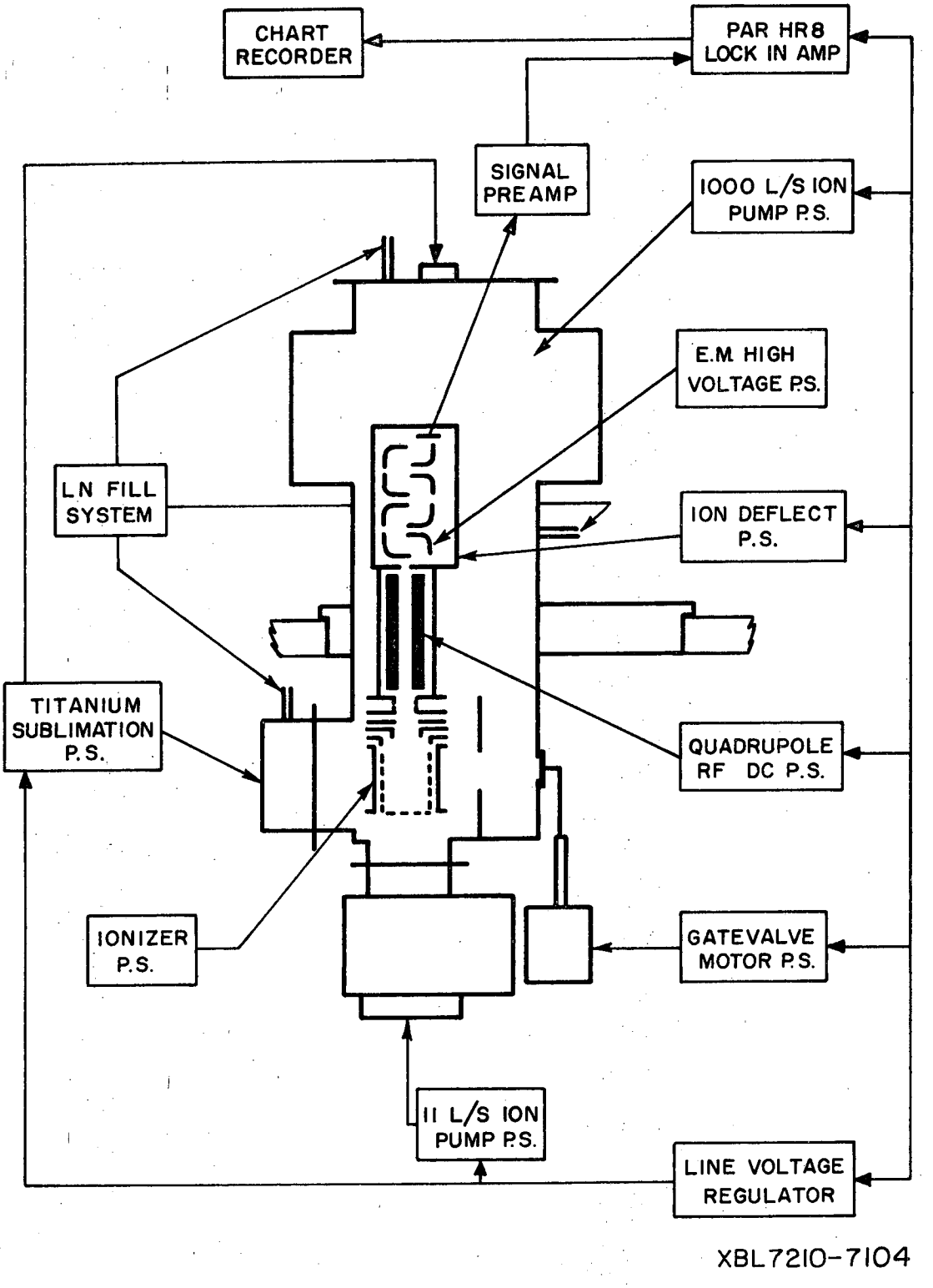

Fig. II-4. Schematic of the Detector and detector chamber with diagram of associated electronics.

Fig. II-5. Cutaway side view of detection chamber.

1. Collision zone
2. Gate valve and plate
3. Collimation chamber
4. Entrance slit to collimation chamber
5. Detector slit
6. Ionizer assembly
7. Quadrupole mass filter housing
8. Electron multiplier housing
9. Liquid nitrogen reservoir and shrouds
10. Rotating lid O-ring grooves
11. Titanium sublimator cold shroud
12. Titanium sublimation filament
13. Liquid nitrogen reservoir
14. 15 ℓ/s ion pump
15. To 1000 ℓ/s combination ion-sublimation pump

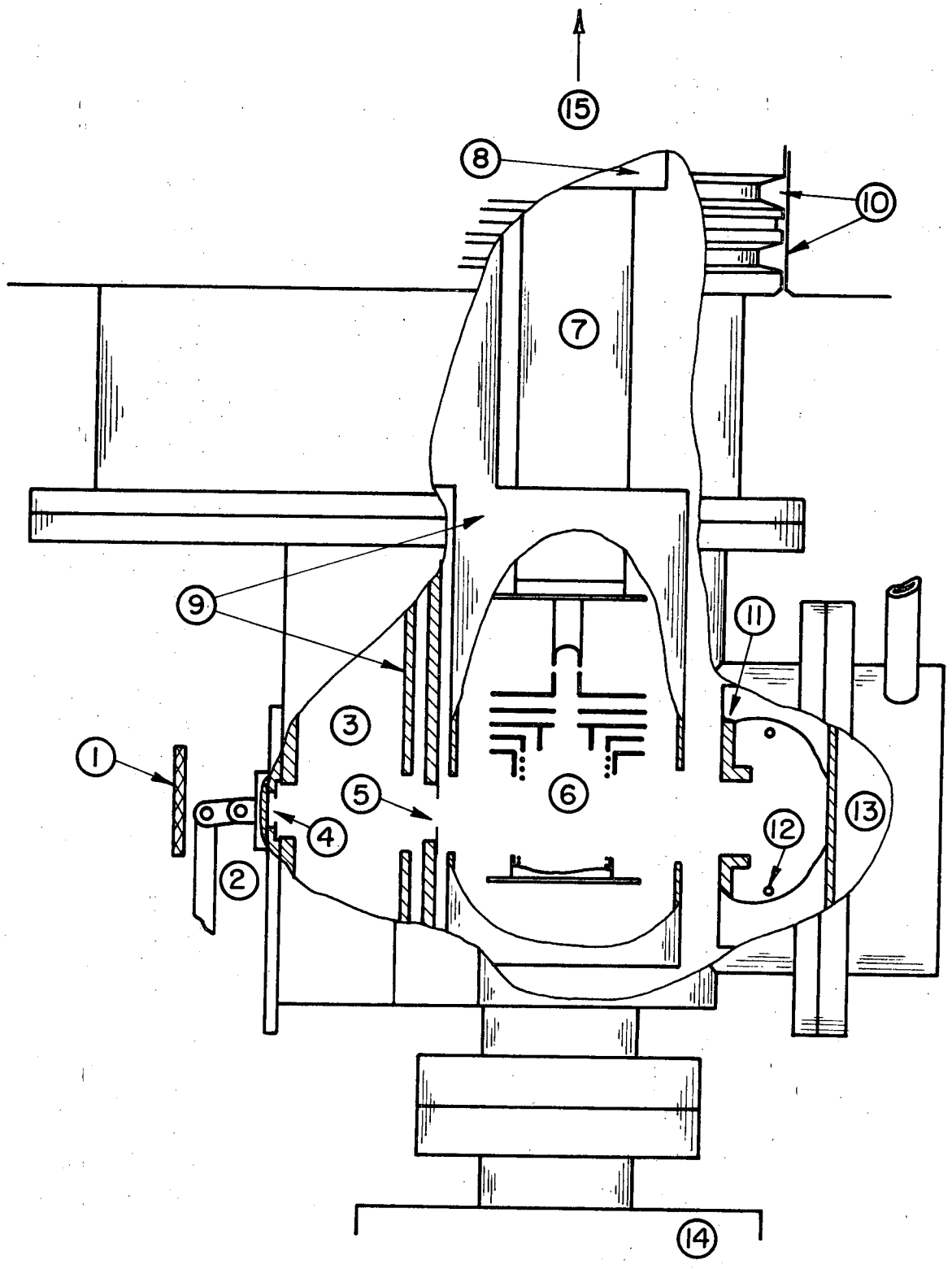

Fig. II-5.

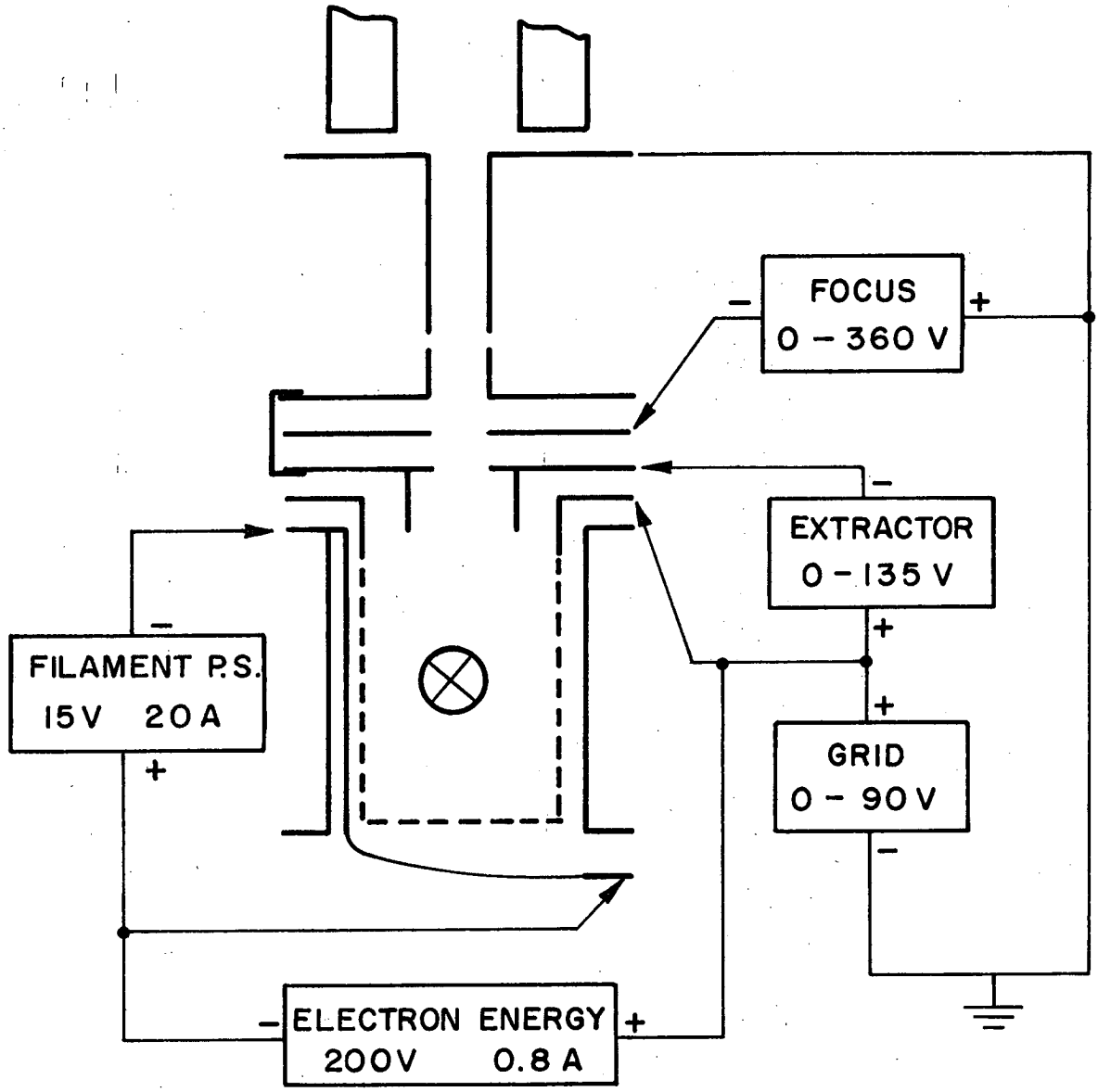

Fig. II-6. Cross section of ionizer with associated electronics.

Above the grid are the extracting and focusing electrodes, also made of stainless steel sheet and tube. All ionizer elements are mounted on four stainless steel rods, sheathed by alumina tubes, which descend from the uppermost electrode. Spacing is provided by alumina tubing cut to appropriate lengths, and the assembly is held together by nuts on the threaded ends of the rods. The entire assembly is then mounted to the quadrupole housing by screws.

A few words about the design: Brink's design, when operated in the axial beam mode, utilizes a potential wall along the axis, due to electron space charge, to hold the ions while they are slowly extracted. These delicate conditions are certainly destroyed when slits are cut to allow the beam to traverse the ionizer perpendicularly to the axis, and when large potentials are applied to the extracting electrode. Nevertheless, with appropriate extractor geometry, the equipotential surfaces in the grid resemble hemispheres centered about a point inside the extractor tube.[12] Thus, most of the ions are drawn to a "smudge" in the extractor tube. As they begin to diverge again, they pass through an Einzel lens[12] which has as its focal length the distance to the "smudge". This then produces an approximately parallel beam which is focused into the input aperture of the quadrupole housing by the final two-tube lens. Typical operating conditions for the ionizer are given in Table III.

Since the ions are "born" on different potentials, there is a spread in ion energies; and since the lenses are not "color corrected", the focusing scheme is only approximate. A good estimate of the

Table III. Typical operating conditions of ionizer

Element	
Grid	+60 V[a]
Extractor	- 5 V[a]
Focus	-130 V[a]
Electron energy	150 V
Electron emission	30-50 ma
Power dissipation, grid	~6 watts
Filament voltage	9 V } 25 watts
Filament current	2.8 a } 25 watts

[a] with respect to ground

collection efficiency of this configuration could be arrived at only by an extensive ray-tracing and was not attempted. However, from beam intensities it is estimated that the entire ionizer is $\lesssim$0.1 times as efficient as the values quoted for the original Brink design.

The electrical leads are 16 guage copper wire, sheathed in quartz tubing for insulation and attached to the appropriate electrodes by screw clamps. They are fed into the chamber by an 8-pin feedthrough in an Ultek UHV flange.

The quadrupole mass filter operates at nominal ground potential so that the ion energy is roughly defined by the grid potential. This is an upper limit due to the effects of the extraction potentials. The shield and filament are floated with respect to the grid (Lambda Corp., D.C. power supply, Model C880-M) by a voltage which roughly defines the electron bombardment energy. The potentials for the grid and the other electrodes are supplied by stacks of Burgess 45 volt "B" batteries and appropriate variable resistors. The filament is heated by an NJE, Model QR-15-20 D.C. power supply. The 25 watts dissipated by the filaments were used to bake out the ionizing region continuously when experiments were not in progress.

3. Mass Filter

The mass filter is an RF quadrupole type (Model Quad 250) purchased from Electronics Associates Inc. along with its RF-DC power supply. The quadrupole is attractive because of its relatively large entrance aperture, its compact size, and its easily varied resolution. The

resolution of the EAI unit is variable to values larger than the mass number for masses up to 500. A resolution of M is defined by EAI as that which resolves ion peak of mass M from an equally intense peak at M+1 with a 10% valley between. At higher mass numbers, settings which produce such resolution also lower the transmission markedly and so, during an experiment, the resolution is set at the lowest value which will exclude troublesome neighboring mass peaks. This is illustrated in Fig. II-7.

When the apparatus was first pumped down, the background mass spectrum was quite typical of ultra high vacuum systems[4,11] with a predominance of methane fragments, atmospheric constituents, water, and inert gases. As the experiments progresses, other background peaks became old "friends", notably one at mass 127 which was attributed to I^+ and which persisted throughout these experiments despite long bake-outs. Before an isolation valve was installed in front of the detection chamber and a liquid nitrogen baffle placed over the diffusion pump in the collision chamber, the build-up of background at almost every mass number was observed and attributed to contamination of the detection chamber by pump oil.

4. Electron Multiplier

The ions which exit the mass filter are accelerated toward the first dynode of a 22-stage electron multiplier (special model SPM-00-402, Dumont Electron Tube Div., Fairchild, Ind.). This 22-stage configuration assured reserve gain for ion counting. Single ion counting was

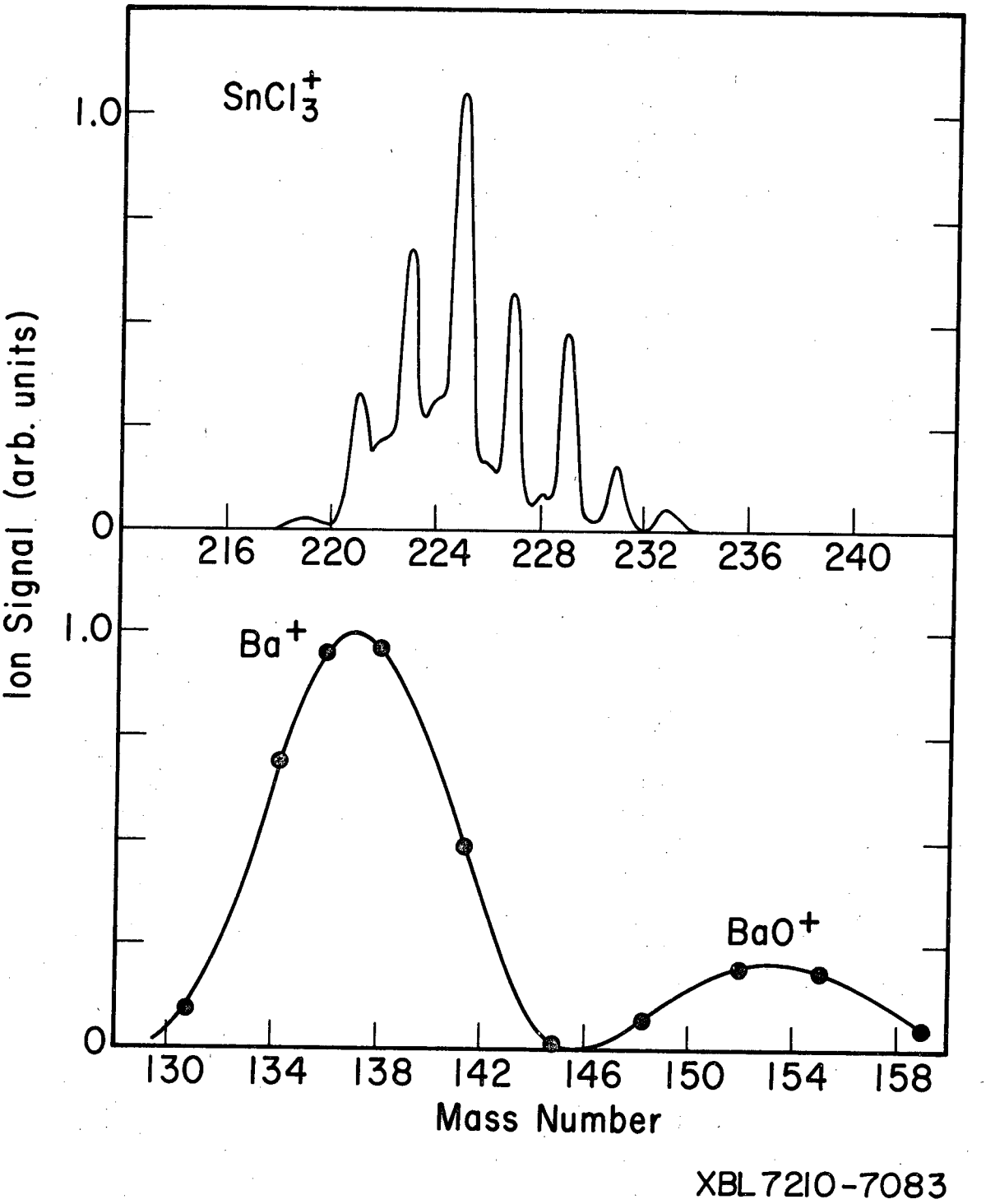

Fig. II-7. Sample mass spectra. The upper panel is a mass scan of the isotopes of $SnCl_3^+$. The mass resolution is ~0.7 times the mass number. The lower panel shows scattered Ba^+ signal resolved from BaO^+ at a resolution of ~0.08 times the mass number. The transmission of a given ion peak at the setting in the lower panel is more than 20 times greater than that at the setting for the upper panel.

attempted but problems with RF pickup from the quadrupole leads were never satisfactorily solved.

The ionizer produces photons to which the electron multiplier is sensitive, resulting in a large multiplier current. This was overcome by offsetting the electron multiplier ~1 cm from the quadrupole axis. An electrode was installed to deflect ions from the mass filter to the multiplier. The voltage for the electron multiplier is supplied by a Fluke model 408B high voltage power supply. Both the high voltage lead and signal lead are fed through 5 kV rated feedthroughs so that the signal lead could be floated to study negative ions (see Section G). The signal lead is doubly shielded and wrapped with pieces of mu-metal foil inside the detection chamber to reduce electric and magnetic pickup.

D. Detector Chamber

In order to reduce the total background in the region of the ionizer, one or more stages of differential pumping are usually provided. Originally, the detector chamber was to be one differentially pumped chamber, but later, in order to eliminate contamination problems, two pseudo-stages of differential pumping were provided along with a pump behind the ionizer to pump the molecules which fly through.

The detector chamber is an integral part of a stainless steel 12" dia. rotating lid on the main chamber. The rotating seal is provided

by two Viton O-rings lubricated with Dow Corning #33 heat-stable low-temperature silicon grease. A port is provided to pump out the volume between the two O-rings, but this was never necessary.

The upper part of the chamber is a 6" dia. cylinder on top of which is a 1000 L/S Ultek Cryo-Boostivac D-I combination ion-sublimation pump. The lower portion of the chamber is divided front and rear into two pseudo-chambers, open at the top. The rear one accommodates the ionizer and is called the ionizer chamber. The front compartment is a collimation chamber. The collimation chamber is closed at the bottom but the ionizer chamber is pumped from below by an 11 L/S Veeco ion pump. Directly behind the ionizer chamber is another, very small chamber which contains a titanium sublimation filament and is cooled by a small liquid nitrogen reservoir. In addition to providing additional pumping speed to the ionizing region, this provides a very effective trap for the un-ionized molecules which fly through the ionizer.

The slit between the collimation chamber and the ionizing chamber is the defining slit of the detector. For optimal pumping, the entrance slit to the collimation chamber is given the smallest dimensions (allowing for small misalignments) which avoid any viewing problems (see following section). The slits in the ionizer grid and shield are cut so that every molecule which has flown through both the collimation slit and detector slit will also fly through the ionizer untouched. These slits are also cut to the smallest such dimensions

(again allowing for small misalignments) in order to minimize perturbations to the potentials in the grid.

A nickel-plated copper liquid nitrogen reservoir sits atop the collimation chamber and from it hang two cold shrouds. One forms a curtain in the collimation chamber, and the other is cylindrical and surrounds the ionizer region. Ample slits are cut in these shrouds to allow passage of the product beam. So that the upper ion pump can effectively pump the collimation chamber, the reservoir has a vertical tunnel through it which is essentially a continuation of the collimation chamber. The reservoir is fed by tubes which enter the chamber through stainless steel Swagelok fittings. This arrangement was initially leak-tight at pressures as low as 10^{-10} torr, but after a month or so of thermal cycling, a small leak developed which was easily sealed by additional tightening of the Swagelok fitting.

The entire detection chamber can be isolated from the main chamber by a small cam-action slide valve which seals over the entrance slit to the collimation chamber. A 1 cps AC gear-motor drives a screw mechanism which raises and lowers the valve.

The ionizing chamber and collimation chamber are somewhat isolated from one another in that for a molecule to get from one to the other, it must pass up through the large ion pump, or, of course, through the detector slit. For condensibles, the pumping speed in both chambers is enormous, but because of the long tube to the collimation chamber, the pumping speed of non-condensibles there is limited by the conductance of the tube and is calculated to be ~25 liters/second. The

combined pumping speed of the small ion pump and sublimator at the ionizer is probably ~25 liter/second also. If the two are considered to be separate chambers, the ultimate calculated pressure for the ionizer chamber is $\sim 10^{-11}$ torr considering only effusion through the slits and a collision chamber pressure of 10^{-6} torr. The lowest pressure ever actually achieved was 2×10^{-10} torr (uncorrected ion pump reading). The pressure reading in the ionizer chamber was unavailable during an experiment, however, because the ionizer leaked electrons into the small ion pump, causing an erroneously high current reading.

The collimation of the product beam, fly through design, and liquid nitrogen shrouding proved invaluable in keeping the ionizer region free of contamination. Experiments in an earlier configuration with only one chamber were quickly terminated by a rapid rise in background at higher mass numbers, presumably from contamination and from outgassing from the chamber walls in the high temperature environment around the ionizer.

E. Viewing Corrections

It is important in angular distribution measurements that one knows how much of the collision zone the detector can "see" as a function of LAB angle. Ideally, one would design the detector such that it could see the entire collision zone, but there are often competing considerations. For instance, one desires a larger collision zone for larger intensities, but needs a well-collimated product beam for slotted disc velocity analysis,[13] magnetic deflection

analysis,[14] etc. Thus in Reference 13, the collision zone is 1 cm on a side, whereas the detector "sees" only a 0.1 cm swath through it. In Reference 14, these viewing corrections are quite large, varying over an order of magnitude as the LAB scattering angle varies from 0° to 90°.

In this apparatus, care was taken to insure that no viewing correction is necessary at any LAB angle. The positions and dimensions of the slits given in Table I produce a collision zone ~0.3 cm on a side (full width). The detector collimator slit geometry is adjusted to insure that each position in the collision zone can "see" all of the detector slit.

Calculations were made to determine the sensitivity of this problem to misalignments of the beams, broadening of the beams due to collisions, etc. The calculation proceeded in the following manner. The signal at a given angle is the sum of contributions from all positions in the collision zone. Provided certain conditions are met, the contribution from one position in the collision zone is given simply by

$$dS(\Theta) = A \cdot I(\Theta) \cdot \bar{n}_1(\tau) \cdot \bar{n}_2(\tau) \cdot \Omega(\tau) \cdot d\tau \qquad (1)$$

where $\bar{n}_i$ $(i = 1,2)$ denotes the number density of reactant molecules from beam i, $d\tau$ is the differential volume element, Ω is the solid angle subtended by the visible portion of the detector slit, A is the normalizing constant independent of angle or position, and $I(\Theta)$ is the LAB angular differential cross section. The requirements for

Eq.(1) to be valid are the following: (a) the detector resolution in LAB angle, Θ must be small, and (b) the distribution in relative collision velocity vectors must be the same throughout the collision zone. Both conditions are adequately met because of good collimation of the beams. The signal is then given by:

$$S(\Theta) = A \cdot I(\Theta) \int \bar{n}_1(\tau) \cdot \bar{n}_2(\tau) \cdot \Omega(\tau) \cdot d\tau \qquad (2)$$

Thus $I(\Theta)$ is obtained by dividing the signal $S(\Theta)$ by $AV(\Theta)$, where

$$V(\Theta) = \int_{\tau} \bar{n}_1(\tau) \cdot \bar{n}_2(\tau) \cdot \Omega(\tau) \cdot d\tau \qquad (3)$$

A simple computer program was written to calculate $V(\theta)$ for various apparatus slit configurations assuming effusive flow from the beam sources. A grid of points which covered the collision zone was provided. At each point in the grid, $\bar{n}_1$ and $\bar{n}_2$ were calculated (in relative units) by calculating the solid angle subtended by the visible portion of the beam 1 and beam 2 source slits, respectively. This automatically includes the $1/r^2$ and cosine dependence of emission from an effusive source.[15] The Ω's were similarly obtained by calculating the solid angle subtended by the visible portion of the detector slit. The integral in Eq.(3) was done by summing the contributions from each point and the process repeated for each desired LAB angle.

Since the source slit of beam 2 is a multichannel source, one might expect some broadening of the beam due to scattering in front of the source slit. Also beam 1 might be broadened by possible local high background pressure in the high temperature environment around

the oven. These conditions were simulated by calculating $V(\theta)$ for various assumed widths of the source slits. Figure II-8 shows that even if the beam 2 source slit were twice as wide as its nominal value, only a 10% viewing correction need be applied. Similarly, the beam 1 source slit could be four times its nominal width for the same magnitude correction. Experimental beam profiles indicated no evidence for the broadening of either beam except in the case of $SnCl_4$ (see Chapter V).

The effect of misalignments in the beams proved to be a more serious problem. Figure II-9 shows $V(\theta)$ calculated for various misalignments of beam 1 at the collision zone. As is evident from the figure, a misalignment of 1 mm at the collision zone introduces a serious (20%) error in the measured LAB angular distribution. The effect was the same for either direction of misalignment and was somewhat less for beam 2.

This problem was carefully guarded against by the following procedures. The oven and collimator were carefully aligned before each pumpdown. Based on experience with the optical cathetometer used for alignment, the maximum initial error is estimated to be 0.2 mm. Beam 1 profiles were measured after every thermal cycling of the oven to check for movement, and a careful check of the final alignment was made before removing the oven for refilling. Since the metal oven was removed often for refilling, it received more attention. The cross beam oven remained fixed throughout the study and after its careful initial alignment, beam profiles measurements

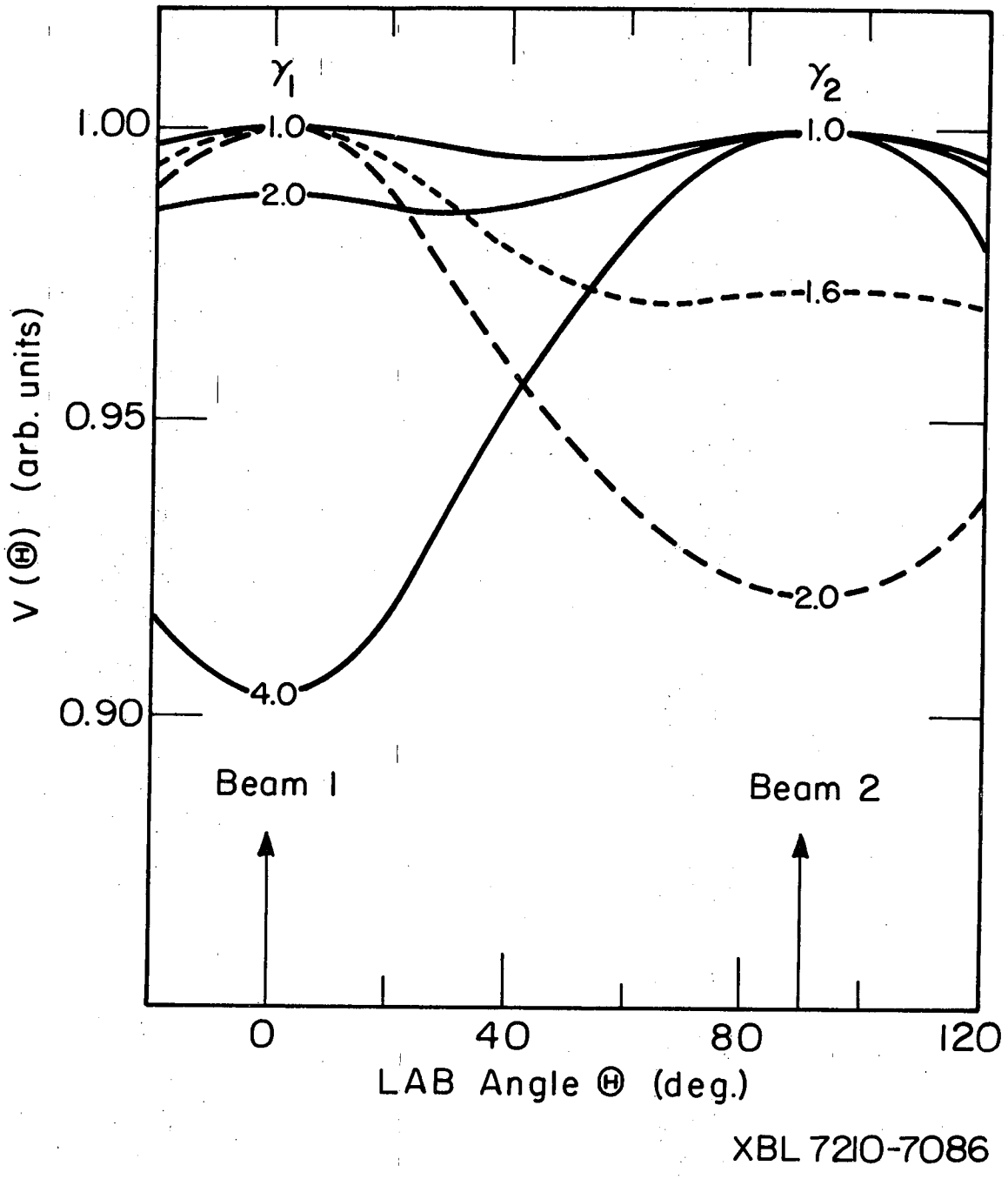

Fig. II-8. Apparatus angular intensity weighting function, $V(\theta)$ for various broadening of beam sources. γ_i (where i denotes beam 1 or 2) is the assumed width of the source slit of beam i divided by its nominal width.

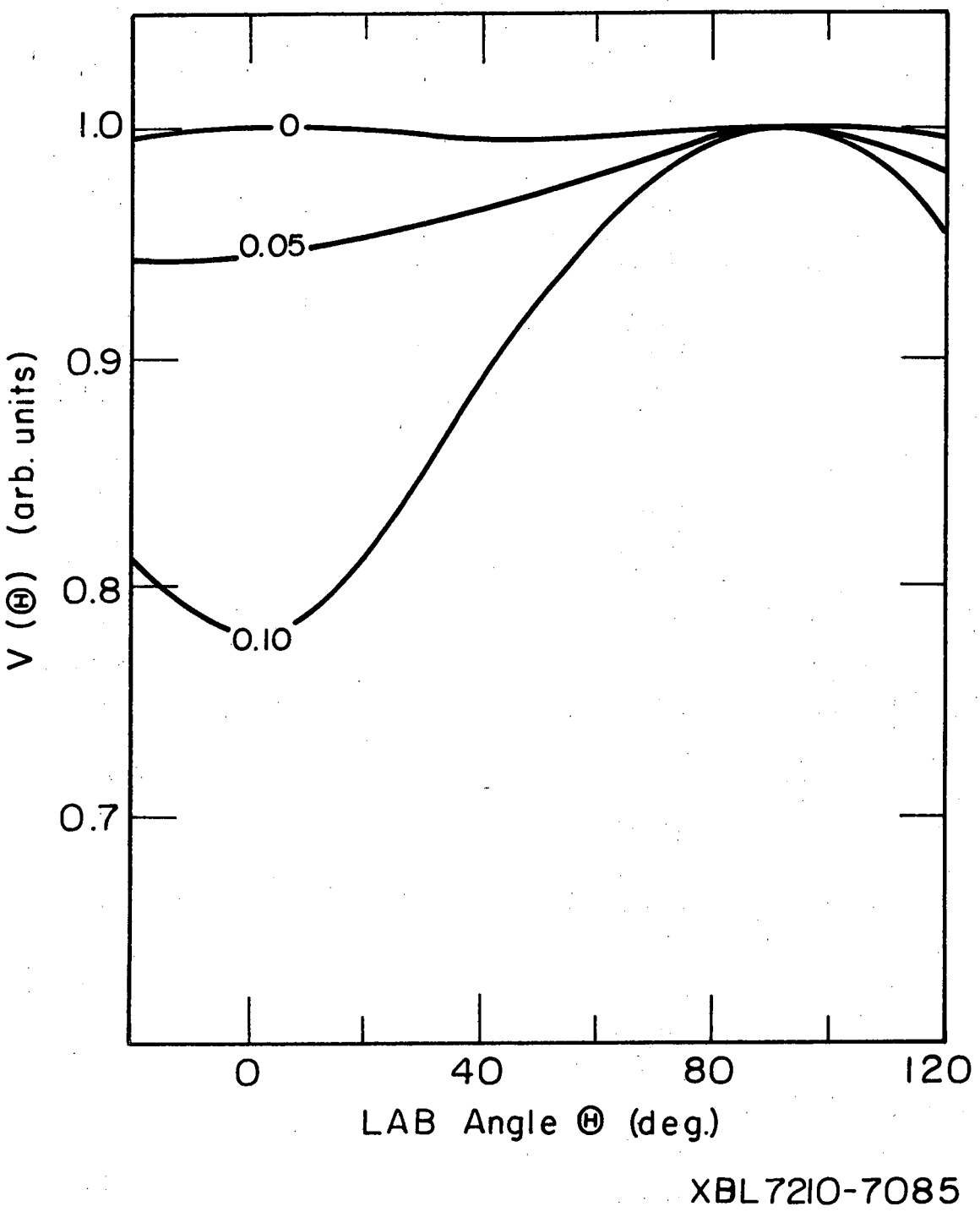

Fig. II-9. Apparatus angular intensity weighting function V(Θ) for various misalignments of beam 1 (in cm). The effect was the same for misalignment to either side.

and alignment checks were made only occasionally. Additional evidence for the absence of any viewing problems due to misalignment is the reproducibility of angular distributions from a given reaction on widely separated pump-downs. Also gratifying is the close agreement with another laboratory's results for Ba + Cl_2.[16]

F. Beam Velocity Distributions

In order to correctly educe information about the center-of-mass (CM) cross section from measured LAB distributions, one must characterize the beam velocity distributions. The velocity distribution for Ba in beam 1 and most of the beam 2 gases studied in Chapters III, IV, V, and References 1, 2, and 3 were measured using a small cylindrical velocity selector. All velocity distributions were found to be decidedly non-thermal in the pressure range used in the experiments.

1. Velocity Selector

The velocity selector used was an "afternoon experiment" type, made by cutting two 0.38 cm wide slits in a thin walled 3.8 cm dia. vertically oriented aluminum cylinder. This is a simplified version of a design reported by Crowley et al.[17] As is shown in Fig. II-10, one slit is offset by a 7° phase angle from a position directly opposite the other slit. A small notch is also cut in the cylinder edge directly opposite one of the slits to aid in alignment. The cylinder is mounted directly on the shaft of a miniature AC hysteresis motor (Globe model 53A112-2) capable of frequencies as high as 24,000

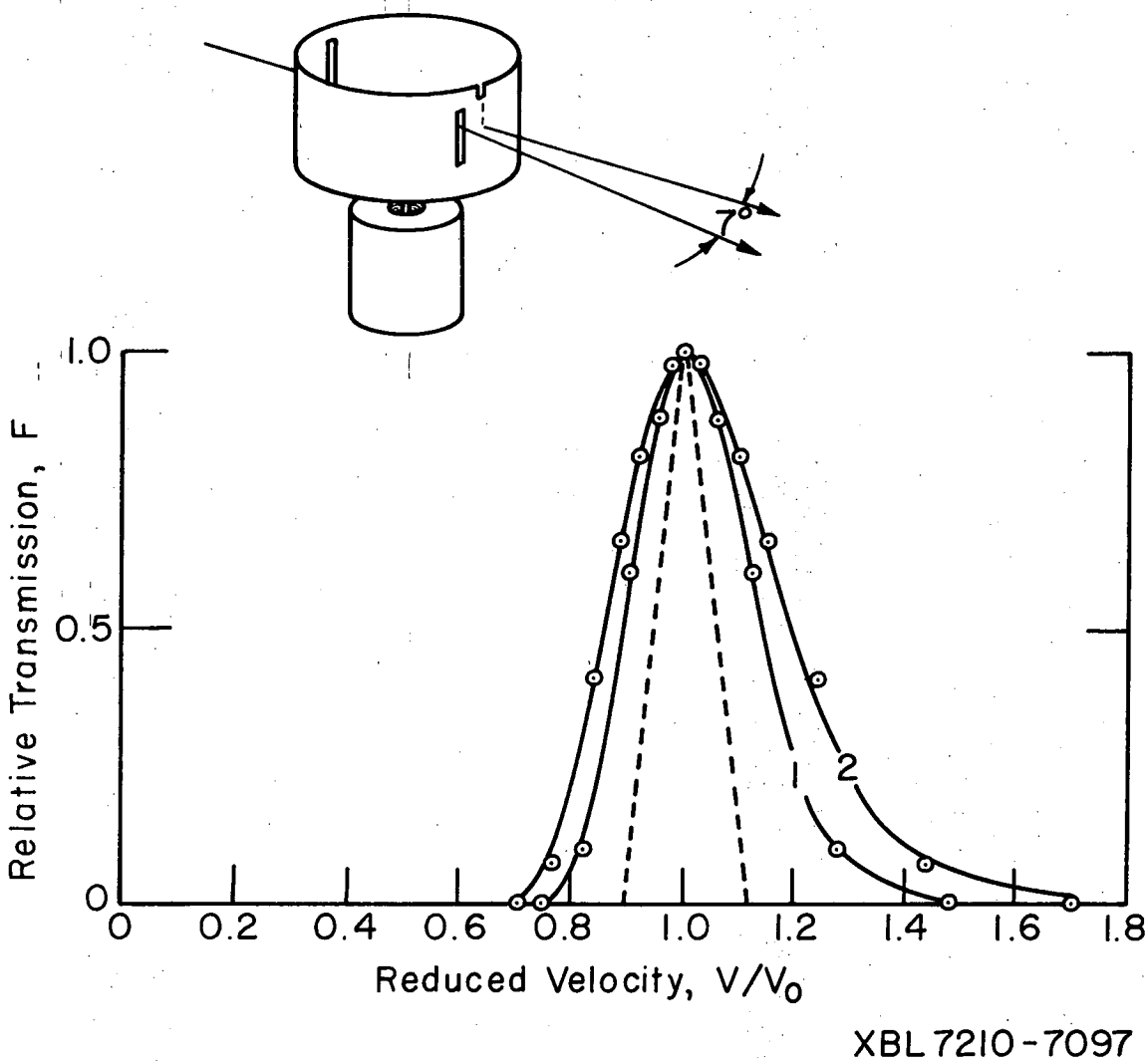

Fig. II-10. Simple drawing of the small cylindrical velocity selector and resolution function for beams 1 and 2. The points are calculated and the solid curves are fits given by

$$F_i = \exp[-(1-V_o/V)^2/H_i]$$

where i denotes beam 1 or 2 and the values of H_1 and H_2 are .022 and 0.38, respectively. The dashed curve is the resolution function for an infinitely thin beam.

rpm. This and the selector dimensions give a maximum nominal transmitted velocity of 8×10^4 cm/sec. The 0-40 volt two phase power was furnished by a power supply consisting of a variable frequency oscillator, power amplifier, and a variable capacitor to maintain the proper phase between the two power leads. The selector assembly was mounted on a bracket bolted to the main chamber wall and was aligned such that the beam axis intersects the rotation axis of the selector. The detector slit and the narrower of the two oven slits (source or collimator) define the beam. These two slits and the axis of rotation of the selector must be in perfect alignment, but this task is greatly simplified by the fact that the selector works in either mode of rotation. After mounting the selector in the beam, one simply rotates the detector slit until the data taken in both modes of rotation superimpose.

Figure II-10 also shows the resolution of the selector and the fact that the resolution varies with the width of the beam. Also shown is the resolution function for an infinitely thin beam (dashed curve). The calculated points (circles) are essentially calculated open times of the selector for the chosen values of the reduced velocity. The solid curves are analytical fits and are given by

$$F_i = \exp[-(1-V_o/V)^2/H_i] \qquad (4)$$

where the subscript i denotes beam 1 or 2, V is the velocity and V_o is the nominal selected velocity. The values for H_1 and H_2 are 0.022 and 0.038, respectively. It should be noted that if the beam, detector,

and selector slits are not mutually parallel, the F_i curves would be somewhat broader.

The velocity distribution data obtained are fit to a number density velocity distribution of the form

$$P_i(v) = N_i(v-a_i)^2\exp[-(v-a_i)^2/\alpha_i^2]\cdot u(v-a_i) \qquad (5)$$

where i again denotes beam 1 or 2; a_i and α_i are variable parameters; u(t) is the unit step function u(t) = 0, t < 0, and u(t) = 1, t $\geq$ 0; and $N_i = 4\pi^{-1/2}\alpha_i^{-3}$. This distribution has the form of a Maxwell-Boltzmann distribution characterized by most probable speed α_i which has been shifted bodily toward higher velocities by an amount a_i. This form has no theoretical justification, but was suggested by an examination of the data. Values of the parameters are chosen, the function convoluted over F_i, and the result is compared with the experimental data. The parameters are varied in this way until good fits to the data are found.

Signals were quite weak due to the small open time (0.002) of the selector; consequently, the beams were chopped and lock-in detection was used.

2. Gas Beam

Beam 2 velocity distributions were measured first since the source slit was a multichannel type and grossly non-thermal distribution had been reported for such a source.[13] The data in Fig. II-11 show very dramatically this non-thermal behavior. All the gases

exhibited similar behavior and the data were all well fit by Eq.(5) if α_2 is given the value α_o, where $\alpha_o = \sqrt{2kT/M}$ (k is the Boltzmann constant, T is the source temperature, and M is the molecular weight of the gas in question), and is the calculated most probable speed in the source, assuming a thermal distribution. The distributions are then essentially the nominal thermal distributions shifted toward higher velocity by the amount a_2. Values of a_2/α_o obtained are plotted against source pressue for all the gases studied in Fig. II-12. It can be seen that they form a rough family of curves that increase with source pressure, and that the values can be quite large. Failure to take the non-thermality of these distributions into account can lead to serious errors in the analysis of LAB scattering data (see later chapters). The data in Fig. II-12 also seem to show a trend toward higher a_2/α_o values for more complex molecules.

Although many crossed beams studies have used "crinkly foil" multichannel sources, most have ignored the possibility of non-thermal velocity distributions. Many of the early alkali metal studies[18] reported gas beam source pressures of ~0.3 torr, although these pressure readings were taken from a thermocouple gauge which was unlikely to be very accurate; the actual pressure may have been as high as a few torr.[19] Even at 0.3 torr there could be an appreciable effect, especially in the case of the larger alkyl halides in Reference 18b. In the Li studies[14] source pressures of ~3 torr are reported, but while this suggests non-thermal beam conditions, the effect on the

Fig. II-11. Br_2 velocity distribution data. Shown are raw velocity data for four different source pressures, normalized to the same peak intensity. The solid curves are fits using Eq.(5) and convoluting over the selector transmission function (Eq.(4)). The values of the parameters which provided these fits are represented in Fig. II-12. The dashed curve is the Maxwell-Boltzmann distribution for the measured source temperature (330°K), also convoluted over Eq.(4).

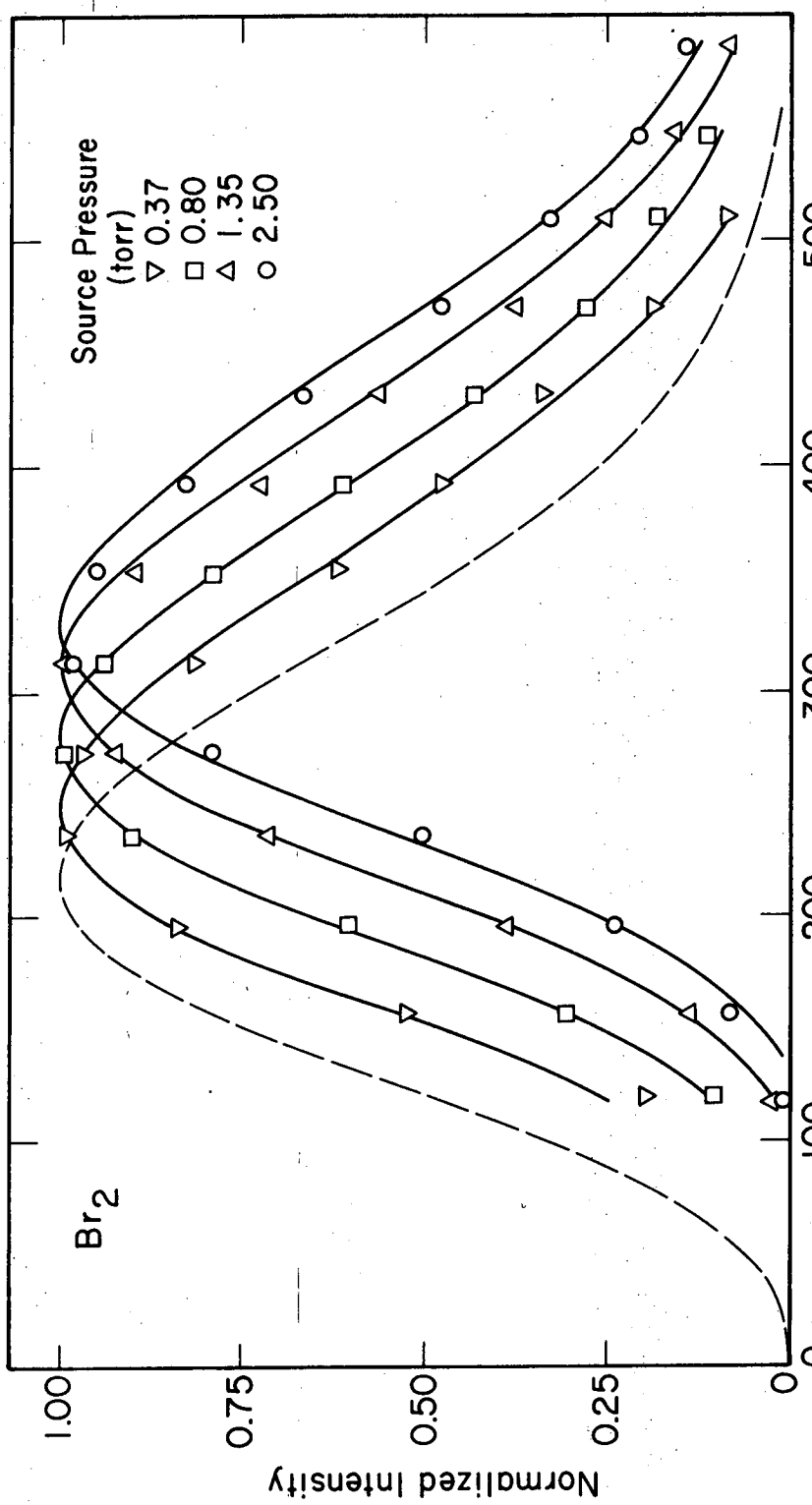
Source Pressure
(torr)
▽ 0.37
□ 0.80
△ 1.35
○ 2.50
Br_2
Normalized Intensity
1.00
0.75
0.50
0.25
0
0
100
200
300
400
500
Nominal Transmitted Velocity (m/sec)
XBL 7210-7084

Fig. II-11.

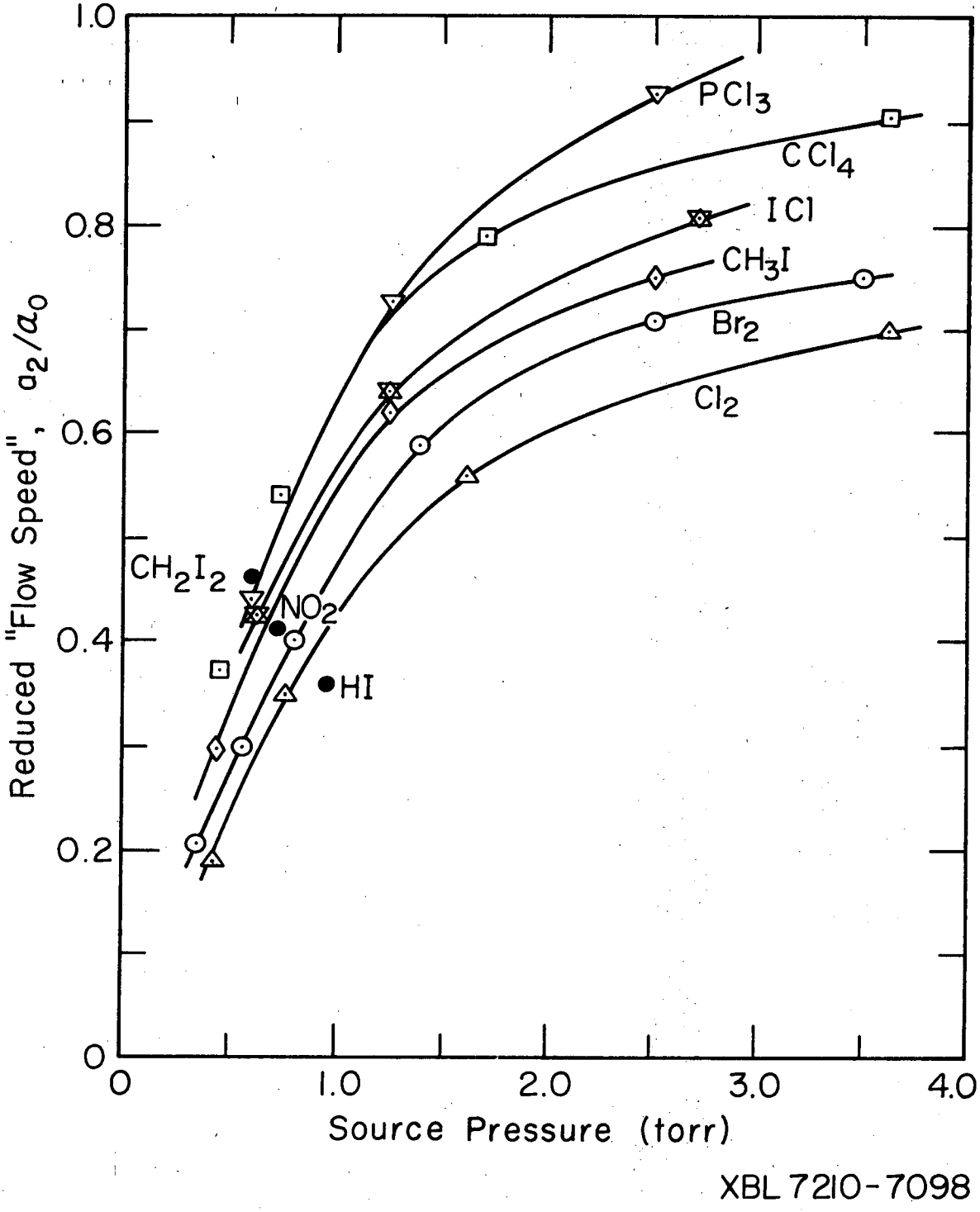

Fig. II-12. Gas beam velocity distributions. Plots of the reduced parameter a_2/α_o are shown as a function of source pressure. The velocity distributions for CH_2I_2, NO_2, and HI (solid points) were measured at only one pressure.

analysis should be less important due to lithium's much lighter mass, and consequent higher speed. Gillen and co-workers[20] noticed that the peak in the KBr distribution from K+HBr moved to LAB angles nearer the HBr beam as its source pressure was increased. This was an indication of higher velocities in the HBr beam and therefore they reduced the HBr pressure until no further effect was noted before using the data. Even then, the analysis indicated some residual non-thermality in the beam distribution. A kinematically constrained reaction such as K+HBr is especially sensitive to the beam velocity distributions (see Chapter III).

Blais and Cross[13] have reported velocity distributions of Br_2, I_2, and IBr in a beam with a "crinkly foil" source slit very similar to the one here which are in good agreement with the data here. Although no source pressure is quoted, the Br_2 distribution they report is identical to the result here for 1 torr. Rulis[21] reports a behavior for CH_3I which is qualitatively similar to that observed here but occurring at somewhat higher pressures. This is undoubtedly due to the smaller channel dimensions (0.025 mm dia. and 0.16 cm length) in his capillary array.

Generally, theoretical and experimental studies[5,22] of the properties of multichannel beam sources have been limited to pressures such that the channel length is at most ~50 times the mean free path. This corresponds approximately to the lowest pressures measured here (~0.2 torr). There are no good theories to explain behavior in the range between these pressures and those where hydrodynamic flow is

applicable. The theory of nozzle expansions[23] predicts an enhancement of directed translational energy in the beam at the expense of energy contained in other modes of the molecules as the source pressure is raised. While this certainly does not explain the retention of the full nominal thermal width in these distributions, it may explain the generally greater effect seen for the more complicated molecules.

3. Alkaline Earth Beam

The alkaline earth beam source slit is of standard knife-edge design[15] and the oven generally operated at lower source pressures than the cross beam; therefore, less deviation from thermal behavior was expected.

Figure II-13 shows the velocity distribution obtained for Ba at 0.4 torr (solid curve). Comparison with the thermal (dashed curve) distribution shows that this distribution is much less non-thermal than the gas beam distributions, but a marked deficiency of low velocity atoms is evident. This effect is well known[15,24] and is generally attributed to the formation of a "cloud" in front of the oven slit which preferentially scatters slow-moving atoms out of the beam. What is surprising is that identical distributions were also obtained for 0.7 torr and 1.0 torr source pressures. Also shown in Fig. II-13 is a reported velocity distribution for K at 0.3 torr source pressure[25] and Li at 0.5 torr.[26] Identical distribution were also obtained at source pressures of 0.7 and 1.0 torr. As is evident, the three curves are virtually superimposible in this reduced

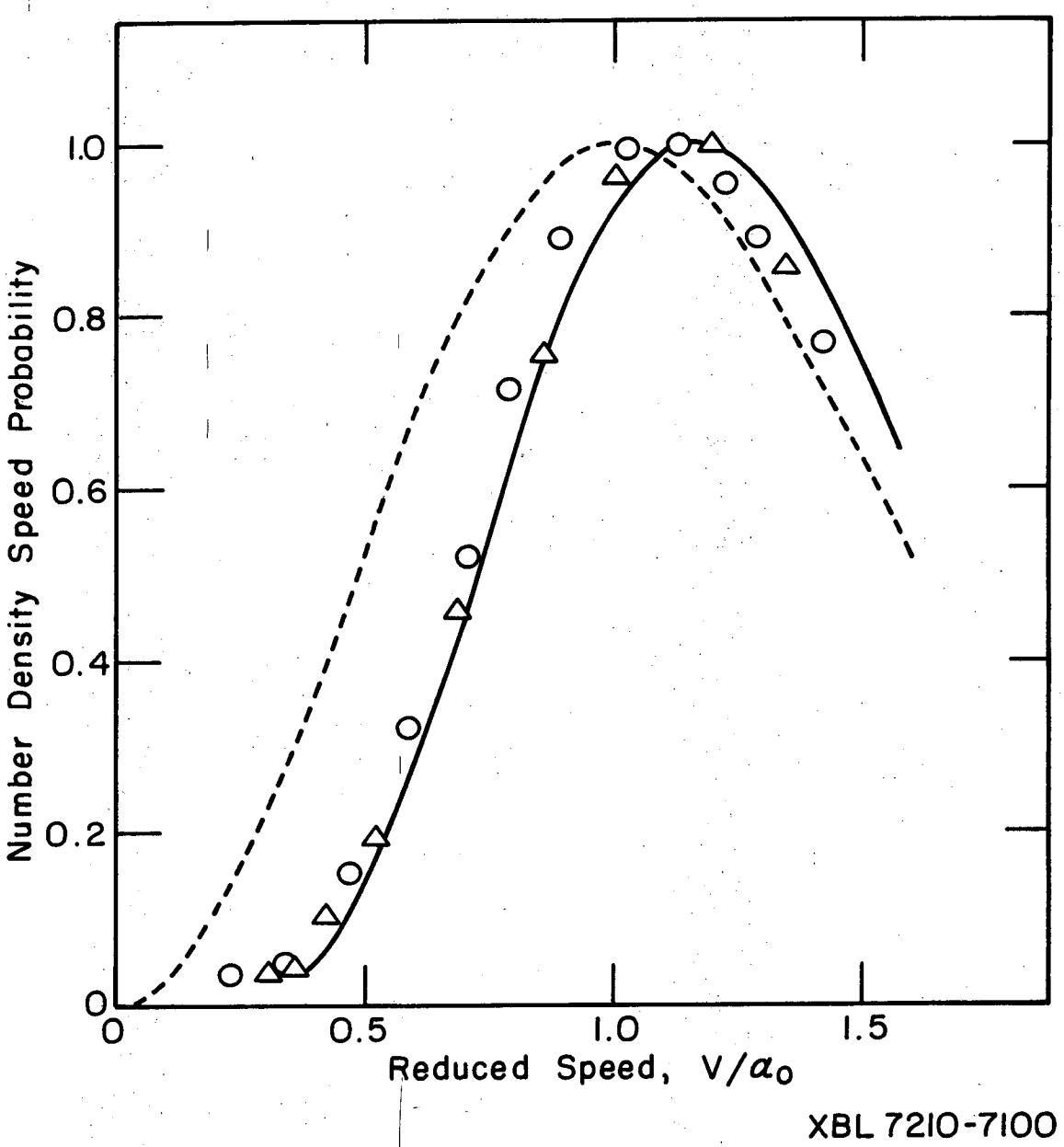

Fig. II-13. Reduced velocity distribution for Ba (solid curve), K (circles), and Li (triangles) at source pressures ~0.3-0. 5 torr. The dashed curve is Maxwell-Boltzmann.

velocity plot. All are well fit by Eq.(5) with the following parameter values: $\alpha_1 = 0.89\ \alpha_o$, and $a_1 = 0.33\ \alpha_1$, where all variables are defined in the previous section.

A simple long-standing model developed in Reference 26 gives the form of the velocity distributions as

$$P(v) = N(v^2/\alpha_o^2)\ \exp[-(v^2/\alpha_o^2 - k\bar{F}(v/\alpha_o)] \qquad (6)$$

where k is a parameter and $\bar{F}$ is a non-analytic function which is nearly constant for $v/\alpha_o > 1$ but rises steeply at smaller values. Excellent fits to the data are also obtained with Eq.(6) with a value of k = 2.5 - 3.0. According to the model, however, the parameter k should increase proportionally with source pressure, with a slope that scales as the collision cross section of the gas in question. Signal limitations precluded the measurement of Ba velocity distributions at lower pressures but data on Li at pressures less than 0.1 torr indicate a roughly linear dependence of "best fit" k values on pressure in that region. So the theory seems to be qualitatively obeyed at low pressures but the distributions seem to "saturate" at k values ~3.0.

Because identical reduced velocity distributions were obtained for these three metals with widely different masses, the same parameters in Eq.(6) were used to generate Sr, Ca, and Mg distributions for use in analyzing the alkaline earth reactive scattering data. Mg could not be studied with this selector because of its light mass and consequent high speed, and intereference in the mass spectrometer from Ar^+ precluded the measurement of Ca distributions. Since the

collision cross sections get smaller as one goes Ba → Sr → Ca → Mg (because of diminishing polarizabilities), the assumption of "saturation" for the distributions of Mg and Ca may not be valid. For these experiments, though, this is unimportant because correction for the non-thermal metal beam had a negligible effect in the data analysis.

It is not clear why the velocity distributions "saturate", since both Eq.(6), based on molecular flow, and nozzle theory predict progressive narrowing of the distribution as pressure is increased. Again the pressures here are in the region where there are no good theoretical treatments. Perhaps particles begin to be scattered back into the beam as fast as they are scattered out. This might be expected to result in a broadening of the beam profile, but in view of the small angles involved, the broadening might not be noticeable. In any case, no broadening of experimental beam profiles was observed.

G. Negative Surface Ionization

1. Introduction

The positive surface ionoization technique which made possible the molecular beam scattering studies of alkali metals, relies on the transfer of an electron from a substance with a low ionization potential to a surface with a high work function.[27] When an atom is adsorbed on a surface it can leave the surface either as a neutral or a positive ion, and the ratio of ions to neutrals is predicted by the Saha-Langmuir equation:

$$I_+/I_o = g_+/g_o \exp[(\phi-I)/kT] \quad (7)$$

where g_+ and g_o are the partition functions of the positive ion and neutral respectively, ϕ is the work function of the surface, and I is the ionization potential of the neutral atom. This simple theory assumes, among other things, complete equilibrium on the surface, no interaction of an atom either with the surface or another atom on the surface. Desorption lifetimes studies[28] of alkali metals on Mo and Ta surfaces indicate appreciable interaction energies with the surface. Nevertheless Eq.(7) seems to hold for alkali metals on a variety of surfaces.

It has long been recognized that the analogous process whereby negative ions are formed on low work function surfaces from precursors with high electron affinities might provide a sensitive detector for certain species in scattering experiments. The appropriate Saha-Langmuir equation is

$$I_-/I_o = g_-/g_o \exp[(E_a-\phi)/kT] \quad (8)$$

where E_a is the electron affinity of the neutral and other symbols are analogous to those in Eq.(7).

An early study[29] reported up to 60% yield of chloride ion when a CsCl beam was directed onto a hot thoriated tungsten wire. However, a later and more extensive study[30] of the formation of positive and negative ions on various surfaces did not bear this out. Not only were the efficiencies of the negative ion formation on low work

function surfaces much less than predicted, but as the surface temperature was raised, the efficiencies reached a maximum and then declined. The best reported efficiency was 3%, on thoriated tungsten. No mass analysis of the ions was performed in Reference 30, but others[31,32] have reported the formation of various molecular negative ions on surfaces. There have been, in addition, several studies[28,33] of desorption lifetimes of various halide ions from surfaces and they generally indicate larger interaction energies with the surface than the alkali metals.

2. Experimental

At an early stage in the evolution of this apparatus, it was decided to extend these studies and evaluate the possibility of using negative surface ionization as a detection scheme for scattering studies, in particular to examine the production of fluoride ion on thoriated tungsten.

The apparatus used was essentially the apparatus described in this chapter, with the only important difference being the replacement of the electron bombardment ionizer by a heated filament of the surface under study and appropriate focusing electrodes. The mass analyzed negative ion currents were amplified by the electron multiplier and the output measured by a battery operated Kiethley electrometer which floated at the output potential of the electron multiplier (~5 kV). The electrometer was housed in an insulating box; the scales were manipulated with a long ceramic rod with a rubber tubing gripper on the end.

The apparent filament temperature was measured with an optical pyrometer of the disappearing filament type and corrected for spectral emissivity (Reference 34, p. 241). The molecule under study was introduced into the beam source oven and the detector was rotated to look at the beam. Any negative ion currents were measured as a function of filament temperature. Desorption lifetimes were roughly measured by interrupting the beam and then observing the current decay on the electrometer. The response time of the meter needle (0.5 sec) set a lower limit on the lifetimes measured.

3. Results - Thoriated Tungsten

The 0.003" dia. thoriated tungsten wire was purchased from Rembar, Inc. and activated according to directions in Reference 34. Because of electron multiplier amplification, absolute ionization efficiencies were not obtainable. The qualitative behavior of the chloride ion signal from CCl_4 reproduced that of Reference 30. In addition, the response times were quite slow, on the order of seconds at the temperature which gave the maximum ion signal. A similar behavior was noted for Cl^- from $SnCl_4$ and despite the stability of the chlorostannate ion ($SnCl_3^-$), none was detected.

The results for the fluoride ion formation were even more discouraging. Not only were the ion intensities much lower than those for chloride, but the response times were even slower at the same temperatures. This is summarized by the data in Fig. II-14, which presents the temperature dependence of the intensities and lifetimes

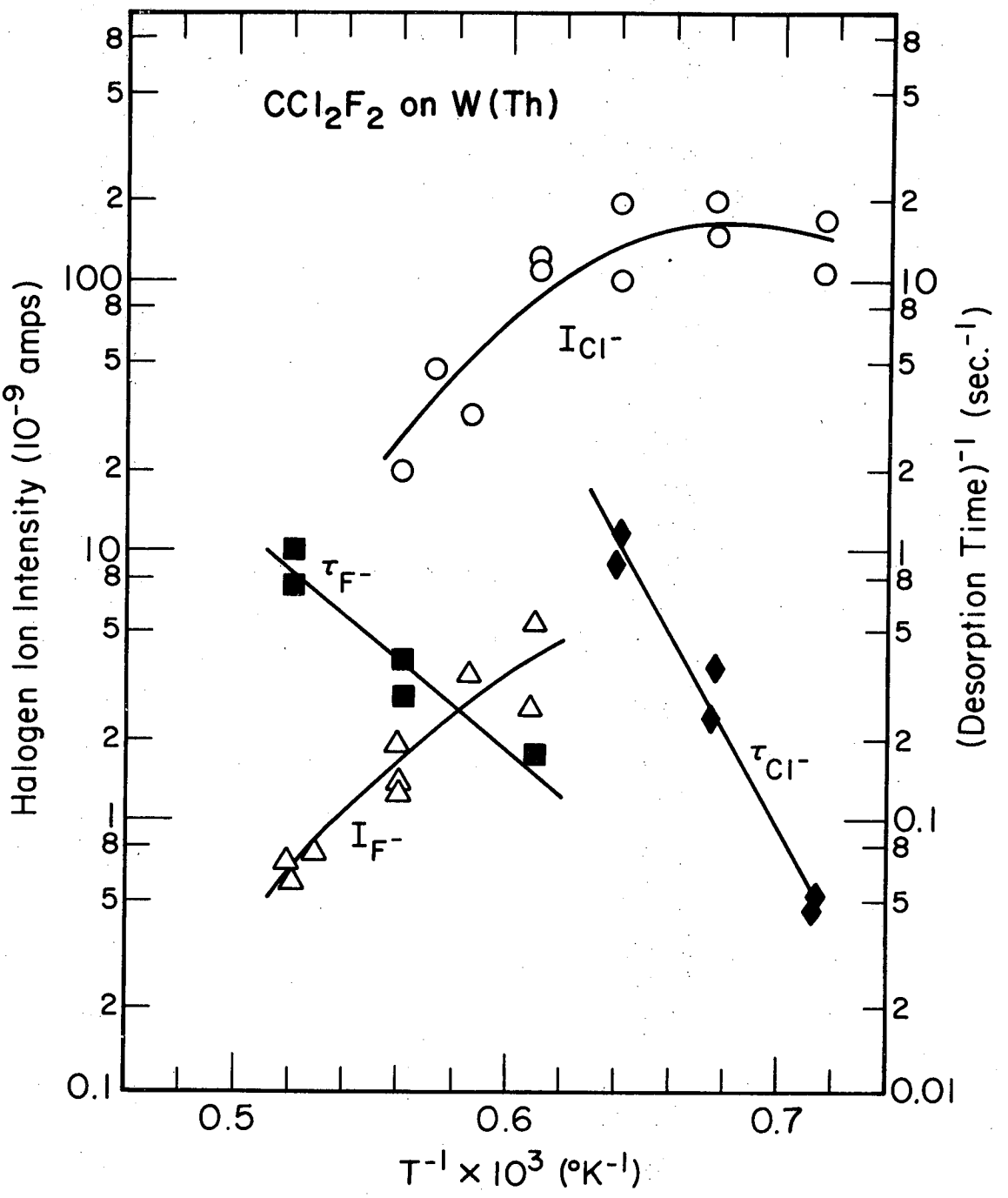

XBL 7012-7464A

Fig. II-14. Chloride and fluoride formation from CCl_2F_2 on W(Th). The intensity ordinate refers to the intensity data (open symbols), and the reciprocal lifetime ordinate refers to desorption lifetime data points (solid symbols).

for both F^- and Cl^- from a beam of CCl_2F_2. The ratio of F^- to Cl^- is only 0.1 instead of the stoichiometric 1.0. Muschlitz[35] confirmed this behavior along with reporting similarly disparate ratios for other freons. If the present Cl^- data from CCl_4 is normalized to that in Reference 30, then the fluoride ion formation efficiency here is estimated to be $<10^{-3}$ for CCl_2F_2 and considerably worse for BF_3 and SiF_4. At temperatures where the response times are convenient (1 sec), the efficiencies are another factor of ten lower. No molecular ions were detected from any of the compounds studied. Attempts to observe NO_2^- from NO_2 resulted in the immediate deactivation of the filament.

4. Results - Graphite

The next and last surface tried was graphite. Filaments were prepared from threads of graphite cloth and clamped in place. Figure II-15 shows the data obtained for chloride ion from CCl_4. Over the temperature range observed, the data are fit by the Saha-Langmuir equation if the work function is taken as 4.2 eV, a number in reasonable agreement with tabulated values.[36] Desorption times were also conveniently fast. Extension of the data to higher temperatures was prevented by repeated filament burnouts, probably a result of non-uniform thickness of the threads. A large ion signal at mass number 24 was observed and assigned as C_2^-, as this and other fragments have been reported in the spectrum of negative ions evolved from carbon surfaces.[37]

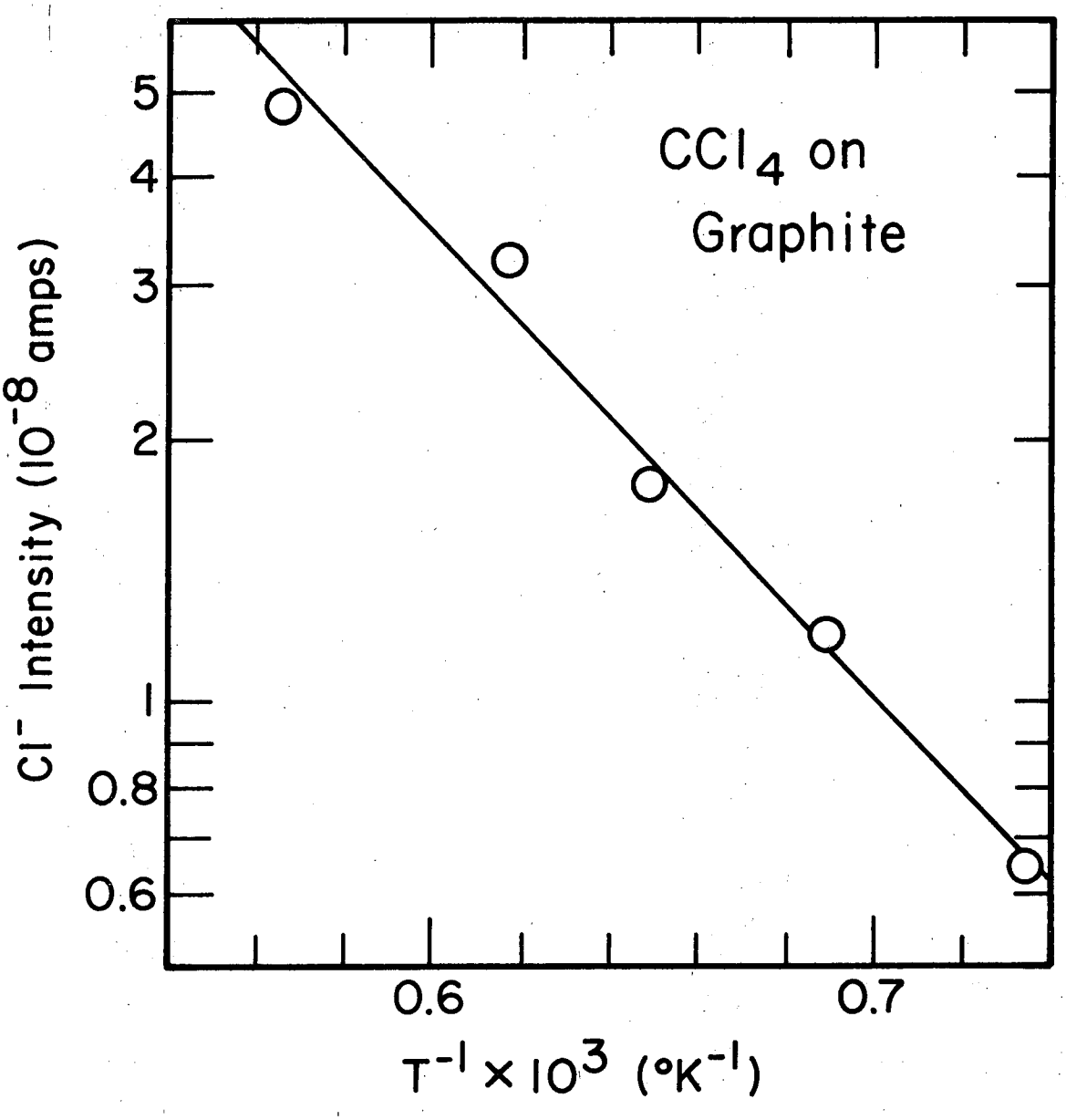

Fig. II-15. Chloride ion formation from CCl_4 on graphite.

5. Discussion

The results for the evolution of fluoride ions from thoriated tungsten are even more discouraging than the results for the other halide ions reported in Reference 30. There is some mystery as to why negative surface ionization yields and response times are so poor on the low work function surfaces. More than likely, there are alternate channels of escape for the halogen atom from the surface. This could be by incomplete dissociation of the parent molecule and subsequent re-evaporation of fragments with lower electron affinities, or by formation of volatile halides of the surface metal. Muschlitz[35] makes the first argument to explain the low F^-/Cl^- ratios, since the carbon-fluorine bond is stronger than the carbon-chlorine bond. The second channel is plausible because many metals (including W and Th) have volatile polyhalide salts; Cl_2 has long been known to attack hot tungsten, giving off WCl_6.[38] In addition, the long desorption times indicate a strong interaction with the surface. These long desorption times also raise the possibility of appreciable surface coverage which would be expected to raise the work function if the adsorbed species is electronegative.[39] Also since the work function is generally a nonlinear function of surface coverage[34] a surface ionization detector with these characteristics would probably be nonlinear. Although the formation of negative ions on high work function surfaces seems to obey Eq.(8), it seems that the properties of a low work function, which should give large ion yields, and high heats of adsorption and/or surface chemistry go hand in hand.

So far there has been only one reported molecular beam elastic scattering study which used negative surface ionization as a detection scheme.[40] Because of the foregoing considerations, a compromise surface was chosen, niobium, which had an efficiency of 0.1%. This is less than that for good electron bombardment ionizers.

The results here with graphite indicate that this surface might be useful as a molecular beam detector if its ionization efficiency continues to rise with temperature. Equation (8) predicts a 10% efficiency for chloride formation at 3000°C, above which carbon sublimation would be a problem. Even if this efficiency were achieved, in order to do reactive scattering some auxiliary means of analysis such as magnetic deflection would probably have to be used, since the detector in general could not distinguish the precursor of an ion signal.

Nevertheless, this method could be useful in elastic scattering studies and as a beam monitor because of its relative simplicity. Although negative surface ionization itself involves interesting chemical processes worthy of further study, its attractiveness as a molecular beam detection scheme, especially in reactive scattering, is severely limited.

APPENDIX A

List of Apparatus Mechanical Drawings and LBL Numbers*

1. Vacuum chambers

   A. Collision chamber

main chamber	12N 2746
side flanges (2)	12N 2833
back flange	12N 2843
liquid nitrogen reservoir	12N 2804
liquid nitrogen shield chassis	12N 2784
liquid nitrogen fill tube	12N 2913
side flange liquid nitrogen shields (2)	12N 2863
back flange liquid nitrogen shield	12N 2823
oil diffusion pump baffle (2)	12N 2962
ion gauge flange	12N 2952
chamber support stand	12N 2933
adapter to high temperature oven chamber	12N 2764

   B. High temperature oven chamber

main chamber	12N 2754
side flanges (2)	12N 2923
back flange	12N 2794
liquid nitrogen fill flange	12N 2903
liquid nitrogen reservoir	12N 2943

---

* These drawings are filed at the Lawrence Berkeley Laboratory; copies of LBL drawings whose numbers are cited here may be obtained by writing to Lawrence Berkeley Laboratory, Technical Information, Building 90, Room 3118, Berkeley, California 94720.

liquid nitrogen shield chassis	12N 2774
side flange liquid nitrogen shields (2)	12N 2893
back flange liquid nitrogen shield	12N 2883
adapter to collision chamber	12N 3812
flange to adapter	12N 3153
pump baffle	12N 2853
chamber support stand	12N 2873
corrosive gas exchanger	12N 3193
liquid nitrogen cold traps (2)	12N 3203

2. Ovens

high temperature oven	12N 4693
oven support copper blocks	12N 4682
ceramic adaptor	12N 4672
gas source oven	12N 3162

3. Detector chamber

detector chamber	12N 2814
detection chamber - lower section	12N 4714
lid modification	12N 3823
detection chamber cold shroud	12N 4053
small sublimator unit	12N 3693
sublimator cold shield	12N 3682
slide valve	12N 4652
slide valve plate	12N 4662

4. Ionizer

grid	12N 4002
shield	12N 3982
extractor and lens assembly	12N 4012
frame and exit aperture	12N 3992
quadrupole mass filter mount	12N 4032

APPENDIX B

List of Apparatus Electronic Diagrams and LBL Numbers

System wiring diagram	8S 8405
Dual liquid nitrogen level control	8S 7252
Single vacuum interlock (2)	8S 2803-1A
Hastings gauge dual vacuum interlock	6z 4664E
Hastings gauge dual vacuum interlock	5z 4994-1D
Ion gauge 5 position switching panel	8S 7392
High temperature oven power supply	8S 7351

REFERENCES

1. Shen-Maw Lin, Ph.D. Thesis, University of California, Berkeley, 1972.

2. C. A. Mims, S.-M. Lin, and R. R. Herm, J. Chem. Phys. 57, 3099 (1972).

3. S.-M. Lin, C. A. Mims, and R. R. Herm, J. Chem. Phys. 58, 327 (1973).

4. Y. T. Lee, J. L. McDonald, P. R. LeBreton, and D. R. Herschbach Rev. Sci. Instr. 40, 1402 (1969).

5. H. Pauly and J. P. Toennies, Advan. At. Mol. Phys. 1, 195 (1965).

6. Brunswick Corp. (Tech. Prod. Div., Skokie, Illinois) makes a stainless steel array with 12μ channel dia., for example.

7. R. Weiss, Rev. Sci. Instr. 32, 397 (1961).

8. G. O. Brink, Rev. Sci. Instr. 37, 857 (1966).

9. S. Datz and E. H. Taylor, J. Chem. Phys. 25, 389 (1956).

10. a. QUAD 250 Operating Manual, Electronics Associates, Inc., Palo Alto, California.

    b. W. Paul, H. Reinard, and V. Von Zahn, Z. Phyzik. 152, 143 (1958).

11. C. Batalli-Cosmovici, and K. W. Michel, Chem. Phys. Lett. 11, 245 (1971).

12. K. R. Spangenberg, Vacuum Tubes (McGraw Hill, New York, 1948), Chapter 13.

13. a. N. C. Blais and J. B. Cross, J. Chem. Phys. 52, 3580 (1970).

    b. N. C. Blais and J. B. Cross, J. Chem. Phys. 55, 3970 (1971).

14. a. D. D. Parrish and R. R. Herm, J. Chem. Phys. 51, 5467 (1969).
b. D. D. Parrish and R. R. Herm, J. Chem. Phys. 54, 2518 (1971).

15. N. F. Ramsey, Molecular Beams (Oxford University Press, London, 1963).

16. J. A. Haberman, K. G. Anlauf, R. B. Bernstein, and F. J. Van Itallie (to be published).

17. L. T. Crowley, M. A. D. Fluendy, and K. D. Lowley, Rev. Sci. Instr. 41, 666 (1970).

18. a. J. H. Bireley, R. R. Herm, K. R. Wilson, and D. R. Herschbach, J. Chem. Phys. 47, 933 (1967).
b. G. H. Kwei, J. A. Norris, and D. R. Herschbach, J. Chem. Phys. 52, 1317 (1970).

19. R. R. Herm, private communication.

20. K. T. Gillen, C. Riley, and R. B. Bernstein, J. Chem. Phys. 50, 4019 (1969).

21. A. M. Rulis, Ph.D. Thesis, University of Wisconsin, 1972.

22. a. J. A. Giordmaine and T. C. Wang, J. Appl. Phys. 31, 463 (1960).
b. D. R. Olander, R. H. Jones and W. J. Siekhaus, J. Appl. Phys. 41, 4388 (1970).
c. W. J. Siekhaus, R. H. Jones, and D. R. Olander, J. Appl. Phys. 41, 4392 (1970).

23. J. B. Anderson, R. P. Andres, and J. B. Fenn, Adv. Chem. Phys. 10, 275 (1966).

24. I. Estermann, O. C. Simpson, and O. Stern, Phys. Rev. 71, 238 (1947).

25. J. H. Bireley and D. R. Herschbach, J. Chem. Phys. 44, 1690 (1966).

26. C. Sholeen and L. Gundel (unpublished data).

27. For a review of the theory and experimental work in positive surface ionization see:

    a. E. Ya. Zandberg and N. I. Ionov, Vsp. Fiz. Nauk 57, 581 (1959).

    b. M. Kaminsky, Atomic and Ionic Impact Phenomena on Metal Surfaces (Academic Press Inc., New York, 1965), pp. 98-142.

28. M. Scheer and J. Fine, Proc. 6th Int. Symp. on Rarified Gas Dynamics (Academic Press, New York, 1969).

29. J. W. Trischka, D. T. F. Marple, and A. White, Phys. Rev. 85, 136 (1952).

30. A. Persky, E. F. Greene, and A. Kupperman, J. Chem. Phys. 49, 2347 (1968).

31. J. T. Herron, H. M. Rosenstock, and W. R. Shields, Nature 206, 6111 (1965).

32. E. E. Muschlitz, private communication, reports seeing NO_2^- and CNO^- from CCl_3NO_2.

33. J. L. G. Dugan, D. Stelman, and E. E. Muschlitz, First Annual Meeting, DEAP of APS, November 17-19, 1969.

34. F. Rosebury, Handbook of Electron Tube and Vacuum Techniques (Addison Wesley, Reading, Massachusetts, 1965).

35. C. S. Harden, D. Stelman, and E. E. Muschlitz, Jr., 14th Annual ASTM Conference, 1966.

36. Handbook of Physics and Chemistry lists values ~4.5 e.v.

37. R. E. Honig, J. Chem. Phys. 22, 126 (1954).

38. I. Langmuir, J. Am. Chem. Soc. 37, 1139 (1915).

39. G. A. Somorjai, Principles of Surface Chemistry (Prentice-Hall, Englewood Cliffs, New Jersey, 1972).

40. M. J. Cardillo, M. S. Chou, E. F. Greene, and D. B. Sheen, J. Chem. Phys. 54, 3054 (1971).

III. CROSSED BEAMS COLLISION MECHANICS OF KINEMATICALLY RESTRAINED REACTIONS

A. Introduction

The K + HBr → KBr + H reaction was the first studied by the crossed molecular beam technique.[1] Reactions of A + HB → AB + H where the masses of both A and B greatly exceed that of the hydrogen atom are kinematically unique in that the nature of the transformation between the laboratory (LAB) and center-of-mass (CM) coordinate systems requires[2] that the AB product appear in the LAB system with a velocity close to that of the velocity of the center-of-mass of the collision partners, $\vec{C}$. Two other types of reactions in which the products are even more kinematically restrained than the above are Penning ionization and radiative recombination, where the lighter "products" formed are an electron and photon respectively. This restriction makes it extremely difficult to elucidate the reaction CM energy and angle recoil distributions from measurements of the AB flux in the LAB, although Bernstein and co-workers[3] did manage to do so for the K + DBr reactions in an elegant experiment employing a velocity selected K beam and velocity analysis of the KBr product. However, this kinematic restriction on these reactions makes possible the determination of the dependence of the reaction cross section, Q, on relative kinetic collision energy, E, by means of an experiment in which the two reactant beams are crossed with known velocity distributions. Here one argues that the heavy AB product which is detected must essentially recoil (in the LAB) along $\vec{C}$

and exploits the broad distribution in E by proceeding to calculate the angular distributions of $\vec{C}$ for various assumed forms of Q(E). The requisite theory was developed in Reference 2 for a crossed thermal beams experiment in which the LAB flux of AB product is measured and was applied to the data reported in Reference 1 for the K + HBr reaction. This resulted in an estimated threshold relative kinetic energy, E*, of ~2.5-3 kcal/mole, although the agreement of the experimental data with the theoretical curve was not very good. A much smaller value of E* for this K + HBr reaction was obtained in a more recent[4] measurement of the KBr flux formed upon crossing a velocity selected K beam by a thermal HBr beam. A recent crossed thermal beams experiment of the type analyzed in Reference 2 has reported[5] E* ~ 2-3 kcal/mole for the K + HCl → KCl + H reaction. In this chapter, measured LAB angular distributions of product MI (M = Ba, Sr, or Ca) from the reaction M + HI → MI + H are reported; from the analysis of these, estimates of E* and rigorous lower limits on D°_{o} (MI) are obtained. Reactions of M with other hydrogen halides were also attempted and the results are discussed.

B. Experimental Procedure

The apparatus described in the previous chapter was used without modification. The HI was supplied from a lecture bottle purchased from Matheson Co. and maintained at a reservoir pressure of ~2 torr by a Granville Phillips leak valve. The HI beam gas flow rate was ~4 torr ℓ/min, and produced a rather high collision chamber pressure ($\sim 4\times10^{-6}$ torr),

which was probably due to H_2 impurity in the beam. This is of no consequence, inasmuch as the beam profiles were not measurably broadened, but any concomitant I_2 impurity would be troublesome because it produces significant (relative to the HI contribution) alkaline earth iodide scattered signal. Contributions from scattering from I_2 were shown to be negligible (1) by the absence of an I_2 signal in the mass spectrum of the HI beam and (2) by checking that no alkaline earth iodide was scattered into negative LAB angles.

It is appropriate to comment here on the detector response. If c is the "rate constant" for electron bombardment ionization in the ionizer, then the probability that a molecule will pass through without being ionized is e^{-ct} if it spends an amount of time t traversing the ionizing region. Therefore, the ionization efficiency $\beta = 1 - e^{-ct}$, if successive processes such as second ionization, electron attachment, etc. are neglected. If ct is small, then $\beta \cong ct$ and is thus proportional to the residence time in the ionizer; under these conditions, β is then proportional to the reciprocal of velocity and the detector measures the number density (rather than the flux) of the molecules. This is true for all electron bombardment ionizers now in use, for all velocities of interest in molecular beam scattering. In the happy event that an ionizer is invented which is 100% efficient for all velocities of interest, the flux density expressions in Reference 2 will then be applicable to the molecular beam "supermachine".

C. Crossed Beams Collision Mechanics

In the following section, we wish to compare the measured alkaline earth iodide angular distributions with calculated angular distributions of centroid vectors. Although theoretical expressions for the flux density angular distributions of centroid vectors are given in Reference 2, the corresponding expressions for the number density distributions are not available in the literature and are discussed here.

1. General Formulation

The calculation of the number density distributions of $\vec{C}$ is a straightforward extension of the methods and results given in Reference 2; accordingly, the nomenclature employed in Reference 2 is retained here. Two beams of particle masses M_1 and M_2 are assumed to collide at an angle γ defining an intersection volume τ. The relative collision velocity, $\vec{V}$, relative collision energy, E, and center-of-mass velocity, $\vec{C}$, are defined in terms of the velocities of particles in beams 1 and 2, $\vec{v}_1$ and $\vec{v}_2$, by:

$$\vec{V} = \vec{v}_1 - \vec{v}_2 \ , \tag{1a}$$

$$M\vec{C} = M_1\vec{v}_1 + M_2\vec{v}_2 \ , \tag{1b}$$

and

$$E = \mu V^2/2 \ , \tag{1c}$$

where the mass factors are given by

$$M = M_1 + M_2 \tag{2a}$$

and

$$\mu = M_1M_2/M \ . \tag{2b}$$

Fig. III-1. The data points show measured LAB angular distributions of BaI product of the Ba + HI reaction; nominal beam temperatures: 1033°K (Ba) and 363°K (HI). The solid curve gives the number density angular distribution of $\vec{C}$, $B(\theta)$, calculated from Eq.(7) for reaction model B (Eq. (14b)) for $E^* = 2.5$ kcal/mole by numerical integration over the experimentally measured speed distributions in the two beams. Also shown are angle profiles of the two beams as well as a LAB $\leftrightarrow$ CM transformation diagram for the Ba + HI reaction. This is drawn for the $\gamma = 90°$ intersection angle employed in this work and for the Ba and HI most probable beam speeds and shows the relative collision velocities, $\vec{V}$, and velocity of the center-of-mass, $\vec{C}$. The circles are drawn for BaI CM recoil speeds corresponding to typical possible product recoil energies, E', of 1, 3, 6, and 10 kcal/mole.

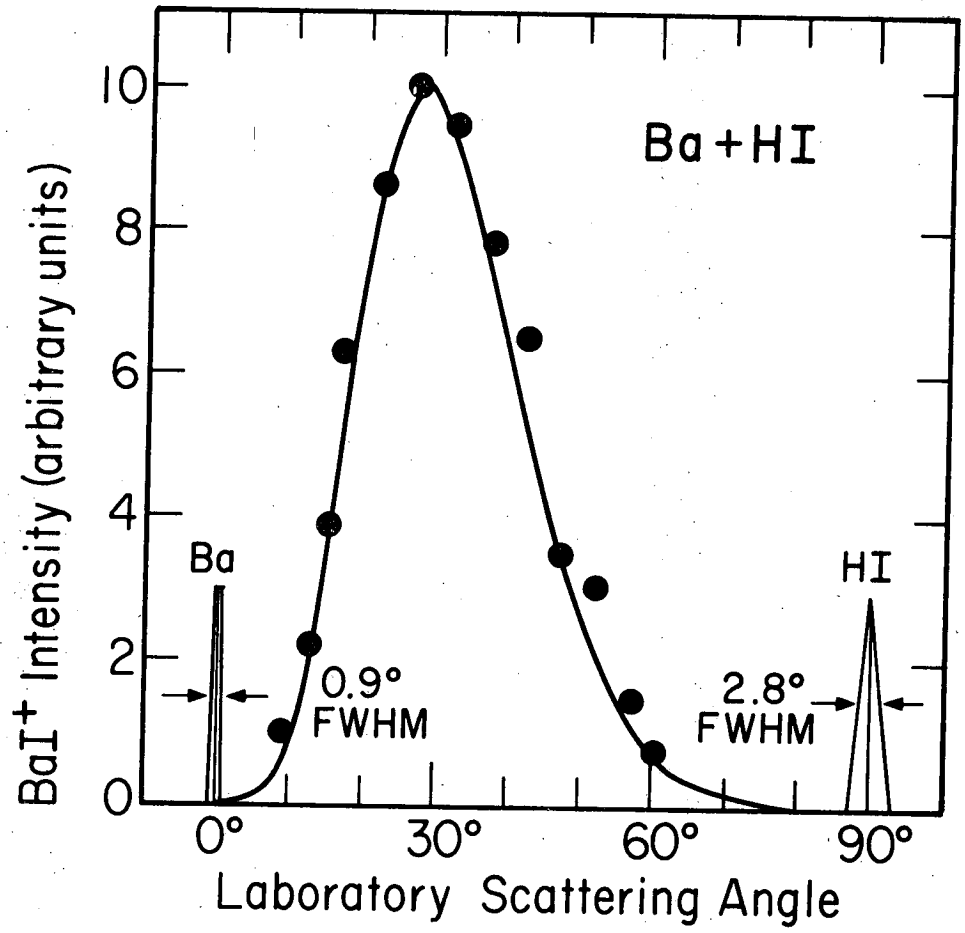

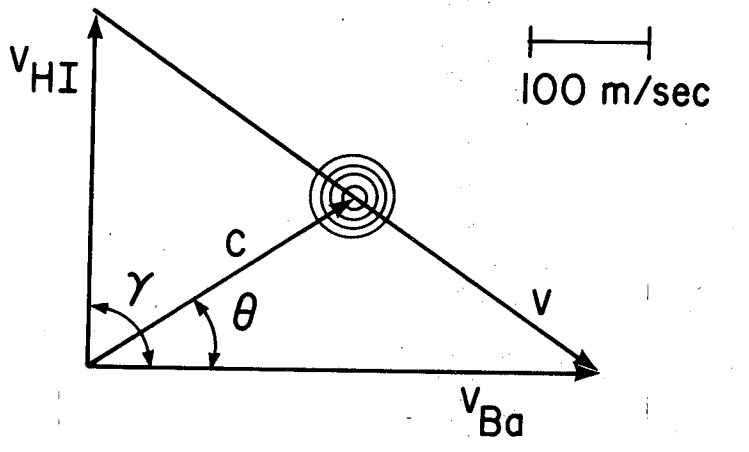

XBL 726-6372

Fig. III-1.

Figure III-1 includes a transformation diagram illustrating the relations of $\vec{v}_1$, $\vec{v}_2$, $\vec{V}$, $\vec{C}$, and θ, the angle between $\vec{v}_1$ and $\vec{C}$.

The number of reactive events per second, N, may be written in terms of the number densities of beams 1 and 2 at the collision zone, n_1 and n_2, as

$$N = n_1 n_2 \tau \int_0^\infty \int_0^\infty Q(V) V \rho_1(v_1) \rho_2(v_2) dv_1 dv_2 \ , \qquad (3)$$

where ρ_1 and ρ_2 are the number density probability density speed distribution functions for beams 1 and 2. This may also be written as

$$N = \int_0^\gamma \int_0^\infty P(\theta,C) dC d\theta \qquad (4)$$

where $P(\theta,C)dCd\theta$ is the number of reactive collisions per second with center-of-mass speed between C and C+dC and direction between θ and $\theta+d\theta$. Equating N in Eqs.(3) and (4), $P(\theta,C)$ may be written as

$$P(\theta,C) = n_1 n_2 \tau Q(V) V \rho_1(v_1) \rho_2(v_2) M^2 C / M_1 M_2 \sin \gamma; \qquad (5)$$

V, v_1, and v_2 may be expressed as functions of θ and C by means of the transformation equations given in Reference 2. Integration of $P(\theta,C)$ over C yields the flux angular distribution of $\vec{C}$ which would be measured by a flux detector (e.g. a surface ionization detector). However, it seems likely that most molecular beam studies of non-alkali scattering will employ an electron bombardment ionization detector, as is the

case here. As has been noted, the electron bombardment ionizer is a number density detector so that the appropriate centroid distribution function becomes

$$B(\theta,C) = \delta P(\theta,C)/C \ , \tag{6}$$

where δ is a constant characterizing the detector sensitivity. The angular distribution of $\vec{C}$ appropriate to experiments employing a number density detector is then given by

$$B(\theta) = \int_0^\infty B(\theta,C)dC \ . \tag{7}$$

2. Crossed Thermal Beams

The expressions for $B(\theta,C)$ and $B(\theta)$ are especially simple in the case of two crossed beams with thermal speeds distributions. Although the beams in this experiment do not have thermal distributions (see Chapter II), these expressions should be of general interest to molecular beam experimentalists. For this thermal case, $B(\theta,C)$ becomes

$$B(\theta,C) = \beta Q(MC/m)F(\theta)\, C^5 \exp[-M^2C^2/m^2\alpha^2] \ , \tag{8}$$

where $F(\theta) = m^{-1} \sin^2(\gamma-\theta) \sin^2\theta/\sin^5\gamma$;

$MC/m = V$; $\beta = 16\delta n_1 n_2 \tau M^7/\pi M_1^{\,3} M_2^{\,3} \alpha_1^{\,3}\alpha_2^{\,3}$;

and α_1 and α_2 are the most probable thermal source speeds, $\alpha_i = (2kT_i/M_i)^{1/2}$. Equation (8) is written in terms of the velocity

independent, angle dependent "effective mass" m and "effective thermal source speed" α derived in Reference 2 as:

$$m^{-2}\sin^2\gamma = \frac{\sin^2(\gamma-\theta)}{M_1^2} - \frac{2\cos\gamma\sin(\gamma-\theta)\sin\theta}{M_1M_2} + \frac{\sin^2\theta}{M_2^2} ; \quad (9)$$

$$\alpha^2 = \frac{\sin^2\gamma}{m^2}\left\{\frac{\sin^2(\gamma-\theta)}{M_1^2\alpha_1^2} + \frac{\sin^2\theta}{M_2^2\alpha_2^2}\right\}^{-1} . \quad (10)$$

Molecular beam experimentalists may occasionally want to employ Eq.(8) or its flux counterpart directly. Thus, assuming that Q(E) were known, comparison of Eq.(8) with measured LAB velocities of the AB product of the kinematically constrained A + HB reaction would provide a check against systematic apparatus errors. Additionally, this equation indicates the distribution in origin of the CM coordinate system and might be useful in estimating the loss of resolution in CM cross sections which results from the LAB → CM transformation for the case of crossed thermal beam experiments.

In analogy with observations in Reference 2, $B(\theta)$ obtained by substitution of the $B(\theta,C)$ expression of Eq.(8) into Eq.(7) is naturally expressed as

$$B(\theta) = (\beta/2)(m/M)^6 F(\theta) G(\alpha^{-2}) \quad (11)$$

in terms of the Laplace transform

$$G(\alpha^{-2}) = \int_0^\infty \exp(-t/\alpha^2)t^2 Q(t)\, dt \quad (12)$$

where $t = V^2 = 2E/\mu$. In the case of a constant cross section Q_o, independent of E, $G(\alpha^{-2}) = Q_o 2\alpha^6$, and

$$B_o(\theta) = Q_o \beta (m/M)^6 F(\theta) \alpha^6 . \qquad (13)$$

Since the cross section for elastic scattering is generally a weak function of energy, $B_o(\theta)$ represents the angular distribution of centroid vectors for all the collisions between the two beams. Figure III-2 shows plots of $B_o(\theta)$ for various angles of intersection; the beam masses and temperatures correspond to the conditions for the Ba + HI reaction. Since the Ba effuses from a hotter source (T_{Ba} = 1030°K, T_{HI} = 360°K) the Ba beam has more average momentum, and all the $B_o(\theta)$ curves favor angles close to the Ba beam. For beams with similar momenta, the $B_o(\theta)$ curves become more symmetric about $\gamma/2$ and exhibit bimodal behavior for very large (150°) and very small (30°) intersection angles. The bimodal behavior for large angles is found in the flux expressions, but for small γ, is a result of the relative insensitivity of the number density detector to the faster moving molecules at $\gamma/2$.

3. Reaction Cross Sections

Consider now two simple forms of Q(E). The first of these is a step-function model (Model A) in which one assumes that Q(E) is finite and of constant value Q_o only if E exceeds E*, a reaction threshold energy. Thus, in terms of u(t), the unit step-function, model A is given by

Fig. III-2. Number density angular density distribution of centroids, $B_o(\theta)$ for various angles of intersection of the two beams. These have been calculated for the beam conditions used for Ba + HI in this chapter. The curves for $\gamma = 30°$ and $150°$ have been multiplied by a factor of 8. These represent what would be measured by a detector with constant resolution in angle θ. For $B_o(\theta/\gamma)$ the curves must be multiplied by a factor of γ.

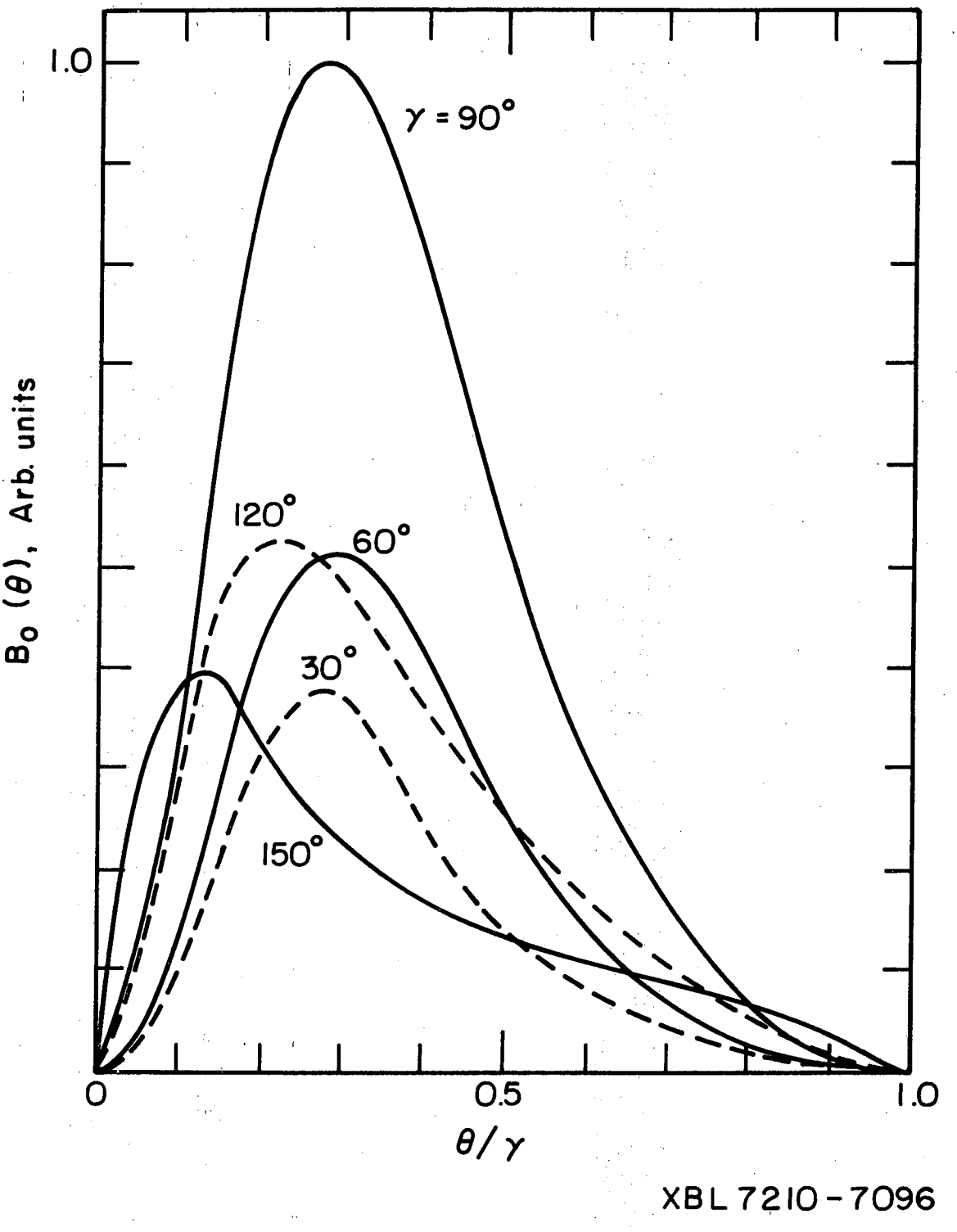

Fig. III-2.

$$Q_A(E) = Q_o\, u(E-E^*) \,. \tag{14a}$$

Model B assumes instead a step-function dependence on the components of collision energy directed along the line-of-centers at impact so that

$$Q_B(E) = Q_o\, [1-(E^*/E)]\, u(E-E^*). \tag{14b}$$

Model B is the well-known form of Q(E) which results in a simple Arrhenius temperature dependence of the kinetic rate constant for the more conventional experiment employing a gas thermally equilibrated in a reservoir. Figure III-3 includes a comparison of the Q(E) dependence for Models A and B.

The Laplace transform in Eq.(12) is known[6] for these two forms of Q(E), and the resulting B(θ) expressions obtained from Eq.(11) become

$$B_A(\theta) = B_o(\theta) \left[1 + \frac{V^{*2}}{\alpha^2} + \frac{V^{*4}}{2\alpha^4}\right] \exp(-V^{*2}/\alpha^2) \tag{15a}$$

and

$$B_B(\theta) = B_o(\theta) \left[1 + \frac{V^{*2}}{2\alpha^2}\right] \exp(-V^{*2}/\alpha^2) \tag{15b}$$

where $V^* = \sqrt{2E^*/\mu}$.

One can extend this treatment in a manner parallel to that of Reference 2 by considering a generalized cross section of the type

$$Q(E) = Q_o \sum_n c_n (E^*/E)^n\, u(E-E^*) \tag{16}$$

The constants c_n may be adjusted as parameters and should be able to represent any desired form of the cross section. Models A and B are

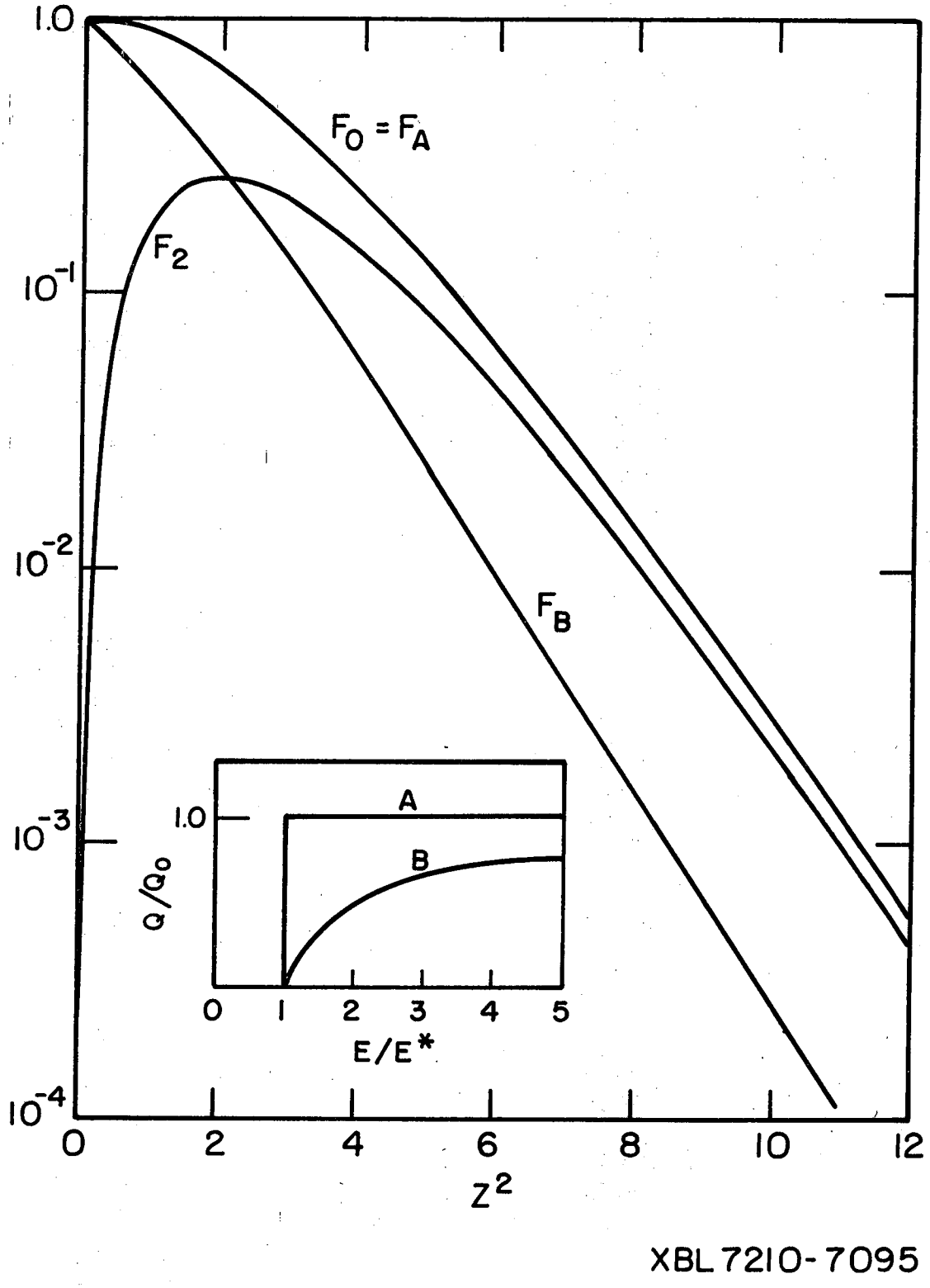

Fig. III-3. Attentuation functions corresponding to various values of n in Eq.(23). Insert shows energy dependence of models A and B.

special cases of Eq.(16): for model A, $c_o = 1$; for model B, $c_o = 1$, and $c_1 = -1$. For a cross section of the form of Eq.(16), $G(\alpha^{-2})$ can take the form

$$G(\alpha^{-2}) = Q_o \sum_n c_n G_n(\alpha^{-2}) \tag{17}$$

where

$$G_n(\alpha^{-2}) = 2 \int_{V^*}^{\infty} \left(\frac{V^*}{V}\right)^{2n} V^5 \exp(-V^2/\alpha^2)\, dV \tag{18}$$

which can be conveniently expressed in terms of an incomplete gamma function[7]

$$G_n(\alpha^{-2}) = \alpha^6 z^{2n} \Gamma(3-n, z^2), \tag{19}$$

where $z \triangleq V^*/\alpha$, and

$$\Gamma(a,x) = \int_x^{\infty} e^{-t} t^{a-1}\, dt . \tag{20}$$

To determine the effects of the energy dependence of the cross section on $B(\theta)$, the constant cross section part may be factored out:

$$B(\theta) = B_o(\theta) F(z) \tag{21}$$

$$G(\alpha^{-2}) = 2\alpha^6 Q_o F(z) \tag{22}$$

$F(z)$ is considered an attenuation factor inasmuch as it is the part of $B(\theta)$ which depends on the functional form of $Q(E)$. Thus, it represents the premium placed on the relative energy by the cross section. $z^2 = V^{*2}/\alpha^2$ is a measure of the inverse of the available relative energy.

Because of Eq.(16),

$$F(z) = \sum_n c_n F_n(z) \tag{23}$$

and from Eq.(19)

$$F_n(z) = \tfrac{1}{2} z^{2n} \Gamma(3-n, z^2) \tag{24}$$

For n = 2 the integral in Eq.(24) is simple and yields

$$F_2(z) = \tfrac{1}{2} z^4 e^{-z^2} \tag{25}$$

and from recurrence relations of gamma functions[7] the following recurrence relation results:

$$z^2 F_{n-1}(z) = (3-n) F_n(z) + \tfrac{1}{2} z^4 e^{-z^2} \tag{26}$$

Thus, F(z) can be generated for any cross section with energy dependence represented by Eq.(16). Figure III-3 shows attenuation factors for the reaction models A and B and also for one which decreases above threshold. They are quite similar to those shown in Reference 2, and all approach the same behavior at large values of E* (within a scale factor).

Now all one needs to do is calculate z as a function of θ, using Eq.(10) and the fact that $z = V^*/\alpha$. Once this is done, $B(\theta)$ curves for any cross section represented by Eq.(16) can be calculated and compared with experimental data. Even in the case of reactions which are not kinematically restrained, these expressions should be useful to molecular beam experimentalists, as a comparison of a measured LAB

product angular distribution with $B(\theta)$ allows one to quickly estimate the tendency of the reaction to scatter the product into the forward versus the backward hemisphere in the CM coordinate system.

While the calculations of $B(\theta)$ from a given energy dependent cross section is straightforward, the inversion of experimental data to deduce the functional form of $Q(E)$ is not. If one obtains measured LAB angular distributions of a kinematically restrained product which are normalized, i.e. all detector response factors are known, or alternatively are normalized to theoretically calculable elastic scattering, then one can back-calculate attenuation factors $F(z)$ by assuming a value for E^*. Then one can vary E^* until the calculated $F(z)$ curve agrees with that for some reaction model. This method is equivalent to that of calculating $B(\theta)$ curves using assumed forms of $Q(E)$ and varying E^*, and possibly $Q(E)$, until good fits to the laboratory data are obtained. In general, however, several $F(z)$ curves can be fit this way, i.e. several forms of $Q(E)$ will provide adequate fits to the data. This is evidenced by the fact that the best model B fit to the data in this chapter can be duplicated by a model A fit with a slightly higher threshold energy.

The situation is much better when LAB angular distributions are taken with two angles of intersection. Then one can vary E^* until the calculated $F(z)$ forms agree for the two runs. This should be more sensitive also in that $z(\theta)$ can vary dramatically in functional form and magnitude for different angles of intersection (see Figure 4 in Reference 2).

Two experimental variations provide more straightforward means to deduce Q(E). The first employs velocity analysis of the product AB and by comparison of the measured data with Eq.(8) one could obtain Q(E), since only one value of V is specified by one value of the coordinates θ and C. The second method employs a monoenergetic velocity distribution for one of the beams and compares the LAB distribution with a theoretical expression which is easily calculated by means of Eq.(6). This method is also quite simple, after one has produced a monoenergetic beam, because each value of θ represents only one value of V.

In the case of the present experiments, however, one must assume a likely form for Q(E) and calculate $B(\theta)$ curves to compare with experimental data, varying E* and perhaps Q(E) until a good fit to the measured angular distribution is obtained. For both models the effect of an increase in E* on the calculated $B(\theta)$ curves here was to decrease their breadth and shift the peak toward the hotter alkaline earth beam.

D. Experimental Results

The LAB $\leftrightarrow$ CM transformation diagram for the Ba + HI reaction which is included in Fig. III-1 indicates that the LAB BaI scattering velocity could deviate significantly in direction from that of $\vec{C}$. The maximum possible deviation may be estimated from the largest BaI CM recoil speed shown in the diagram, as the reaction is unlikely to be exothermic by more than the ~10 kcal/mole exothermicity of the analogous Cs + HI reaction. The extent of possible deviations for the Sr and

Ca reactions should resemble that for the Ba reaction because the decreasing M_{MI}/M_H mass ratio is offset by the likely decrease in the reaction exothermicities. This deviation might render the E* estimates somewhat low in that part of the breadth of the LAB curve could be a result of this "smearing". However, two arguments suggest that the deviations between the directions of $\vec{C}$ and the LAB MI velocities should be insignificant: (1) the product KBr velocity analysis experiments reported in Reference 3b indicate that a large fraction of the reactions of K with HBr and DBr produce low product recoil energies, E'; and (2) the peak in the LAB MI angular distribution is most sensitive to reactions producing low E' values because of the form of the Jacobian of the CM → LAB transformation. As an additional argument against a significant deviation from $\vec{C}$, MI LAB angular distributions for the Ca, Sr, and Ba + HI reactions were calculated for various assumed CM angular and E' distributions by numerical integrations of the CM → LAB transformation. The calculated MI LAB angular distributions were always broader than the calculated angular distributions of $\vec{C}$, although the additional breadths were negligible unless the E' values were predominantly confined to values greater than ~5 kcal/mole.

1. The Beam Speed Distributions

The measured LAB BaI, SrI, and CaI product angular distributions are shown in Figures III-1 and III-4. Most of the foregoing theory, unfortunately, is inapplicable to these data because of the non-thermal behavior of the beams. As related in the previous chapter, the beam

velocity distributions were measured and the measurements are well fit by an HI number density speed probability distribution of the form

$$\rho_2(v_2) = (v_2-a_2)^2 \exp[-(v_2-a_2)^2/\alpha_2^2]\, u(v_2-a_2) \qquad (27)$$

where α_2 is still α_0, the most probable thermal source speed and u(t) is the unit step function. The parameter a_2, increases with increasing HI source pressure; for the 2 torr source pressure employed here the speed distribution is considerably non-thermal with $a_2 = 0.45\ \alpha_2$. This value was obtained by extrapolating the one measured point for HI along the family of curves in Figure II-12. In view of this non-thermal behavior it is not surprising that attempts to fit the data with $B(\theta)$ curves calculated by means of Eqs.(15a) and (15b) were unsuccessful.

As reported in the previous chapter, the measured Ba beam distribution is much closer to thermal behavior and was also fit by Eq.(27) except that α_1 (see Chapter II) is now given by 0.89 times α_o, the most probable thermal source speed, and $a_1 = 0.33\ \alpha_1$. The same distribution in reduced velocity, v/α_o, was used for Ca and Sr as well, for reasons explained in Chapter II. As was stated, this could possibly overestimate the non-thermality of the Ca and Sr distributions, but in practice, this uncertainty is inconsequential because $B(\theta)$ curves calculated from thermal atom beams were indistinguishable from the ones using Eq.(27).

2. Reaction Threshold Energies

Angular distributions of $\vec{C}$ were calculated from Eq.(7) by numerical integration over the measured beam speed distributions. The solid

Fig. III-4. Data points give measured product LAB angular distributions of SrI and CaI; different data point symbols for CaI show results measured on different pumpdowns; nominal beam temperatures: 953°K and 348°K for Sr + HI; 1020°K and 328°K for Ca + HI. Also shown are $B(\theta)$ curves calculated as described for Fig. III-1 for: Sr + HI for $E^* = 4$ kcal/mole (solid); and Ca + HI for $E^* = 3$ (dash), 5 (solid) and 7 (dash-dot) kcal/mole. the $B(\theta)$ function calculated for $E^* = 4$ kcal/mole and reaction model B for intersecting Sr and HI beams with thermal speed distributions is also shown (dash curve).

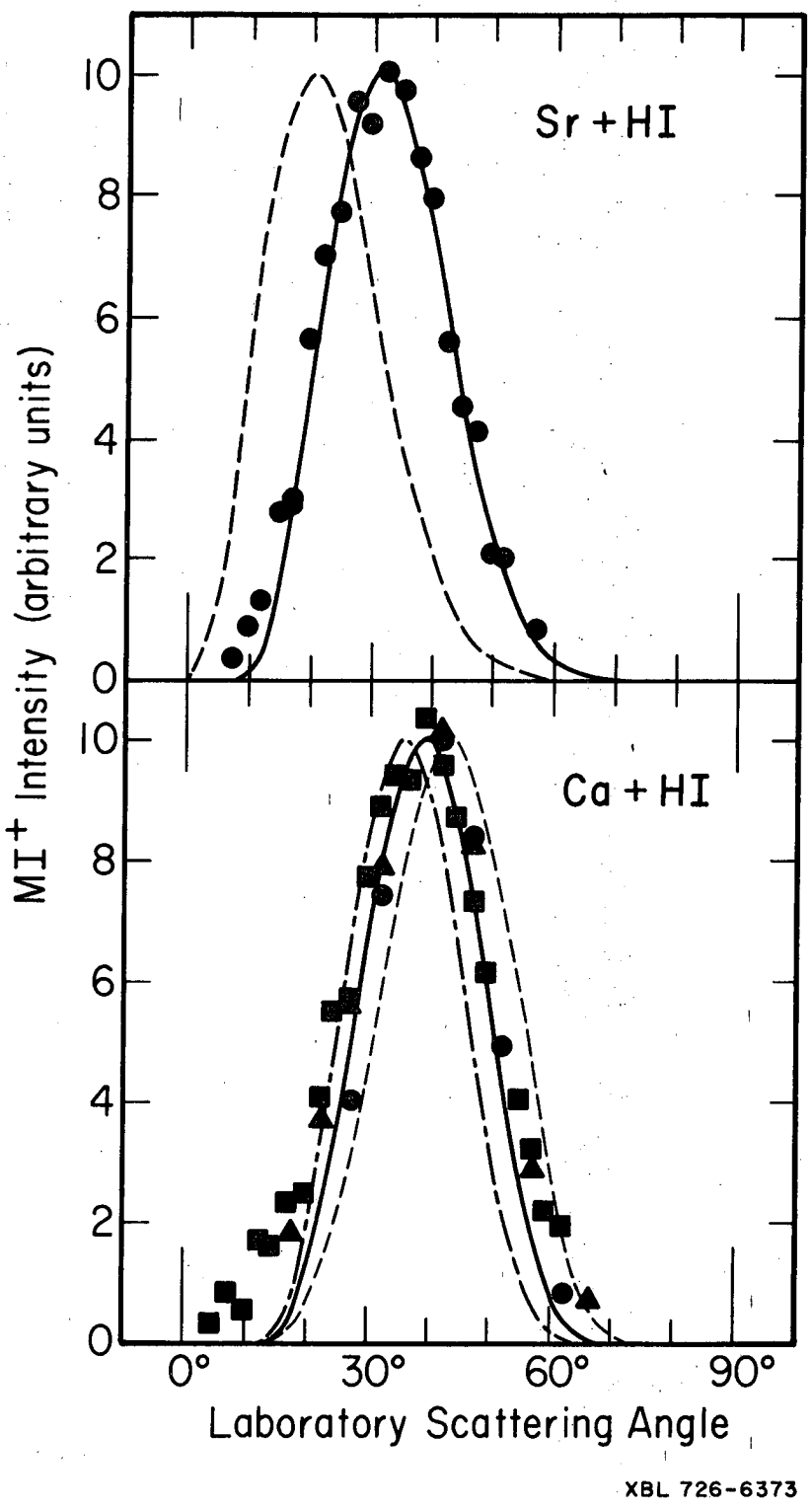
Sr + HI
Ca + HI
MI^+ Intensity (arbitrary units)
0
2
4
6
8
10
0°
30°
60°
90°
Laboratory Scattering Angle
XBL 726-6373

Fig. III-4.

curves in Figs. III-3 and III-4 show the $B(\theta)$ functions calculated from E^* values which best fit the data, using reaction model B (Eq.(14b)).

In general, the fits of the theoretical $B(\theta)$ curves to the measured MI signals which are shown in Figs. III-3 and III-4 are very good, much better than were obtained in previous studies of the K + HBr [2] and HCl [5] reactions. The small positive deviations of the measured MI signals from the calculated $B(\theta)$ curves which are apparent at small LAB angles in Figs. III-1 and III-4 are probably a consequence of Eq.(27). which unrealistically assumes zero probability for very small HI speeds and thereby renders the calculated $B(\theta)$ curves absolutely zero at small θ values.

The Sr + HI panel in Fig. III-4 also shows a $B(\theta)$ curve calculated for two thermal beam speed distributions and reflects the sensitivity of the $B(\theta)$ calculations to the true HI beam speed distribution. In general, when thermal distributions were used to calculate $B(\theta)$ curves, the peak was shifted too close to the Ba beam for values of E^* which gave good fits to the widths of the LAB data. Similar problems have been reported by other workers[5,8] attempting to analyze alkali metal M + HX reactions. These studies also used multichannel sources for the HX beam, and assumed the beams to be thermal. This is probably the source of their difficulties.

The Ca + HI panel in Fig. III-4 includes calculations of $B(\theta)$ curves for three different values of E^* in order to indicate the sensitivity of the fit to the data to the E^* value; the Ca + HI data is the least sensitive to changing E^* values because this reaction has the

highest threshold energy. In general, reaction cross section model A (Eq.(13a)) provides $B(\theta)$ curves which fit the data as well as the model B calculations illustrated in the figures; model A provides best fits for E* values slightly larger (~0.5 kcal/mole) than those obtained from model B fits. Table I lists the E* values which best fit the data shown in Figs. III-1 and III-2; the uncertainties in E* listed in the table reflect the differences between model A and B fits as well as the range in E* values which adequately fit the data for calculations for one reaction model.

3. Other Reactions

Reactively scattered signal of BaBr was measured from the reaction of Ba and HBr but the poor quality of the data precluded any analysis for threshold energy. This was due in part to high apparatus pressures due to the vapor pressure of HBr at liquid nitrogen temperature ($\sim 10^{-5}$ torr). If Q_o for this reaction is comparable to that of Ba + HI, the absolute LAB signal levels indicate that E* could not be much greater than ~5 kcal/mole.

No reactively scattered MX signals were observed from crossed beams of either Mg and HI or Ba and HF. If one assumes that the Q_o constants in Eq.(13) for these reactions are comparable to those for Ca, Sr, and Ba + HI, this inability to observe reaction in the apparatus employed here would imply that E* > 8-10 kcal/mole for these two reactions. This might simply be a consequence of the Mg + HI reaction energetics, as D_o° (MgI) is not known well, but is likely[9,10] to be considerably

Table I. M + HX → MX + H reaction threshold energies and lower limits for $D_o^\circ(MI)$ [a]

Alkaline earth halide, MX	Measured threshold relative collision energy, E*	$D_o^\circ(MX)$ estimates of Reference 9	Lower limits for $D_o^\circ(MX)$ provided by this work
CaI	5 ± 1	75 ± 15	64
SrI	4 ± 1	80 ± 15	65
BaI	2.5 ± 1	85 ± 15	66
BaBr	< 8 [b]	100 ± 15	77

[a] All energies given in kcal/mole.

[b] Not measured; estimated from signal intensity.

less than D_o° (HI) (see also Appendix A, Chapter IV). However, the behavior of the Ba + HF reaction cannot be rationalized in this manner, as the most recent value[11] for D_o° (BaF) exceeds that of D_o° (HF) by ~5 kcal/mole. Studies of electron capture cross sections of HX [12] indicate that the vertical electron affinity of HI near the minimum in its well is close to zero. This decreases in the HX series until the electron attachment process is ~50 kcal/mole endoergic for HF. Since the barium halides are ionically bound,[10] this extra energy required to produce the negative ion probably has the effect of reducing the value of Q_o or increasing E* or both for this reaction, and would explain our failure to detect reaction.

E. Bond Dissociation Energies

Experimental determinations of bond dissociating energies of high temperature metallic halides are notoriously difficult. Thus, in his most recent compilation of bond energies of diatomic molecules, Gaydon[9] regards the experimental data on the CaI, SrI, and BaI bond energies as unreliable and refers to Rittner ionic model calculations by Krasnov and Karaseva[10] for the best estimates. Modern chemical kinetics studies of reaction dynamics may be expected to establish lower limits for a number of bond dissociation energies as these techniques are extended to embrace a wider variety of reactions; recent examples are given by lower limits for bond strengths of a number of alkaline earth halides and oxides provided by molecular beam electronic chemiluminescence experiments[13] and of the H-$SiCl_3$ band provided by an infrared chemiluminescence experiment.[14]

In the present experiment, a minimum of E* relative translational energy of approach is observed to permit reactions of Ca, Sr, and Ba with HI. At the temperature employed, the HI has negligible vibrational energy and RT_{HI} average rotational energy.[15] Thus, by energy conservation, the observation that reaction occurs imposes the following limit on the dissociation energy of the alkaline earth iodide, $D_o^\circ(MI)$, terms of the known[9] HI dissociation energy, $D_o^\circ(HI)$, the final product energy in translational recoil E' and internal excitation W':

$$D_o^\circ(MI) \geq D_o^\circ(HI) - E^* - RT_{HI} + E' + W' . \qquad (28)$$

Rigorous lower limits on the CaI, SrI, and BaI dissociation energies evaluated by means of Eq.(28) and assuming E' = W' = 0, are given in Table I. These limits are firmly established even if the value for E* is low due to broadening of the angular distribution by finite product recoil speeds. The larger value of E* activation energy is offset by the finite value of E' needed to broaden the distribution. The assumption that W' is zero may also be challenged by an argument presented in Reference 5. Generally, it states that in order to conserve angular momentum, all of the initial angular momentum in the collision must appear in the products as rotational excitation in view of the very small reduced mass of the separating products. This would raise the $D_o^\circ(MI)$ limits in Table I by 1-2 kcal/mole.

Although E* was not measured by Ba + HBr → BaBr + H, a similar treatment can be made because reaction was observed. The result is also included in Table I.

Table I also lists the ionic model D_o° estimates given by Krasnev and Karaseva.[10] These workers also recommend D_o° values for SrF and BaF which are only slightly less (5 kcal/mole) than recent reliable effusion cell measurements.[11a] On the other hand, recent effusion cell[11b] and molecular beam[13b] determinations of D_o° values of the possibly less ionic CaCl, SrCl, and BaCl molecules are very close to the lower limits of estimates of Krasnov and Karaseva. Thus, extrapolating this trend to the bromides and iodides, D_o° values of ~60, 65, and 70 kcal/mole for CaI, SrI, and BaI, respectively, might be estimated from Krasnov and Karaseva's calculated value. Similar values are predicted from a rough correlation of known MX bond strengths and equilibrium bond lengths shown in Appendix A of Chapter IV. In view of these lower values, the rigorous lower limits established in this work take on added significance.

REFERENCES

1. E. H. Taylor and S. Datz, J. Chem. Phys. 23, 1711 (1955).
2. S. Datz, D. R. Herschbach, and E. H. Taylor, J. Chem. Phys. 35, 1549 (1961).
3. a. A. E. Grosser, A. R. Blythe, and R. B. Bernstein, J. Chem. Phys. 42, 1268 (1965).
   b. K. T. Gillen, C. Riley, and R. B. Bernstein, J. Chem. Phys. 50, 4019 (1969).
4. D. Beck, E. F. Greene, and J. Ross, J. Chem. Phys. 37, 2895 (1962).
5. T. J. Odiorne and P. R. Brooks, J. Chem. Phys. 51, 4676 (1969).
6. M. Abramowitz and I. A. Stegun (eds.), Natl. Bur. Std. (US) Appl. Math. Ser. 55, 1020-1030 (1964).
7. ibid., pp. 255-265.
8. M. Ackerman, E. F. Greene, A. L. Moursund, and F. Ross, J. Chem. Phys. 41, 1183 (1964).
9. A. G. Gaydon, Dissociation Energies and Spectra of Diatomic Molecules (3rd ed.) (Chapman and Hall Ltd., London, 1968).
10. K. S. Krasnov and N. V. Karaseva, Optics and Spectros. 19, 14 (1965).
11. a. D. L. Hildebrand, J. Chem. Phys. 48, 3657 (1968).
    b. D. L. Hildebrand, J. Chem. Phys. 52, 5751 (1970).
12. D. C. Frost and C. A. McDowell, J. Chem. Phys. 29, 503 (1958).

13. a. Ch. Ottinger and R. N. Zare, Chem. Phys. Lett. 5, 243 (1970).

b. C. D. Jonah and R. N. Zare, Chem. Phys. Lett. 9, 65 (1971).

c. C. D. Jonah, R. N. Zare, and Ch. Ottinger, J. Chem. Phys. 56, 263 (1972).

14. N. Jonathan, C. M. Melliar-Smith, D. Timlin, and D. H. Slater, App. Optics 10, 1821 (1971).

15. Actually, the HI rotational energy might be less than RT_{HI} if the enhanced HI speed distribution reflected a transition to an isentropic nozzle flow. However, this is a minor effect which would make the lower limits on $D_o^\circ(MI)$ given in Table I be too low by less than 0.5 kcal/mole.

IV. REACTIONS OF ALKALINE EARTH ATOMS WITH MIXED HALOGENS

A. Introduction

Crossed beams studies have determined angular distributions of product scattering from K, Rb, and Cs,[1] Na,[2] and Li [3] + ICl and from Cs [4] and K [4,5] + BrCN. In general, the results reported for these reactions were quite similar to those found for the reactions of alkali atoms (A) with homonuclear halogen molecules (X_2). The dynamics of these latter reactions have been rationalized in terms of an electron transfer model which pictures the transfer of the valence electron of A to X_2 at a relatively large reactant separation; the reaction then proceeds to form the ionically bound alkali halide product by means of the breakup of the X_2^- intermediate in the force field provided by the A^+ ion. Three groups have reported classical trajectory calculations[6-8] using potential hypersurfaces with the long range reactant attraction which is suggested by this model. However, the manner in which the intermediate X_2^- decomposes remains uncertain because all of these calculations gave results consistent with the experimental findings despite quite different assumptions regarding the product interactions.

The study of mixed halogens should help clarify this uncertainty because the reactant sides of the potentials are likely to be quite similar, due to comparable electron affinities; but as Reference 1 points out, the "introduction of asymmetry in the mass distribution and

electronic structure thus provides an opportunity to look for effects which can be related to the dynamics of the breakup of the halogen molecule-ion". Unfortunately, however, the previous crossed beams studies[1-5] with mixed halogens (XY) have provided only limited additional insight into the dynamics of alkali atom reactions because these experiments employed a surface ionization detection technique which failed to distinguish between the AX and AY products. Kinematic analyses[1-3] of the measured laboratory (LAB) angular distributions indicated that ACl is the predominant product of the A + ClI reactions. A triple beam chemiluminescence study[9] provided further support for this conclusion for the K + ClI reaction, although this study suggested that some KI product was produced as well.

The use of an electron bombardment ionizer detector to distinguish the two products in these alkali reactions would be severely hampered by uncertainties in the fragmentation patterns of the alkali halides, which may depend strongly on the AX vibrational state.[10] The angular distributions thus measured would be highly ambiguous. As was mentioned in Chapter I, the fragmentation patterns in the alkaline earth monohalides are quite favorable.

This chapter reports product angular distributions of both product channels (MX and MY) for the reactions of Ba, Sr, Ca, and Mg + ICl and Ba + BrCN. Previous crossed beams studies of Ba + Cl_2 [11] and of Ba, Sr, Ca, and Mg + Cl_2 and Br_2 [12] indicated close similarities in the dynamics of reactions of alkali atoms and of the heavier alkaline earth atoms (notably Ba), despite the presence of the large chemical well in

the potential surface for the latter reactions. Thus, the study of the reactions of alkaline earth atoms with the mixed halogens might, in addition, throw some light on the analagous alkali reactions.

B. Experimental Procedure

The apparatus, described in Chapter II, was used without modification. The ICl was purchased from Eastman Organic Chemicals and the BrCN was purchased from Matheson Coleman and Bell; Both were used without further purification. The beam materials were introduced into the gas line from sample bulbs maintained at ~10 torr vapor pressure by an appropriate cold bath (ice-water for ICl and ice-brine for BrCN). The gas line reservoir pressure was regulated at 2-3 torr by a calibrated finger-stopcock combination. A careful mass scann of the ICl beam indicated that any impurities (e.g. Cl_2 or I_2) were less than 1% abundant.

As has been noted before, the probability speed distributions of both beams were non-thermal and were well-fit by the empirical expression

$$\rho_i(v_i) = N_i(v_i-a_i)^2 \exp[-(v_i-a_i)^2/\alpha_i^2]\, u(v_i-a_i) . \qquad (1)$$

Here, subscripts 1 and 2 denote the M and XY beams respectively; $u(t)$ is the unit step function ($u(t) = 0$ for $t \leq 0$; $u(t) = 1$ for $t > 0$); α_i and a_i are parameters which may depend on the beam source pressure; and $N_i = 4\pi^{-1/2}\alpha_i^{-3}$. Table I lists the beam operating

Table I. Experimental beam conditions[a]

Reaction	Alkaline earth atom beam				Halogen beam			
	source conditions		speed distribution[b,c]		source conditions		speed distribution[b,d]	
	temp.	pressure	α_1	α_2	temp.	pressure	α_1	α_2
Ba + ClI	1000	0.14	3.3	0.6	350	2.4	1.9	1.5
Ba + ICl	1010	0.15	3.3	0.6	340	2.8	1.9	1.5
Sr + ClI	980	0.6	3.8	1.3	340	3.0	1.9	1.5
Sr + ICl	980	0.6	3.8	1.3	340	2.7	1.9	1.5
Ca + ClI	1040	0.6	5.8	1.9	360	2.3	1.9	1.5
Ca + ICl	1060	0.7	5.9	1.9	360	2.3	1.9	1.5
Mg + ClI	860	0.8	6.8	2.2	350	3.0	1.9	1.5
Ba + NCBr	1080	0.6	3.2	1.1	350	2.7	2.3	1.9
Ba + BrCN	1120	1.0	3.3	1.1	350	2.6	2.3	1.9

[a] Temperatures are given in °K, pressure in torr, and speeds in 100 m/sec. Data are given for the M + XY → MX + Y reaction.

[b] Symbols refer to parameters of Eq.(1).

[c] Parameters for Ba are based on actual measurements; parameters for Sr, Ca, and Mg are from an extrapolation discussed in Chapter II.

[d] Parameters for ICl are based on actual measurements; parameters for BrCN are from an extrapolation discussed in the text.

Fig. IV-1. Shown are the LAB angular distribution for Ba + ClI → BaCl + I from 3 separate runs. The dotted curve gives the calculated (assuming an energy independent cross section) angular distribution of center of mass vectors, $\vec{C}$. The curves in the lower two panels are the $T(\theta)$ and $P(E')$ functions which generate the fits shown to the data. The legends correspond to those in Table III, and the long dash and dot-dash curves give the corresponding LAB fits using the solid $P(E')$ curve. Also shown are angular profiles of the beams and a diagram relating the sense of Θ, the LAB scattering angle.

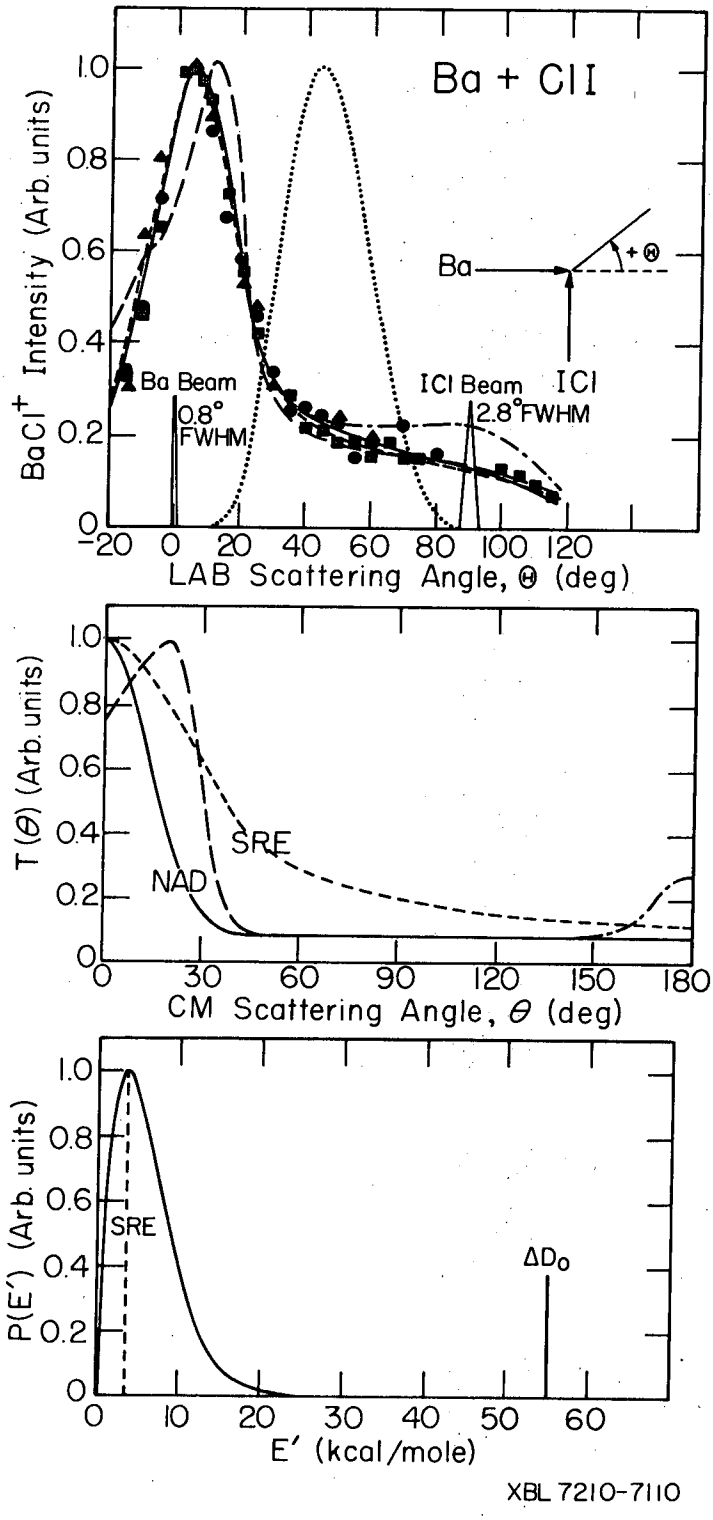
Ba + ClI
Ba
+Θ
ICl
Ba Beam
0.8°
FWHM
ICl Beam
2.8°FWHM
BaCl+ Intensity (Arb. units)
LAB Scattering Angle, Θ (deg)
T(Θ) (Arb. units)
SRE
NAD
CM Scattering Angle, Θ (deg)
P(E') (Arb. units)
SRE
ΔD0
E' (kcal/mole)
XBL 7210-7110

Fig. IV-1.

conditions and Fig. IV-1 shows the angular profiles of the beams. The parameters for the ICl velocity distributions are based on measurements reported in Chapter II. The BrCN parameters are estimated by multiplying the ICl parameters for the appropriate source pressure by $\sqrt{M_{ICl}/M_{BrCN}}$. All data analysis presented in this paper is arrived at by averaging over the actual beam speed distributions (Eq.(1) and Table I). Auxiliary calculations assuming thermal beam speed distributions indicated that the derived center-of-mass (CM) cross section results could be considerably in error if the true halogen beam speed distributions had not been used; on the other hand, recognition of the smaller deviations from thermal behavior of the alkaline earth beams had much less influence on the derived CM cross sections.

Figure IV-1 illustrates that the LAB scattering angle, Θ, is defined as 0° for the M beam direction and 90° for the XY beam direction. The detector may be rotated about the beam intersection volume, in the plane defined by the two intersecting beams, so as to scan a range of Θ from -15° to +115°. The detector angular resolution response function is similar in shape to the M beam angular profile shown in Fig. IV-1. No measurements of the product LAB speed were made; only product LAB angular distributions are reported here. All product angular distributions were measured with the mass filter set at the MX^+ or MY^+ peak. Careful mass scans for several of the scattering partners (Ba and Mg + ClI and Ba + BrCN) failed to disclose any MXY^+ scattered signal. Jonah and Zare[13] have reported the radiative recombination of Ba and Cl_2 to form $BaCl_2$ and here also the MX^+

signal could have arisen from MX or MXY as the parent molecule. Arguments presented later indicate that MX was the predominant, if not exclusive, precursor.

C. Data Analysis and Results

1. Analytical Considerations

The reaction cross section is a function of many variables. The variables most intimately related with the reaction dynamics are the angle θ, and speed u, with which the product recoils in the center of mass (CM) reference frame. It may also depend on the initial relative velocity, V. This differential cross section $\sigma(\theta,u,V)$ is measured at angle Θ, and velocity v in the laboratory (LAB) frame after it has been transformed from its moving (CM) frame of reference, by the following equation

$$F(\Theta,v) = V\sigma(\theta,u,V)\frac{v^2}{u^2} \qquad (2)$$

The sense of the lab angle, Θ, with respect to the beam directions is shown in Fig. IV-1 and Fig. IV-2 shows a CM $\leftrightarrow$ LAB transformation diagram for the Sr + ClI $\rightarrow$ SrCl + I reaction. In the CM coordinate system, θ is defined as 0° (forward scattering) if $\vec{u}$ lies along the initial relative velocity vector, $\vec{V}$, in the direction defined by the Sr beam.

Equation (2) is an expression for the flux of product at Θ and v. Therefore, in the present machine with a number density detector, one power of v must be factored out. In addition, in this apparatus, one must average over the beam speed distributions and integrate over the

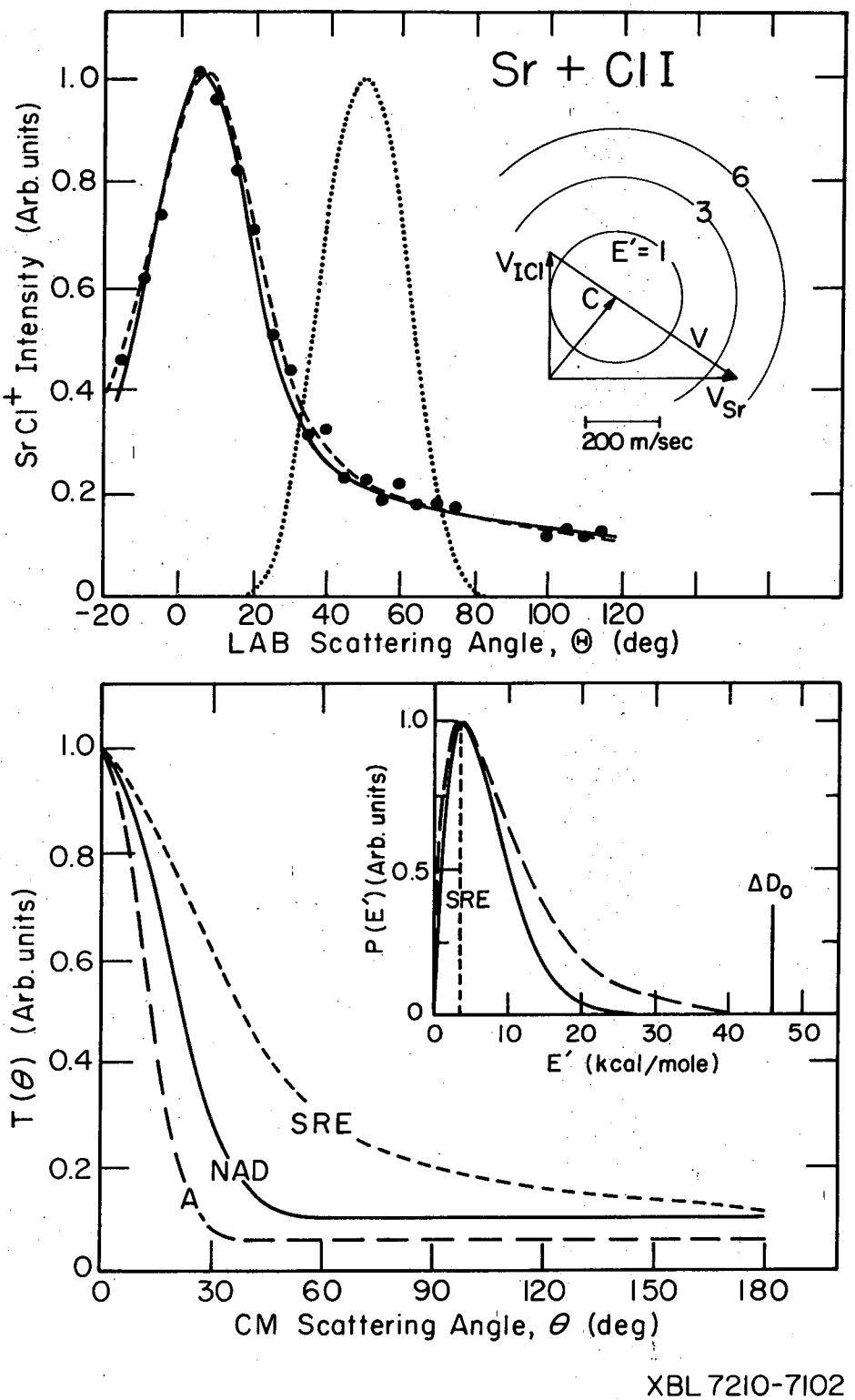

Fig. IV-2. LAB angular distribution data for Sr + ClI → SrCl + I and CM recoil functions. Also shown in a CM ↔ LAB transformation diagram. The circles indicate SrCl recoil speeds for some possible product recoil energies, E' (kcal/mole).

unmeasured LAB speed of the product, v, so that the CM cross section is related to the measured LAB intensity by the following:

$$I_{LAB}(\Theta) = \int_0^{v^*}\int_0^{\infty}\int_0^{\infty} V\sigma(\theta,u)(v/u^2)\rho_1(v_1)\rho_2(v_2)dv_1dv_2dv \quad . \quad (3)$$

The analysis of the data here generally consisted of choosing a form of σ, performing the integrations in Eq.(3) on a computer, and comparing the calculated LAB angular distribution with the measured data. This procedure was repeated until, by trial and error, a form of σ was obtained which provided a good fit to the data.

The integration over v shown in Eq.(3) is limited to a finite range (0 to v*) determined by the reaction energetics. For the M + XY → MX + Y reaction, where the MX product is detected, the energy with which the MX and Y products recoil apart, E', and the internal excitations of MX and Y, W', are related to the initial XY internal excitation, W, and the reactant relative collision energy, $E = (m_M m_{XY}/2m_{MXY})V^2$, by

$$E' + W' = E + W + \Delta D_o, \quad (4)$$

where $$\Delta D_o = D_o(MX) - D_o(XY), \quad (5)$$

$$E' = (m_{MXY}m_{MX}/2m_Y)u^2 \ , \quad (6)$$

and the m's denote the masses of the particles. Table II lists values of E, W, and ΔD_o; v* was calculated for each reaction by setting E = W = W' = 0. Although D_o(Cl-I),[14] D_o(Br-CN),[14] and D_o(M-Cl)[15] are well

Table II. M + XY → MX + Y reaction energetics[a]

Reaction	relative collision energy, E [b]	reactant internal excitation, W [c]	reaction exoergicity ΔD_o
Ba + ClI	2.1	1.0	55 ± 3
Ba + ICl	2.1	1.0	35 ± 15
Sr + ClI	2.7	1.0	46 ± 3
Sr + ICl	2.7	1.0	30 ± 15
Ca + ClI	2.9	1.0	45 ± 3
Ca + ICl	2.9	1.0	25 ± 15
Mg + ClI	2.5	1.0	25 ± 3
Mg + ICl	-	-	5 ± 10
Ba + NCBr	2.6	1.5	30 [d]
Ba + BrCN	2.6	1.5	10 ± 15

[a] All energies are given in kcal/mole.

[b] Calculated for the most probable (number density distributions) beam speeds.

[c] The average thermal rotational and vibration energy in XY which is given here would be too large if the internal degrees of freedom relax somewhat in the beam expansion process.

[d] This is an estimate (see Appendix A).

known, there are no reliable experimental determinations of the bond energies of MBr, MI, or MCN. The values used here for MI and MBr are from an ionic bonding model calculation.[16] The value used for BaCN is an estimate which is based on an empirical correlation (see Appendix A). The structure of this product might be BaCN or BaNC; reported Hartree-Fock calculations[17] indicate that LiNC is marginally more stable than LiCN.

In analyzing the data by means of Eq.(3), σ is assumed to be independent of relative velocity, V. Although recent data on the reactions of higher energy (~5 kcal) K with Br_2 and BrCN [5] indicate a smaller cross section than the earlier published values, a recent, very careful study of the $K + I_2$ reaction[18] at relative energies from 1.9 to 3.6 kcal/mole showed only a very slight energy dependence of the total reactive cross section. A second assumption made is that the cross section is separable in θ and u, i.e.

$$\sigma(u,\theta) = T(\theta)U(u) \qquad (7)$$

This assumption is also supported by Reference 18, in which only a weak coupling of θ and u was noted. Furthermore, because of the absence of product velocity analysis, a family of $T(\theta)$ and $U(u)$ functions will fit the data (and probably an infinite number of coupled functions as well). Therefore, the laboratory angular distribution is best suited to provide qualitative information about a reaction and any introduction of coupled CM cross sections would be a bit pretentious.

In some of the data analyses, it has further proven convenient to express $T(\theta)$ and $U(u)$ as:[19]

$$T(\theta) = (1-C_1)\exp[-\ell n2(\theta/H_1)^2] + C_1, \text{ and} \qquad (8a)$$

$$U(u) = (u/u_1)^{n_1}\exp[(n_1/m_1)(1-(u/u_1)^{m_1})];\ u \leq u_1\ , \qquad (8b)$$

$$U(u) = (u/u_1)^{n_2}\exp[(n_2/m_2)(1-(u/u_1)^{m_2})];\ u \geq u_1\ ,$$

where all subscripted variables serve as adjustable parameters.

In order to provide insight into the range of CM cross sections which are compatible with the experimental data, at least two data analyses are presented for each reaction. One of these, termed the "Single Recoil Energy" (SRE) result, assumes that the products separate with a single, fixed product recoil energy (i.e., $U(u)$ is approximated as a delta function). Since this procedure removes the flexibility in the $U(u)$ function of Eq.(8b), the $T(\theta)$ function is not restricted to the form of Eq.(8a) in seeking fits to the data. Because the full breadth of the measured LAB angular distribution must be accounted for by the $T(\theta)$ function, the SRE result should provide an upper limit on the overall breadth of the peak in the true CM angular distribution. The opposite data analysis extreme presented, termed the "Narrow Angular Distribution" (NAD) result, seeks the $T(\theta)$ function, given by Eq.(8a), with the narrowest breadth about its peak which can be fit to the data; this extreme should provide an upper limit for the dispersion in the recoil speed distribution. In general, data which could be fit by the SRE analysis could also be fit by a family of curves intermediate between the SRE and NAD extremes.

2. $\underline{M + ClI \rightarrow MCl + I}$

The MCl^+ angular distributions are given in Figures IV 1-4. All four show that the LAB MCl^+ signals all peak at considerably smaller Θ values than do the calculated angular distributions (assuming an energy-independent collision cross section) of the LAB velocity of the center-of-mass of the collision partners, $\vec{C}$. Furthermore, the data points fall off smoothly with angle through the angular regions of the peaks of the $\vec{C}$ distributions. These comparisons show that the MCl^+ measured signals must have arisen from ionization of an MCl product which had scattered predominantly into the forward CM hemisphere. Since any MXY formed would be confined to the plane of the detector, the apparatus is much more sensitive to it. One can calculate the fraction of the total BaCl scattering the detector can see at a given LAB angle, assuming a cross section given by the NAD fit, and also how much of the kinematically restrained MXY it could see (based on detector angular resolution). These numbers indicate that if the cross section to form MXY were >1% as large as the cross section to form BaCl, they would produce equal intensities at their peaks in the lab.

Figures IV-1 - IV-4 also show the fits to the measured data which were generated by the $T(\theta)$ and $U(u)$ curves shown on the bottom panels. Table III includes the parameters for the fits shown. $P(E')$ was calculated from $U(u)$ by means of Eq.(6) as $P(E')dE' = U(u)du$.

Calculations for a variety of other CM cross sections have also indicated the following properties of all of the MCl angular

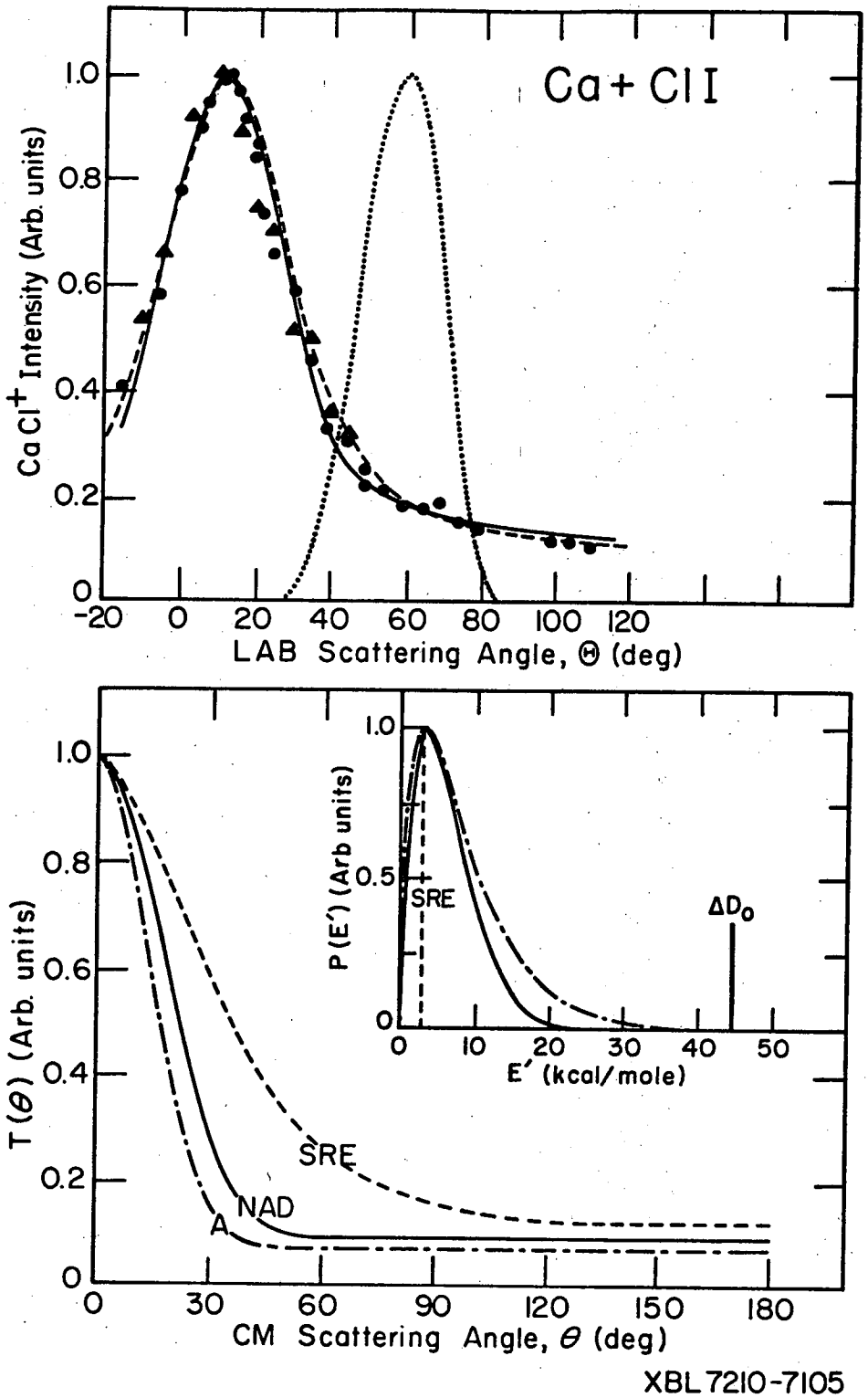

Fig. IV-3. LAB scattering data for Ca + ClI → CaCl + I. The fit obtained from the A recoil distributions was nearly as good as that for NAD.

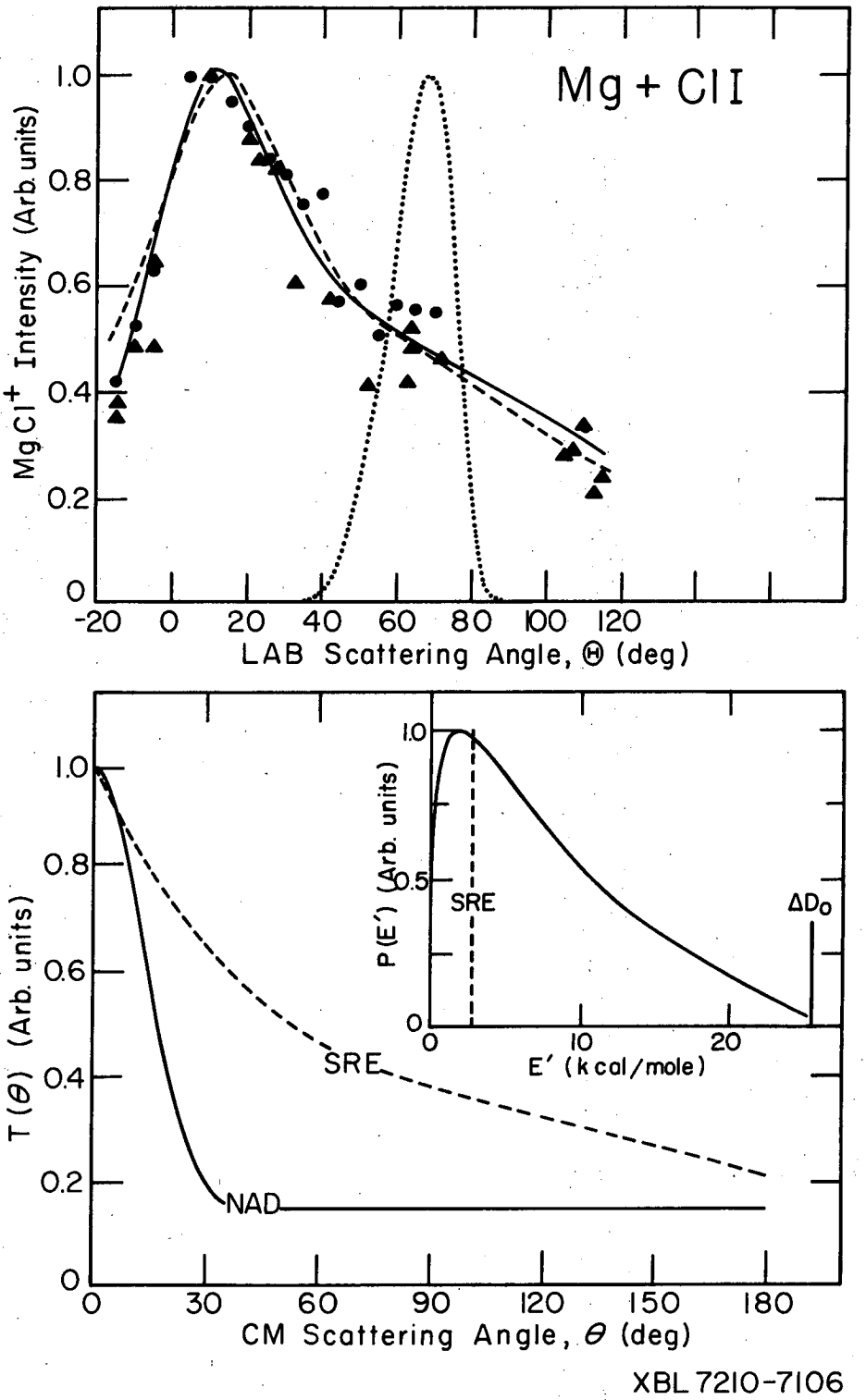

Fig. IV-4. LAB scattering data for Mg + ClI → MgCl + I and CM recoil distributions.

Table III. M + XY → MX + Y derived CM reaction cross sections [a]

reaction	legend	angular distribution [b]			speed distribution [c]		recoil energy [d]	
		H_1	C_1	Q_F	u_1	n_1,m_1,n_2,m_2	$\bar{E}'$	$\langle E' \rangle$
Ba + ClI	SRE	-	-	0.72	-	-	3.3	3.3
	NAD	16	0.08	0.62	3.2	3,2,2,3	3.3	4.7
	A*	10	0.04	0.60	3.2	2,2,2,2	2.5	5.0
Sr + ClI	SRE	-	-	0.70	-	-	3.3	3.3
	NAD	20	0.10	0.67	4.5	3,2,2,3	3.9	5.4
	A	13	0.06	0.61	4.8	2,2,2,2	3.3	6.6
Ca + ClI	SRE	-	-	0.72	-	-	2.8	2.8
	NAD	20	0.09	0.65	6.0	3,2,2,3	3.5	4.9
	A	16	0.07	0.63	6.3	2,2,2,2	2.9	5.7
Mg + ClI	SRE	-	-	0.61	-	-	2.8	2.8
	NAD	15	0.15	0.56	8.0	2,1,2,2	1.7	5.3
	(A)	16	0.07	0.63	6.3	2,2,2,2	2.9	5.7
Ba + ICl	SRE	-	-	0.58	-	-	9.0	9.0
	A	135	0.00	0.60	2.2	10,2,2,10	11.7	11.5
	B	-	-	0.60	2.5	3,2,2,3	11.1	13.8
	C	15	0.17	0.55	2.7	2,1,2,2	4.9	11.6
Sr + ICl	SRE	-	-	0.62	-	-	8.0	8.0
	A	120	0.00	0.63	2.5	10,2,2,10	10.1	10.9

Table III continued

	B	-	-	0.60	3.0	3,2,2,3	10.8	11.1
	(C)	15	0.17	0.55	3.5	2,1,2,2	5.5	11.1
Ca + ICl	SRE	-	-	0.61	-	-	8.0	8.0
	A	120	0.00	0.63	3.1	10,2,2,10	9.9	9.7
	B	-	-	0.60	4.0	3,2,2,3	12.2	10.4
	(C)	15	0.17	0.55	4.0	2,1,2,2	4.6	11.5
Ba + NCBr	SRE	-	-	0.67	-	-	2.8	2.8
	(A)	40	0.25	0.65	3.0	3,2,2,3	2.7	5.0
	NAD	10	0.07	0.56	3.2	2,1,2,2	1.4	5.1
Ba + BrCN	SRE	-	-	0.52	-	-	4.0	4.0
	A	42	0.50	0.57	2.0	2,1,2,2	2.4	4.4
	NAD	15	0.30	0.53	2.0	2,1,2,2	2.4	4.4

* Fits with legend in parentheses are not shown in the figures but provided comparable fits to the data.

[a] Energies are given in kcal/mole and speeds in 100 m/sec.

[b] H_1 and C_1 are parameters of Eq.(8a) and Q_F is the fraction scattered forward (Eq.(9)). If no entries are given for H_1 and C_1, $T(\theta)$ was not restricted to the form of Eq.(8a).

[c] These are the parameters of Eq.(8b).

[d] $dP(E')/dE'\big|_{E'=\bar{E}'} = 0$; $\langle E' \rangle = \int_0^{\Delta D_o} E'P(E')dE'$. All fits refer to ΔD_o values given in Table II except the B and C fits for Ca and Sr + ICl. These provided fits only if ΔD_o was assumed to be the upper limit shown in Table II.

distributions: (1) any $T(\theta)$ symmetric about 90° is incompatible with the data; (2) $T(\theta)$ must peak with $\theta \lesssim 20°$; (3) $T(\theta)$ might actually have a secondary peak at 180°, but it cannot be more than ~20-25% of the forward peak; and (4) $T(\theta)$ cannot be broader than the SRE fit, nor much narrower than the NAD fit. Properties (2) and (3) are illustrated in Fig. IV-1. Furthermore, the true CM cross sections should be much closer to the NAD results than to the SRE results because of the unrealistic treatment of the recoil energy distribution in the SRE procedure and because the NAD results are qualitatively similar in shape to product velocity analysis results for $K + Br_2$ [20] and $K + I_2$.[18]

Table III also includes values for the fraction of the products, Q_F, which is scattered into the forward CM hemisphere:

$$Q_F = \int_0^{\pi/2} T(\theta) \sin\theta \, d\theta \Big/ \int_0^{\pi} T(\theta) \sin\theta \, d\theta \, . \qquad (9)$$

These indicate a tendency for Mg to produce less MCl forward scattering than do the other alkaline earth atoms. The characteristic E' values given in Table III, together with the ΔD_o entries of Table II, also clearly indicate that most of the reaction exothermicities appear as internal excitations of the products.

3. <u>M + ICl → MI + Cl</u>

Figures IV-5 - IV-7 show that the measured BaI^+, SrI^+, and CaI^+ signals peak at smaller LAB angles than do the calculated distributions of $\vec{C}$, again indicating that the MI products are scattered predominantly into the forward CM hemisphere. Furthermore, the smooth decrease with

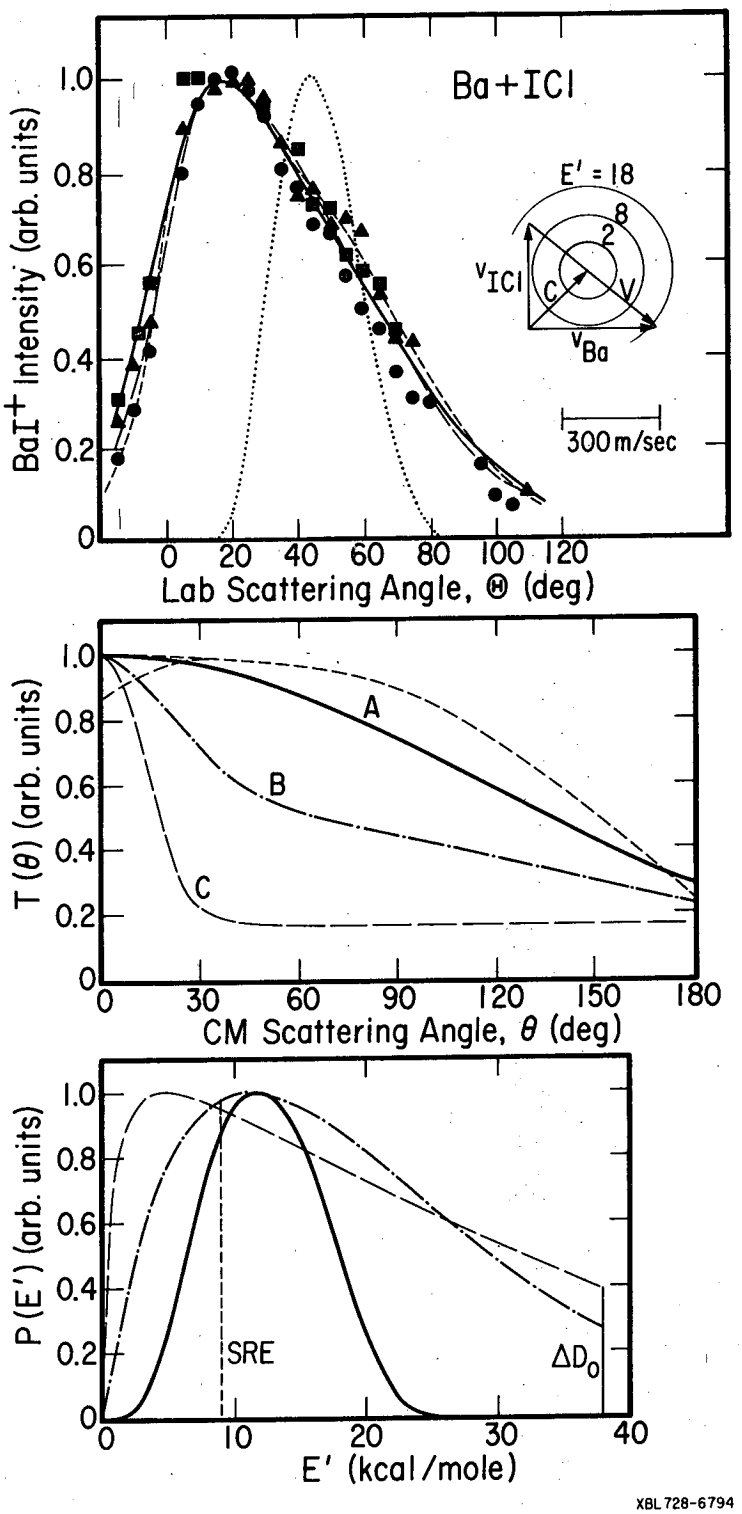

Fig. IV-5. LAB scattering data for Ba + ICl → BaI + Cl, CM recoil distributions, and CM-LAB transformation diagram. The B fit to the data is equally good.

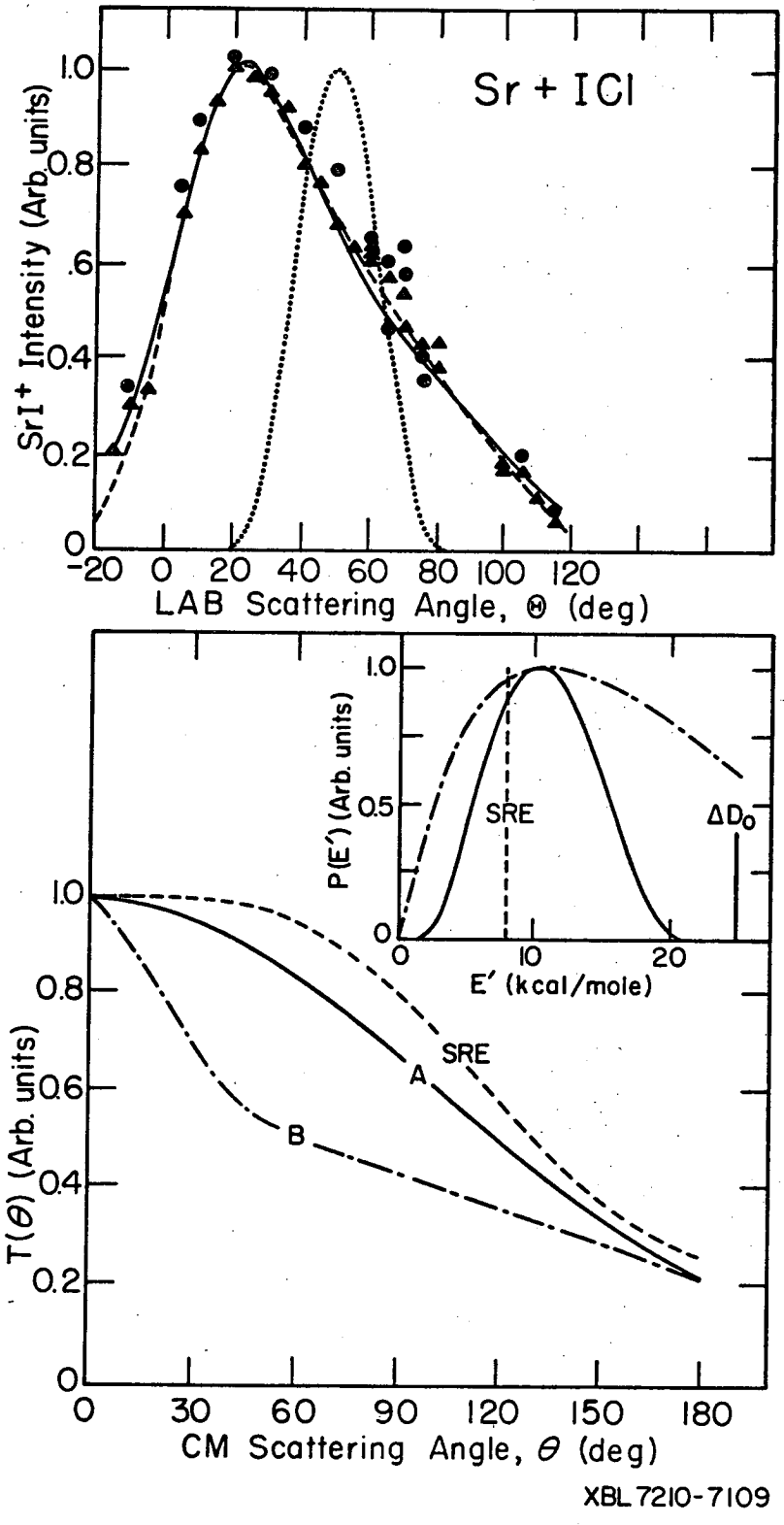

Fig. IV-6. LAB scattering data for Sr + ICl → SrI + Cl and CM recoil functions. Fit B and one equivalent to C in Fig. IV-5 also fit the data only if ΔD_o was raised to the maximum indicated in Table II.

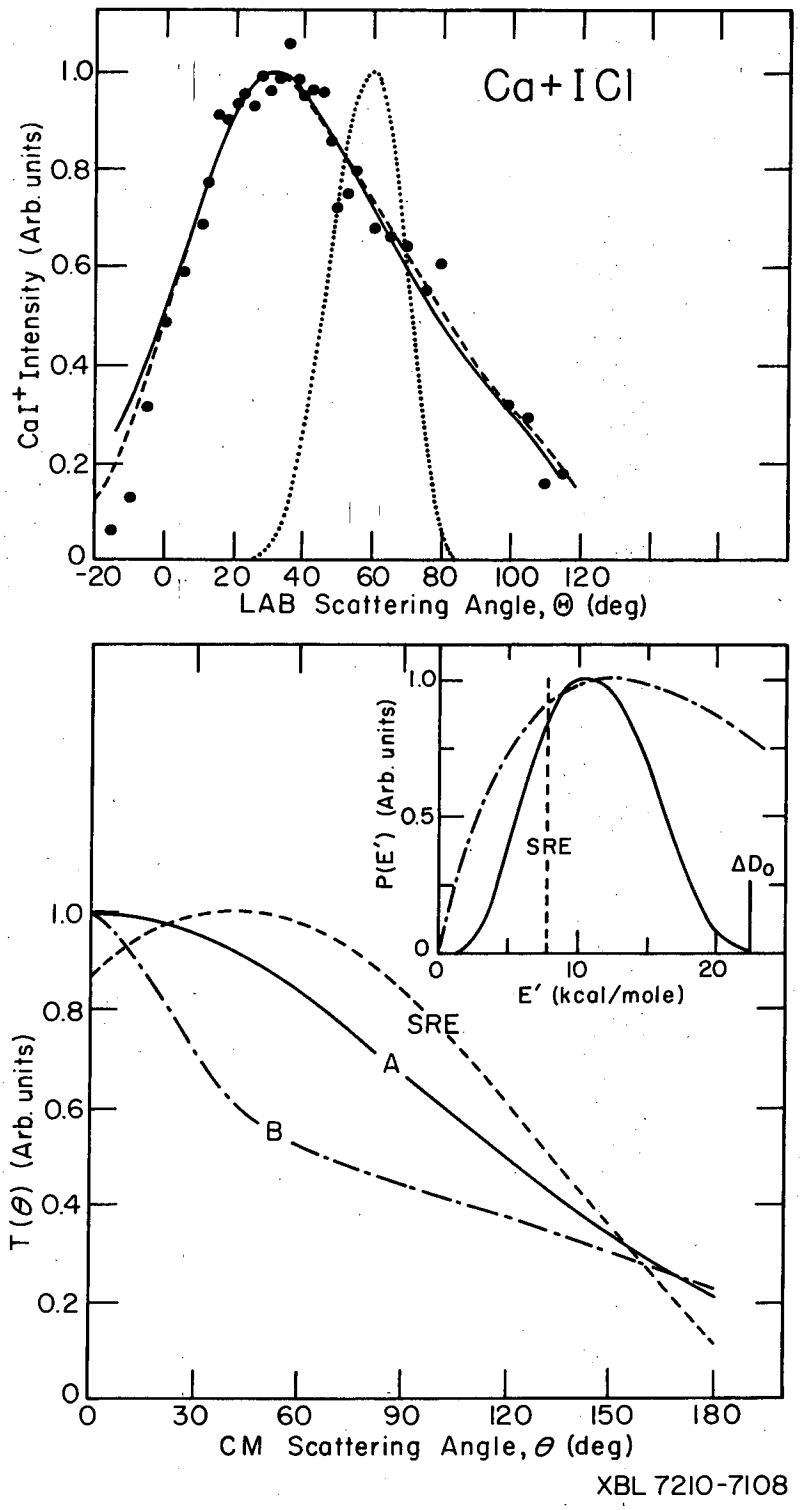

Fig. IV-7. LAB scattering data for Ca + ICl → CaI + Cl and CM recoil functions. The B fit and one equivalent to C in Fig. IV-5 will fit the data only if ΔD_o is raised to the maximum in Table II.

angle through the angular regions of the peaks in the $\vec{C}$ distributions which are apparent in the MCl^+ and MI^+ distributions in Figs. IV-1-IV-7 clearly indicate that little (if any) of the measured product signal arises from ionization of an MICl complex which would necessary recoil in the LAB along $\vec{C}$.

The LAB $\leftrightarrow$ CM transformation diagram for the BA + ICl $\rightarrow$ BaI + Cl reaction which is included in Fig. IV-5 illustrates that the observation of appreciable product intensity at small and even negative LAB angles, as shown in Figs. IV-5-IV-7, requires an appreciable product recoil energy for a significant fraction of the reactions. Furthermore, this transformation diagram, as well as Eq.(5), illustrates that the large m_{MI}/m_{Cl} product mass ratio restricts the MI product CM recoil speed to relatively small values even for rather large values of E'. Owing to the rather wide angular distribution of $\vec{C}$, this in turn makes the measured MI LAB angular distribution much less sensitive than the MCl LAB distribution to the form of the CM cross section.

This insensitivity is reflected in the wide range of CM fits to the data which are presented in Figs. IV-5-IV-7 and Table III. Although the NAD (denoted "C" in Table III) cross sections do provide fits to the measured M + ICl data, they are unlikely to reflect the true shapes of the CM cross sections for two reasons: (1) the NAD fits to the Sr and Ca + ICl reactions were obtained only by assuming the very upper extremes for the ΔD_o values given in Table II; and (2) a very specialized and unrealistic reaction mechanism would likely be required to account for a very sharply forward directed product angular distribution while,

at the same time, providing such a large dispersion in the product recoil energy distribution. Since the SRE fit makes a very restrictive assumption regarding the form of P(E'), the true CM cross sections are likely to fall somewhere within the range of the A and B fits of Figs. IV-3 and IV-4 and Table III. Here again, calculations for a variety of other CM cross sections also indicate that (1) $T(\theta)$ cannot be symmetric about 90°; and (2) $T(\theta)$ favors scattering into the forward CM hemisphere, as illustrated by the Q_F entries in Table III.

Because the detector response may vary each time the apparatus is exposed to atmospheric pressure, it is not possible to extract absolute total reaction cross sections, Q_T, nor even relative values for reactions of different alkaline earth atoms, although a general trend of decreasing LAB product intensity was noted on going from reaction of Ba to that of Mg. For a fixed alkaline earth atom, data on the MI^+ and MCl^+ angular distributions were collected during the same apparatus pumpdown. Thus, the absolute measured MI^+ and MCl^+ signals may be used to calculate $Q_T(MCl)/Q_T(MI)$ by simply correcting for the ratio, β, of MCl and MI detection efficiences and integrating the CM cross sections over recoil speed and solid angle. Although β is rather uncertain, we may estimate it to be unity by the following argument. There are three effects to take into account. The first is the ionization cross section, which generally scales with the polarizabilities of the neutral molecules.[21] This has been found to hold for the magnesium dihalides.[22] If one makes the simple-minded assumption that the polarizabilities of MX are simply the sum of those for M^+ and X^- (taken from Reference 23), MI is favored

over MCl by a factor of ~1.4 (Ca) to 1.3 (Ba). Similarities between the electronic term values of M and MX[24] indicate that the non-bonding electron on M contributes the lion's share to the polarizability, in which case the ratios should be closer to unity. The transmission of the quadrupole decreases with mass in a manner that should cancel any effect of the ionization cross section. Finally, the secondary electron ejection efficiency from CuBe dynode surfaces for atomic ions is generally considered to be proportional to ion velocity[25] and therefore to the inverse of the square root of the mass at a given ion energy. However, electron multiplier efficiencies for various magnesium halide ions[22] showed quite a bit of scatter, but no general correlation with mass number was evident. Thus, the value of β obtained from these three considerations is somewhat uncertain, but is likely to be close to unity. Assuming $\beta = 1$, the different combinations of derived CM cross sections given in Table III provide $Q_T(MCl)/Q_T(MI)$ ratio ranges of 1.3-2.3 for Ba and Sr and 1.5 to 3.2 for Ca. If only the more likely CM cross sections are used (i.e., the NAD MCl results and the A and B MI results), $Q_T(MCl)/Q_T(MI)$ becomes ~1.8 for Ba and Sr and ~2.1 for Ca. A very weak MgI^+ signal from Mg + ICl was also detected; although it proved to be too noisy to permit measurement of an MgI angular distribution, its magnitude suggested that $Q_T(MgCl)/Q_T(MgI) > \sim 5$. The uncertain thermochemistry of these reactions prevents a comparison of these ratios with a statistical theory[26] calculation. However, it is pertinent to note that Reference 1 gives statistical theory calculations of this ratio at 1.8 for K + ClI and 1.2-1.3 for Cs + ClI. It

must be emphasized that the ratios quoted here are quite uncertain, and that more reliable values will come when velocity analysis data on the products become available.

4. The Ba + BrCN → BaNC and BaBr Reactions

Figures IV-8 and IV-9 show the measured LAB $BaCN^+$ and $BaBr^+$ signals scattered from Ba + BrCN. Although the $BaBr^+$ signal is not sufficiently distinct from the calculated $\vec{C}$ distribution to preclude the chance that it arose (at least partly) from ionization of BaBrCN, the data were analyzed assuming BaCN and BaBr products. The BaBr product suffers from the same product mass ratio problem which was encountered with MI. Figures IV-8 and IV-9 and Table III indicate that a wide range of CM cross sections will fit the data. This is true to a lesser extent with BaCN as well because this data was collected near the end of our studies of alkaline earth atom chemistry; consequently, the detector was dirty, signal-to-noise had deteriorated, and unforeseen factors brought the experiment to a premature end before the wide-angle scattering had been measured. Nevertheless, the data do indicate that BaCN is more sharply scattered forward than is BaBr. The integrated total cross section ratio, $Q_T(BaNC)/Q_T(BaBr)$, is calculated to be ~7-20.

D. Discussion

Although there is considerable uncertainty in the derived CM cross sections, the data clearly indicate two qualitative differences between the M + ICl → MI + Cl and M + ClI → MCl + I reactions. First, the

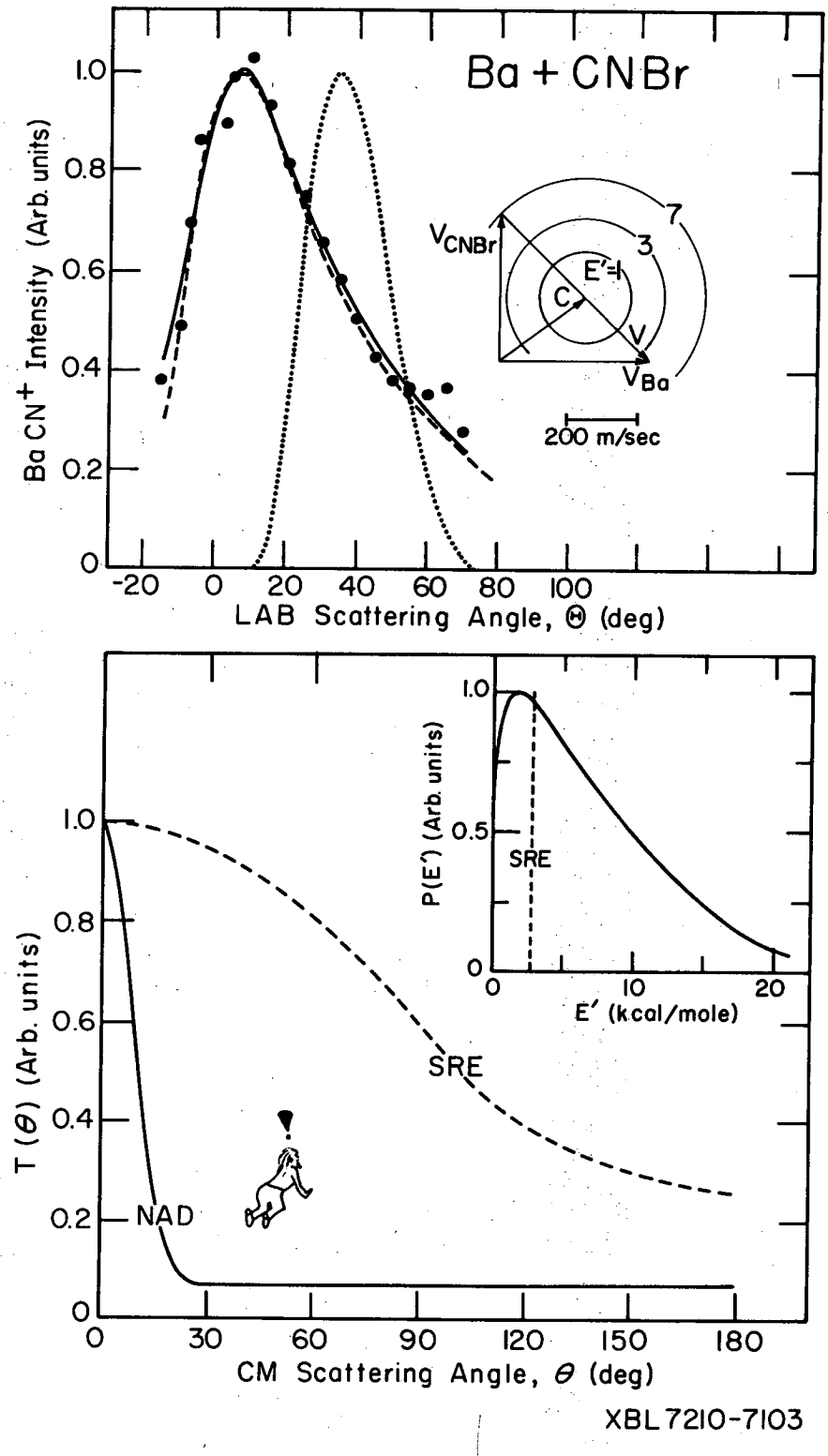

Fig. IV-8. LAB scattering data for the reaction Ba + NCBr → BaNC + Br and accompanying CM recoil functions.

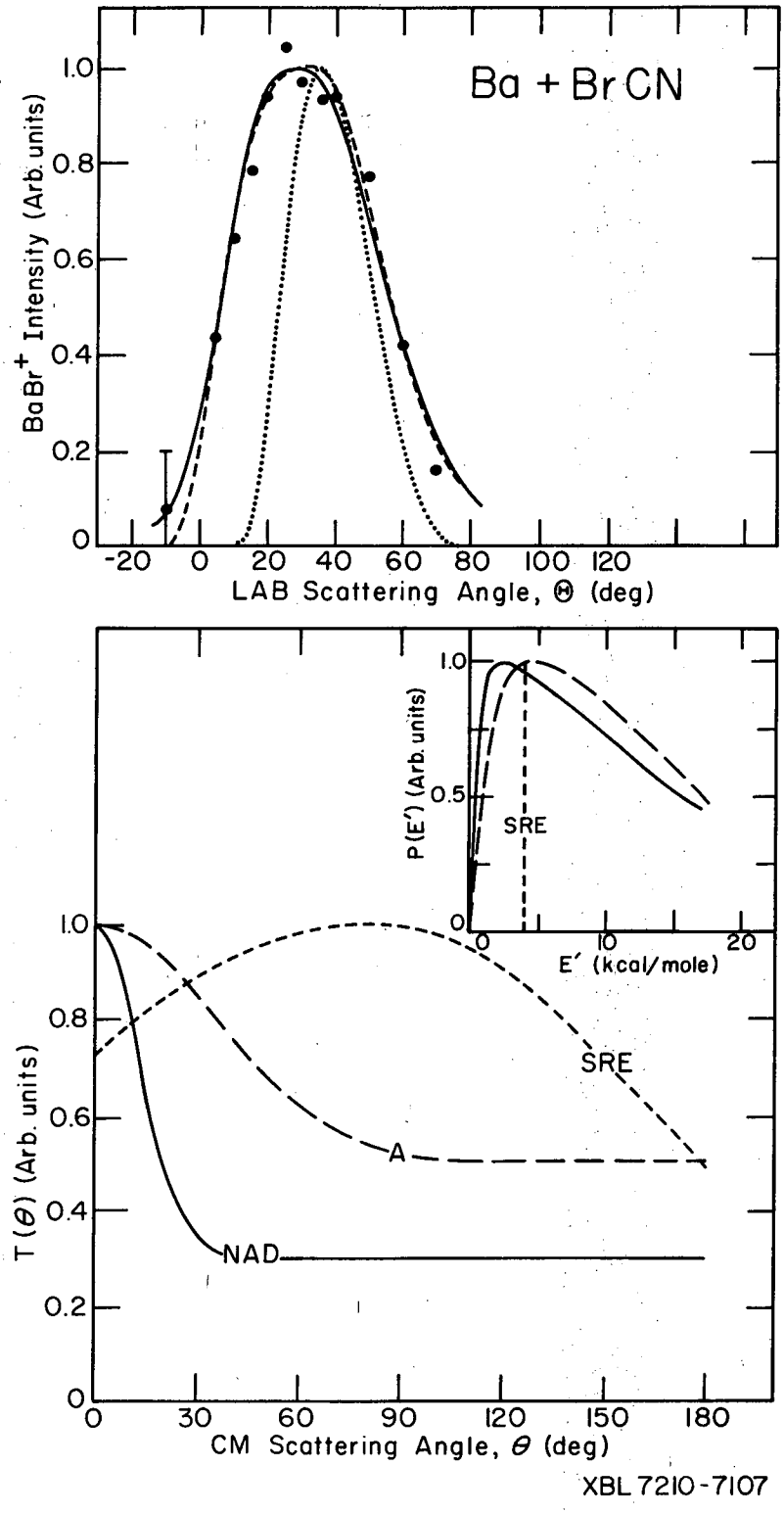

Fig. IV-9. LAB scattering data for Ba + BrCN → BaBr + CN and CM recoil functions.

entries in Table III indicate that the MI and Cl products recoil with appreciably higher average energy than do the MCl and I products; since ΔD_o is less for the M + ICl reaction, this corresponds to an even greater disparity in the fraction of the reaction exothermicity which appears as product recoil. These E' entries also indicate that the product recoil energy is relatively insensitive to the identity of the attaching alkaline earth atom. The second difference which is apparent between these reactions is that the MI product is scattered with a much broader CM cross section than is the MCl product. Although the data analyses do not unequivocally establish whether this added breadth appears in the recoil angle or energy distribution, the "most likely" analyses suggest that both distributions are broadened for the MI product. Property (2) might be a consequence, at least in part, of property (1), as the enhanced product recoil energy might be expected to broaden the forward peaked product angular distribution.

The features of the scattering of the MCl product which are observed here are similar to those found in the reactions of Cl_2 with alkaline earth[11,12] and alkali[27] atoms and are understable in terms of the simple one electron transfer model of alkali atom reactions. Details of this model of the A + ICl reactions are given in Reference 1. These authors point out that the lowest unfilled orbital on ICl which accepts the alkali valence electron is likely to be located predominantly on the I atom for the Cl-I internuclear separations at which the $ICl \rightarrow ICl^-$ vertical jump takes place. However, in free space, this ground state of ICl^- correlates asymptotically with $I + Cl^-$; of course,

for certain configurations the presence of the A^+ could change this asymptotic correlation to $Cl + I^-$. Nevertheless, Kwei and Herschbach[1] argue that this effect will favor formation of the MCl product, at least for large impact parameter collision where pre-migration of the charge in ICl^- is likely to be favored; they estimate, on the basis of a kinematic analysis of their measured AX angular distributions, that formation of ACl occurs 3-4 times as often as does that of AI for the K, Rb, and Cs + ICl reactions. Further evidence for the asymmetry of the ICl electronic structure is also provided (for a vastly different dynamical range) by crossed beams studies of the reactions of D atoms with ICl.[28] Thus, the simple one electron transfer model would provide an explanation of the CM product angular distributions which are observed here because it suggests that MCl rather than MI is likely to be formed in the large reactant impact parameter collisions which should favor forward scattering. The MI (and presumably some MCl) would be formed in smaller reactant impact parameter collisions which would tend to produce a broader product angular distribution.

However, the relatively large MI + Cl product recoil energies which are observed here suggest that the $M + ICl \rightarrow MI + Cl$ reaction dynamics are not adequately described by this one electron transfer model. The observed differences in the MCl and MI product recoil energies would probably be consistent with the one electron transfer model if the repulsion in ICl^- were much larger and were released much more rapidly than has been assumed in the trajectory calculations[6-8] on the $A + X_2 \rightarrow AX + X$ reactions. However, such a potential surface

would not be expected in this model. Moreover, trajectory calculations reported in References 7 and 8b for potential surfaces with appreciable product repulsion indicate that a potential surface of this type would also undoubtedly fail to explain the sharp alkali halide scattering which is observed in the $A + X_2$ reactions. An alternate explanation of the present results in terms of the one electron transfer model would picture formation of MI via an excited intermediate state if ICl^- which might be more repulsive and which would correlate,[1] asymptotically in free space, with $Cl + I^-$. However, this model seems very unlikely because the observed[1-3] strong attenuation of the wide-angle elastic scattering of alkali atoms from ICl suggests that the incoming alkali atom very seldom fails to transfer its electron to form the ground electronic configuration of ICl^-. While it is true that the weak Glory undulations in the energy dependence of the Li + ICl total collision cross section[29] suggest that this transfer is not 100% efficient, it seems unlikely to be sufficiently inhibited to account for the 20-40% MI formation which is observed here.

The MI scattering which is observed here suggests that the dynamics of these reactions might differ from that of the alkali atoms. This is certainly a possibility as the stability of the alkaline earth dihalides implies a deep chemical well in the potential hypersurface which is absent in that for the alkali atom reactions. Since the bonding in the alkaline earth dihalides is probably largely ionic, reactive trajectories which sample this well might be said to undergo a "two electron transfer" mechanism, corresponding to the reaction sequence: $M + XY \rightarrow M^+ \ldots$

$XY^- \rightarrow X^- \ldots M^{+2} \ldots Y^- \rightarrow M^+X^- + Y$. Previous studies[11,12] which noted the similarities of the reactions of M and A with Cl_2 and Br_2 indicated that this deep well in the potential surface did not dominate the dynamics of the reactions of the alkaline earth atoms; however, these studies would probably have been insensitive to the influence of the well in as many as 20-30% of the reaction trajectories. Moreover, the electronic asymmetry of ICl removes the symmetry restriction on broadside attack along the C_2 axis which exist for reaction with the homonuclear halogen molecules. Thus, an attractive explanation for all of the data presented here would picture many of the reactive trajectories proceeding via an alkali-like one electron transfer to form (predominantly) MCl (or BaNC). However, a substantial fraction of the trajectories would follow the two electron transfer mechanism. It is quite conceivable that a $Cl^-M^{+2}I^-$ complex, which would be very highly internally excited, might dissociate into MI and Cl with a high recoil energy.

A crude RRK estimate of the dissociational lifetime for such a complex indicates that this would be shorter than the rotational period, thus being consistent with the observed asymmetry of the product angular distribution. This might happen via a direct mechanism which could even favor formation of MI over MCl because of the greater mobility of the Cl atom. Alternatively, such a complex might tend to distribute the reaction energy statistically, which would again lead to relatively high E' values; in this case, however, decomposition into both product channels would be expected. Indeed, this is consistent with the data

as well because the detector is most sensitive to products scattered along $\theta = 0°$ (or 180°) with small E' values. This is evidenced in Fig. IV-10. The solid curve is the NAD fit to the BaCl data. If one calculates a LAB distribution with a BaCl CM cross section $\sigma(\theta,E')$ identical to the A fit for BaI and scaled such that both BaCl total cross sections are equal, the dashed curve results. Thus, the contribution of such a mechanism would appear in the LAB as only a small (i.e. ~10-30%) perturbation on the "one electron transfer MCl component" which is given in Fig. IV-2 and Table III. These possibilities point out the need for product velocity analysis measurements on the reaction studied here as well as further trajectory calculations on potential surfaces which not only include the deep chemical well present in these reactions but also which simulate the asymmetries introduced by the mixed halogens.

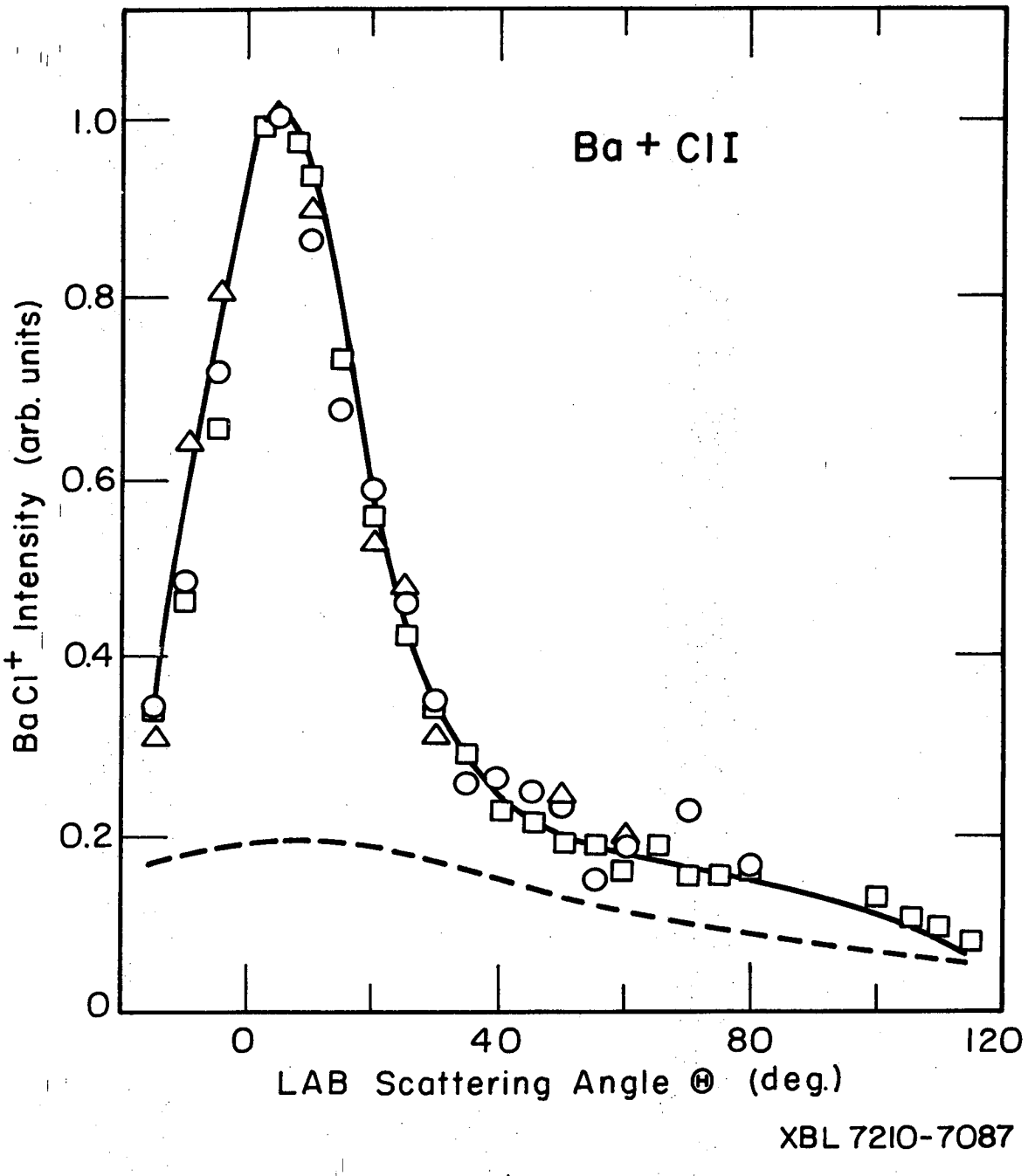

Fig. IV-10. The data points are $BaCl^+$ from Ba + ClI again. The solid curve is calculated from the NAD cross section fit to BaCl in Table III and Fig. IV-1. The dashed curve is calculated from the same $T(\theta)$ $P(E')$ given in the A fit for BaI and scaled to have the same absolute total cross section.

APPENDIX A

Reliable values for the dissociation energies of alkaline earth monochlorides and fluorides have only recently been established.[15,23] The bond strengths of the bromides and iodides are quite uncertain[16] and an estimate of the bond strength of BaCN is unavailable in the literature.

An empirical correlation[30] between equilibrium internuclear separation and the energy required to dissociate an ionically bound alkali halide (AX) into ions A^+ and X^- has proven very useful in the estimation of unknown bonds in alkali compounds. The available data on alkaline earth monohalides were examined for any correlation with the alkali halides, or at least among themselves to facilitate the estimate of the BaCN bond strength.

The data for the alkali halides are reproduced from Reference 30 in Fig. IV-11. The ordinate is the energy required for dissociation to ions and is given by

$$D_o(M^+X^-) = D_o^\circ(MX) + I(M) - E(X) \qquad (10)$$

where $D_o^\circ(MX)$ is the dissociation energy to atoms, and I(M) and E(X) are the ionization potential for the metal and the electron affinity of the halogen atom, respectively.

Reliable values for both the bond dissociation energy and bond length are available for only four alkaline earth monohalides, and these are plotted in Fig. IV-11. The other four points correspond to the Ba and Sr fluorides and chlorides for which there are good bond

strengths. For these, the bond lengths are estimates from Reference 16, which are arrived at by assuming that the ratios of the ionic radius of the metal ion in the dihalide to the radius in the monohalide is a constant for all of the Group IIA metals. Reference 16 estimates that the bond lengths thus derived are accurate to within .05 Å.

Figure IV-11 shows that the alkaline earth halides do not correlate with the alkali halides but do follow a similar trend. Although the correlation is quite sketchy at this point, the dashed curve is drawn through the points and is used for the estimate of D_o(BaCN).

Hartree-Fock calculations in Reference 4 indicate LiNC is marginally more stable than LiCN and that the Li-N bond distance is 1.77 Å. The calculated point charge distribution puts most of the net negative charge on the N atom; this suggests that r_e Li-N should be the proper bond length to use in correlating with other ionically bound molecules. The value of r_e(LiCl)[31] is 2.02 Å and the value of r_e(LiF) is 1.55 Å,[31] indicating an ionic radius for NC^- 0.25 Å less than Cl^- and 0.22 Å more than F^-. Using the bond lengths estimated by Krasnov and Karaseva[16] for BaF and BaCl, r_e(Ba-NC) is estimated as 2.46 and 2.50 Å, respectively. Using a curve drawn between the two BaX points which parallels the dashed curve, one obtains $D_o(Ba^+NC^-)$ = 162 kcal/mole for r_e = 2.48. Using Eq.(10) and the known ionization potential for Ba and electron affinity of CN,[32] one gets D_o(BaNC) $\cong$ 130 kcal/mole. If one uses the dashed curve one gets 124 kcal/mole. These are likely to be somewhat high because of polarizability of the CN^- ion, and therefore an arbitrary value of 120 is chosen. This value is highly

Fig. IV-11. Energies to dissociate ion pairs of alkaline earth and alkali metal halides. The solid points are the alkali data taken from Ref. 3. The triangles are data points which are well established; the open circles have well established D_o°'s, but somewhat uncertain r_e's. The dashed curve is an arbitrary fit.

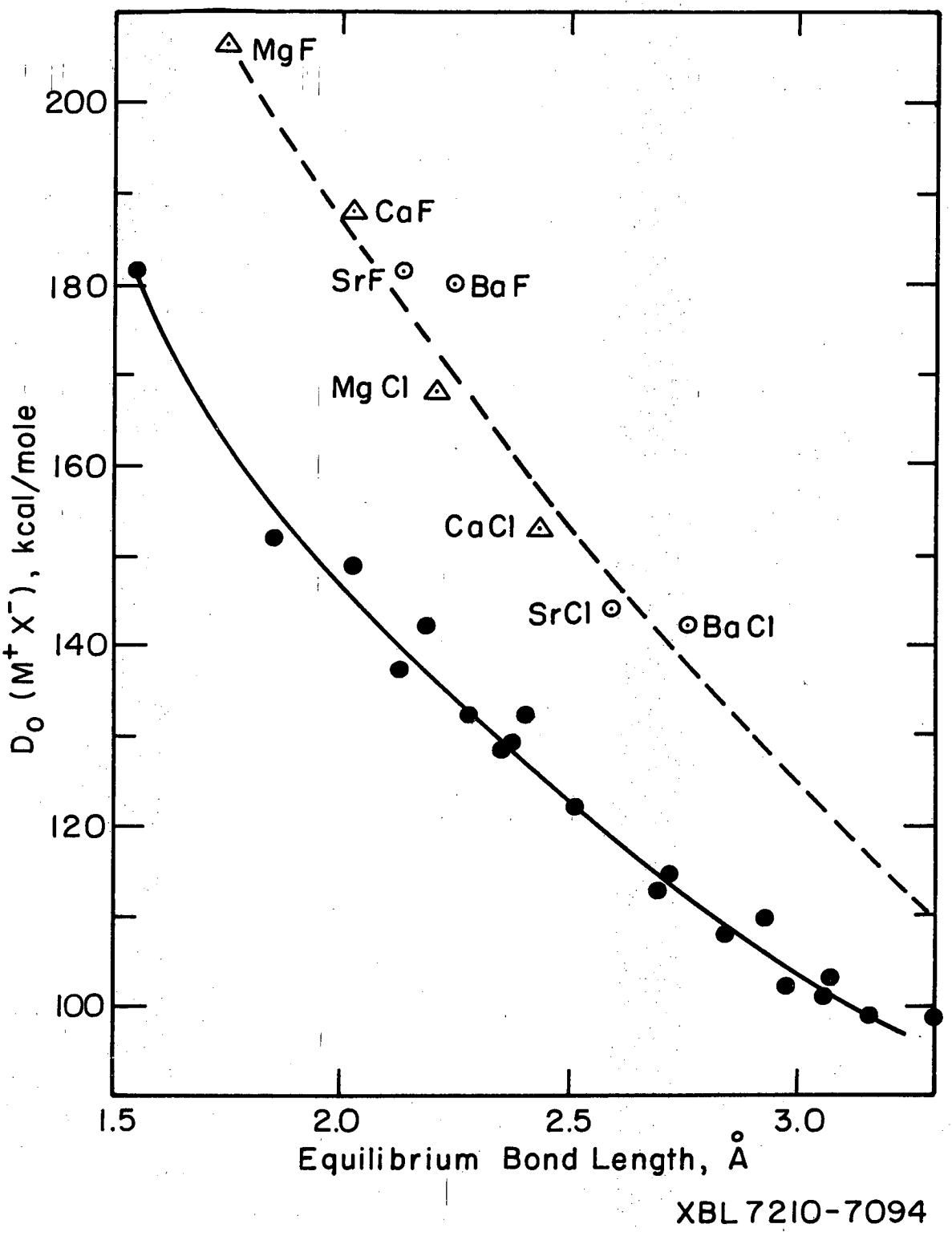
MgF
CaF
SrF
BaF
MgCl
CaCl
SrCl
BaCl
200
180
160
140
120
100
D_o (M^+X^-), kcal/mole
1.5
2.0
2.5
3.0
Equilibrium Bond Length, Å
XBL 7210-7094

Fig. IV-11.

questionable in that it is not known if the alkali cyanides correlate with the other alkali halides.

Using the r_e values in Reference 16, one can also obtain values for the alkaline earth bromides and iodides bond dissociation energies. Table IV compares these values with the ionic model calculations reported in Reference 16. Also included are lower limits established in Chapter III. It must be emphasized that these estimates are very tenuous, and more reliable data are needed to see if the alkaline earths actually do correlate well in this way. They might not be expected to, in that the bonding becomes progressively less ionic in the series Ba → Mg.[16]

Table IV. Alkaline earth monohalide bond strength[a]

MX	Bond strengths from Reference 16	Bond strengths from Figure 11[b] and Eq.(9)	Lower limits, Chapter III
MgBr	74 ± 15	64	-
CaBr	90 ± 15	84	-
SrBr	90 ± 15	85	-
BaBr	100 ± 15	87	77
MgI	55 ± 10	44	-
CaI	75 ± 15	65	64
SrI	80 ± 15	66	65
BaI	85 ± 15	70	66

[a] all energies in kcal/mole

[b] The ionization potentials and electron affinities used in Eq.(9) were from

I(M) - Handbook of Chemistry and Physics, 44th Edition (The Chemical Rubber Publishing Co., Cleveland, Ohio, 1963), pp. 2647-2648.

E(X) - R. S. Berry and C. W. Reimann, J. Chem. Phys. 38, 1540 (1963).

REFERENCES

1. G. H. Kwei and D. R. Herschbach, J. Chem. Phys. 51, 1742 (1969).
2. J. H. Birely, E. A. Entemann, R. R. Herm, and K. R. Wilson, J. Chem. Phys. 51, 5461 (1969).
3. D. D. Parrish and R. R. Herm, J. Chem. Phys. 51, 5467 (1969).
4. R. Grice, M. R. Cosandey, and D. R. Herschbach, Ber. Bunsenges. Phys. Chem. 72, 975 (1968).
5. J. C. Whitehead, D. R. Hardin, and R. Grice, Mol. Phys. 23, 787 (1972).
6. N. C. Blais, J. Chem. Phys. 49, 9 (1968); 51, 856 (1969).
7. M. Godfrey and M. Karplus, J. Chem. Phys. 49, 3602 (1968).
8. a. P. J. Kuntz, E.M. Nemeth, and J. C. Polanyi, J. Chem. Phys. 50, 4607 (1969).
   b. P. J. Kuntz, M. H. Mok, and J. C. Polanyi, J. Chem. Phys. 50, 4623 (1969).
9. M. C. Moulton and D. R. Herschbach, J. Chem. Phys. 44, 3010 (1966).
10. H. J. Loesch and D. R. Herschbach, J. Chem. Phys. 57, 2038 (1972).
11. J. A. Haberman, K. G. Anlauf, R. B. Bernstein, and F. J. Van Itallie, Chem. Phys. Letters (to be published).
12. S.-M. Lin, C. A. Mims, and R. R. Herm, to be published.
13. C. D. Jonah and R. N. Zare, Chem. Phys. Lett. 9, 65 (1971).
14. B. deB. Barwent, Bond Dissociation Energies in Simple Molecules, Nat. Stand. Ref. Data Ser., Nat. Bur. Stand. (U.S.), NSRDS-NBS 31 (1970).
15. D. L. Hildebrand, J. Chem. Phys. 52, 5751 (1970).

16. K. S. Krasnov and N. V. Kavaseva, Opt. Spectrosc. 19, 14 (1965).

17. B. Bak, E. Clementi, and R. N. Kortzeborn, J. Chem. Phys. 52, 764 (1970).

18. K. T. Gillen, A. M. Rulis, and R. B. Bernstein, J. Chem. Phys. 54, 2831 (1971).

19. These functions are special cases of functions used in E. A. Entemann, Ph.D. thesis, Harvard University, Cambridge, Massachusetts 1967. Also see this reference for a definitive discussion of analysis of LAB angular distributions.

20. T. T. Warnock, R. B. Bernstein, and A. E. Grosser, J. Chem. Phys. 46, 1685 (1967).

21. F. W. Lampe, J. L. Franklin, and F. H. Field, J. Am. Chem. Soc. 79, 6129 (1957).

22. J. Berkowitz and J. R. Marquart, J. Chem. Phys. 37, 1853 (1962).

23. D. L. Hildebrand, J. Chem. Phys. 48, 3657 (1968).

24. W. H. Hamill, J. Chem. Phys. 56, 4191 (1972).

25. J. Beynon, Mass Spectrometry and its Applications to Organic Chemistry (Elsevier Publishing Co., 1960) p. 211.

26. J. C. Light, Disc. Faraday Soc. 44, 14 (1967).

27. A recent review of crossed beams kinetics studies is given in: J. L. Kinsey, MTP International Review of Science, edited by J. C. Polanyi (Butterworths, London, 1972), Physical Chemistry Series One, Vol. 9, Chapter 6.

28. J. D. McDonald, P. R. LeBreton, Y. T. Lee and D. R. Herschbach, J. Chem. Phys. 56, 769 (1972).

29. R. K. B. Helbing and E. W. Rothe, J. Chem. Phys. 48, 3945 (1968).

30. R. R. Herm and D. R. Herschbach, J. Chem. Phys. 52, 5783 (1970).

31. L. Brewer and E. Brackett, Chem. Rev. 61, 425 (1961).

32. J. Berkowitz, W. A. Chupka, and T. A. Walter, J. Chem. Phys. 50, 1497 (1969).

V. REACTIONS OF ALKALINE EARTH ATOMS WITH SO_2, NO_2, SF_6, PCl_3, and $SnCl_4$

A. Introduction

In the study of the dynamics of chemical reactions by the molecular beams technique, two complementary avenues of exploration may be travelled. In the first, one seeks to determine the detailed dependence of a given reaction cross section on as many variables as is experimentally possible. In the other, a series of related reactions is studied qualitatively or semi-quantitatively in order to discern existing chemical trends. In the spirit of the latter method, this chapter presents measurements of laboratory (LAB) angular distributions of products from the reactions of alkaline earth atoms (M) with two oxygen containing compounds (SO_2 and NO_2) and three inorganic polyhalides (PCl_3, $SnCl_4$, and SF_6). The experimental success in studying this series of reactions is summarized in Table I.

The reactions of alkali metals (A) with these compounds have been studied in molecular beam experiments and found to exhibit a wide variety of chemical behaviors,[1] The scattering of the heavier alkali metals from NO_2 and SO_2[2] indicated a large cross section for the formation of an ANO_2^* or ASO_2^* complex. With SO_2, this complex must decay non-reactively due to the endoergicity of the AO+SO product channel. With NO_2, some decomposition into the AO+NO product channel apparently takes place because product AO molecules scattered from crossed beams of Na or Cs and NO_2 have been identified[3] by electric and magnetic deflection

Table I. Summary of Experimental Success

Reaction Partner	Alkaline Earth			
	Ba	Sr	Ca	Mg
NO_2	NA	R	R	EP (Ar^+)
SO_2	R	NR	NR	NA
$SnCl_4$	R	R	R	NR
PCl_3	R	R	F	NA
SF_6	R	EP (SF_4^+)	NR	NR

NA = Not attempted

NR = No product ions detected

EP = Experimental problem (interfering ion signal)

R = Reactive signal observed and angular distribution measured

F = Reactive signal observed, too small to allow angular distribution measurement

techniques. Products angular distributions from $A+NO_2$ have been determined (by a magnetic deflection technique) only for the Li reaction.[4] This study[4] indicates that $Li+NO_2$ produces a sharply forward scattered LiO product and resembles the ultra-direct mechanisms found for the alkali atom-halogen molecule reactions.

Early product angular distribution measurements for the reactions of the heavier alkali metals with $SnCl_4$,[5] PCl_3,[5] and SF_6[6] indicated a preference for forward scattering. However, later studies of K, Rb and $Cs+SF_6$ and $SnCl_4$[7] with velocity analysis of the products concluded that these reactions proceed by a long-lived complex mechanism and that the $SnCl_4$ reactions produce both ACl and $ASnCl_3$ products.[8] Product velocity distributions from this study[7] as well as the vibrational energy distribution of CsF from $Cs+SF_6$[9] are consistent with that predicted from the breakup of an intermediate complex in which the available energy is partitioned statistically. Studies of the reactions of Li with these polyhalides[4,10] also indicate broad angular distributions and low product translational recoil energy.

All of the reactant molecules studied here have appreciable electron affinities and the interactions of these molecules with alkali metals have been rationalized in terms of an electron transfer mechanism (see Discussion). This model pictures the transfer of a metal atom valence electron at reactant separations where the coulombic potential curve for the ion pair lies lower than the neutral curve. In the case of a low ionization potential for one reactant and a high electron affinity for the other, this transfer can occur at large reactant separations and has been used to explain the large reactive cross section of alkali metals with many electronegative species.

Because of the low ionization potentials of the heavier alkaline earth metals (notably Ba), one might expect behavior similar to that of the alkali metals. But as was noted previously, there could be different chemical forces acting in these reactions by virtue of the divalent nature of the group IIA metals. It must also be emphasized that while the reactions here are discussed in terms of the electron transfer mechanism, some of the calculated transfer distances are rather small (i.e., ~3 Å for $Ba+SO_2$). At these small separations it is inaccurate to speak of a simple electron transfer between reactants. However, even in these cases, it is still useful to picture the reacting system forming an ionic intermediate as the initiating step in the reaction. The reaction can still be roughly described in terms of the interaction[5] of the positive metal ion with the molecular negative ion.

B. Experimental

1. Apparatus

The apparatus, described in Ch. II, was used without modification. The SF_6, NO_2, and SO_2 were purchased in metal cylinders from Matheson Corp. and used without further purification. The source pressures were maintained at suitable levels in the gas line by admitting the gas through a Granville-Phillips leak valve. The PCl_3 was purchased from Mallinckrodt and the $SnCl_4$ from J. T. Baker. Both were contained in sample bulbs which were immersed in baths to maintain ~10 torr vapor pressure (ice water for $SnCl_4$, and a CCl_4 slush for PCl_3). The gas line pressure was regulated by the stopcock connecting the line to the

sample bulb. Both the $SnCl_4$ and PCl_3 were frozen, thawed, and degassed to remove any volatile impurities, particularly HCl resulting from hydrolysis. Table II lists the beam source temperatures and pressures used in these experiments. The collision chamber pressure was $\sim 1\times10^{-6}$ for the NO_2, PCl_3, and $SnCl_4$ experiments, but was as high as 4×10^{-6} for SF_6 and 6×10^{-6} for SO_2 (uncorrected ion gauge readings).

2. Beam velocity distributions

The beam velocity distributions for Ba, NO_2, and PCl_3 were measured as described in Ch. II. As noted, the number density speed distributions are fit by the following expression:

$$\rho_i(v_i) = A_i(v_i-a_i)^2 \exp\{-(v_i-a_i)^2/\alpha_i^2\} \qquad (1)$$

where all parameters are the same as described in Ch. II and where, as before, the subscripts i = 1 and 2 refer to the alkaline earth beam and gas beam respectively. The parameters used in the analysis of the data reported here are given in Table III. The parameters for Sr and Ca were derived from the measured Ba distributions as prescribed in Ch. II. In the case of $Ba+SO_2$, the Ba source pressure was in the range where the Li distributions reported in Ch. II approached thermal behavior. Therefore, a thermal distribution for Ba was assumed in this case. As has been previously noted, the deviation from a thermal distribution of the alkaline earth beam has little effect in the data analysis so that any error in this assumption is of little importance.

The distribution for SO_2 was obtained by multiplying the parameters for NO_2 by $(m_{NO_2}/m_{SO_2})^{\frac{1}{2}}$, where m is the mass of a given molecule. This

Table II. Beam Source Conditions[a]

Reaction	Alkaline earth beam		Gas beam	
	temperature	pressure[b]	temperature	pressure
$Sr + NO_2$	950	0.3	350	2.2
$Ca + NO_2$	1050	0.7	360	4.0
$Ba + SO_2$	950	0.05	360	4.0
$Ba + SnCl_4$	1030	0.3	360	3.8
$Sr + SnCl_4$	990	0.7	330	3.3
$Ca + SnCl_4$	1010	0.3	340	4.0
$Ba + PCl_3$	1040	0.3	360	3.5
$Sr + PCl_3$	990	0.7	350	3.2
$Ba + SF_6$	1060	0.4	340	2.2

[a] All temperature in °K; pressures in torr.

[b] Vapor pressure data taken from J. L. Margrave, The Characterization of High Temperature Vapors (John Wiley and Sons, Inc., New York, 1967).

Table III. Beam Speed Distributions[a,b]

Reaction	α_1	a_1	α_2	a_2
Sr + NO_2	3.8	1.3	3.6	2.0
Ca + NO_2	5.9	2.0	3.6	2.3
Ba + SO_2	3.3	0	3.1	2.0
Ba + $SnCl_4$	3.2	1.1	1.5	1.4
Sr + $SnCl_4$	3.8	1.3	1.5	1.3
Ca + $SnCl_4$	5.8	2.0	1.5	1.4
Ba + PCl_3	3.2	1.1	2.2	2.0
Sr + PCl_3	3.8	1.3	2.2	1.8
Ba + SF_6	3.2	1.1	2.0	1.4

[a] α_i and a_i are parameters in Eq.(1) where the subscripts i=1,2 refer to the alkaline earth and gas beams respectively; values in units of 100 m/sec.

[b] Results for PCl_3 and NO_2 based on actual measurement; those for SF_6, $SnCl_4$ and SO_2 based on extrapolation (see text).

is equivalent to using the same value of a_2/α_o (see Fig. II-12). The parameters used for SF_6 were obtained in a similar way from the CCl_4 results and those for $SnCl_4$ from the PCl_3 results. Although these are rather rough estimates of the velocity distributions, they are almost certainly much closer to reality than thermal distributions, and their use should eliminate a large fraction of the error in the data analysis which would result from assuming thermal conditions. An attempt was made to measure the velocity distribution for $SnCl_4$, but spurious results led to the suspicion that the data for the $SnCl_4$ reactions is not altogether trustworthy. This is discussed further in the data analysis section.

3. Detector

The angular distributions in all the reactions studied here were obtained by monitoring the MO^+ or MX^+ ion intensities (X = halogen atom). No other product ions were detected despite careful searches for them (notably $MSnCl_3^+$ and its possible daughter peaks and MX_2^+). Alkaline earth dihalides produce predominantly MX^+ upon electron bombardment ionization,[11] the effect being most pronounced for the fluorides and chlorides of the heavier metals. Thus, any MX_2 formed in the reactions here would produce mostly MX^+ in the ionizer and would be indistinguishable from that due to MX product. Attempts were made to identify the precursor of the MX^+ ions by measuring appearance potentials for their formation. These were unsuccessful because of the rapid decrease of both the available ionizing current and the ionization cross sections as the electron voltage was decreased. This reduced the ion signals

to "invisible" levels at electron energies far above expected threshhold values.

The study of reactions producing MgO were thwarted by the large background at mass 40 due to Ar^+. A large background at mass 108 attributed to SF_4^+ interfered with the study of the $Sr+SF_6$ reaction.

C. Results and Data Analysis

As discussed in the previous chapter, the measured intensity at a given LAB angle, Θ, is the result of (1) a transformation of the center of mass (CM) cross section $\sigma(\Theta,u,V)$ to laboratory coordinates, (2) an averaging of the transformation over the beam velocity distributions, and (3) integration over the unmeasured LAB recoil velocity, v, i.e.,

$$I(\Theta_{LAB}) = \int_0^{v^*}\int_0^{\infty}\int_0^{\infty} V\sigma(\Theta,u,V)\,\frac{v}{u^2}\,\rho_1(v_1)\rho_2(v_2)dv_1dv_2dv \quad (2)$$

where all variables are defined as in Ch. IV. Again the angle 0° in both frames of reference is defined by the direction of approach of the alkaline earth atom.

1. Data Analysis

The data are fit by assuming a form for the CM cross section, σ, and performing the integrations in Eq.(2). The resulting calculated LAB angular distribution is compared with the experimental data; the form of σ is varied until good fits to the data are obtained. Here again, σ is assumed to be independent of V, the incident relative

velocity, and also assumed to be separable in θ and u as before:

$$\sigma(\theta,u,V) = T(\theta)U(u) \qquad (3)$$

Although a recent study of $K+SnCl_4$ using a supersonic K nozzle beam[8] obtained a smaller reaction cross section than did Ref. 5 using a thermal K beam, analysis of nonreactively scattered K from $SnCl_4$ and SF_6[12] showed little dependence of the reactive cross section on initial relative kinetic energy. This behavior is also expected of any reaction which is pictured as proceeding by an electron transfer at relatively large reactant separations. If the forces between reactants at separations where the electron transfer occurs can be described by the long range $1/r^6$ potential, the reaction cross section should be proportional to $E^{-\frac{1}{3}}$.[13] This is a rather weak dependence, which for our purposes satisfies the assumption of an energy independent cross section.

The second approximation, that of separability in θ and u, is supported by recent velocity analysis studies of the $K+I_2$[14] and CH_3I[15] reactions. Only one reaction studied thus far, $K+CCl_4$,[16] has also shown a drastically coupled cross section. Of course, σ is uncoupled in any reaction which proceeds by formation of a long-lived complex.

In addition to the foregoing, one must guard against "overanalyzing" angular distribution data. The data can usually be fit by a family of uncoupled cross sections and, undoubtedly, a large number of coupled functions as well. The qualitative and semiquantitative features obtained from analysis using uncoupled functions would not be changed by the inclusion of mild coupling. Similar arguments hold for the

assumption of an energy independent cross section. Therefore, unless one expected Eq.(3) to be grossly in error, a more detailed analysis of the data would be unjustified.

For convenience, the functional forms used for $T(\theta)$ and $U(u)$ are the same as those used in Ch. IV, i.e.,

$$T(\theta) = (1-C)\exp\left\{-\ell n\, 2\left(\frac{\theta}{H}\right)^2\right\} + C\,, \tag{4a}$$

$$U(u) = (u/u_1)^{n_1}\left\{\exp\frac{n_1}{m_1}\left(1-\frac{u}{u_1}\right)^{m_1}\right\} \quad u < u_1$$
$$U(u) = (u/u_1)^{n_2}\left\{\exp\frac{n_2}{m_2}\left(1-\frac{u}{u_1}\right)^{m_2}\right\} \quad u > u_1 \tag{4b}$$

For SF_6, $T(\theta)$ was altered by reflecting the Gaussian part of the expression through $\theta = 90°$ in order to produce a forward-backward peaked distribution. Where it is instructive, an analysis which assumes a delta function for $U(u)$ is also included. As pointed out in Ch.IV, this single recoil energy (SRE) approximation should establish an upper limit to the width of the CM $T(\theta)$ curve for fairly anisotropic (decidedly forward or backward peaked) cross sections. For the SRE analysis, the form of $T(\theta)$ is not restricted to that of Eq.(4a).

Energetics. The translational recoil energy distribution is related to $U(u)$ (ignoring normalization) by $P(E') = P(u)/u$. If m_p is the mass of the detected product, and M is the total mass of the reaction system, then

$$E' = \tfrac{1}{2}\, m_p\, u^2/(1-m_p/M) \tag{5}$$

The total energy available to the products, $\mathcal{E}$, partitioned between recoil translational energy, E', and product internal excitation, W', is given by

$$E' + W' = \mathcal{E} = E + W + \Delta D_o \qquad (6)$$

where E and W are reactant relative kinetic energy and internal excitation, respectively, and ΔD_o is the difference in energies between the bond(s) formed and the bond(s) broken in the reaction.

Table IV gives E, W, and ΔD_o values for the reactions studied here. The E values were calculated from the peaks in the beam velocity distributions, and W was calculated assuming thermal equilibrium. The values for W may be somewhat high if a relaxation of internal energy occurs in the expansion from the gas beam source (see Ch. II).

Although bond dissociation energies of SO_2, NO_2, and the alkaline earth chlorides and fluorides involved here are relatively well known, the other bond strengths involved in these reactions are quite uncertain, and this is reflected in the ΔD_o listings in Table IV. In addition, the reactions with the polyhalides might produce either the monohalide or dihalide product. The ΔD_o values for the production of the dihalides are given in parentheses in Table IV. This difference in ΔD_o values implies different limits on the integration over v in Eq.(2) depending on which product is assumed. However, all of the U(u) distributions which fit the data for these reactions were confined to velocities much lower than that corresponding to $E' = \Delta D_o$ for either case, so that the difference in limits is of no importance.

Table IV. Reaction Energetics Data[a]

Reaction	Relative collision energy, E[b]	Reactant internal excitation, W[c]	Reaction exoergicity, ΔD_o[e]
$Sr + NO_2$	2.1	1.2	28-40
$Ca + NO_2$	2.5	1.2	21-43
$Ba + SO_2$	1.9	1.3	>4.8±2
$Ba + SnCl_4$	2.8	5.1	≈27 (~90)[f]
$Sr + SnCl_4$	2.6	4.5	~20 (~75)
$Ca + SnCl_4$	2.8	4.7	~18 (~75)
$Ba + PCl_3$	2.9	$1.1 + W_{vib}$[d]	~24 (~60)
$Sr + PCl_3$	2.6	$1.1 + W_{vib}$[d]	~15 (~50)
$Ba + SF_6$	2.5	3.4	~55 (~150)

[a] All values in kcal/mole

[b] Calculated using peak velocities in each beam

[c] Calculated assuming thermal equilibrium, using molecular constants in G. Herzberg, Molecular Spectra and Molecular Structure (D. Van Nostrand, Inc., Princeton, New Jersey, 1968).

[d] Molecular constants not reported, probably 2-3 kcal/mole.

[e] Bond dissociation energies were taken from: NO_2, SO_2 and PCl_3, V.I. Vedeneyev, et al., Bond Energies, Ionization Potentials and Electron Affinities (Edward Arnold, London, 1966); SF_6, J. Kay and M. Page, Trans. Far. Soc. 60, 1042 (1964); $SnCl_4$, total of four bonds reported in T.L. Cotrell, The Strengths of Chemical Bonds (Butterworths, London, 1958) divided proportionally to the $SiCl_4$ bonds reported in Vedeneyev, et al.; MCl and MF, D.L. Hildebrand, J. Chem, Phys. 52, 5751 (1970) and 48, 3657 (1969); MO range obtained by considering

Table IV (continued)

data from G. Gaydon, Dissociation Energies and Spectra of Diatomic Molecules, 3rd ed. (Chapman Hall Ltd., London, 1968), Vedeneyev, et al., and upper limit on $D_o(BaO)$ given in Ch. Ottinger and R. N. Zare, Chem. Phys. Lett. 5, 243 (1970).

[f] Numbers in parentheses refer to formation of MX_2 product.

2. The $M+SO_2$ and NO_2 results

The MO^+ LAB angular distributions are shown in Figs. V-1 to V-3. All three peak at smaller LAB angles than do the calculated angular distributions (assuming an energy-independent cross section) of the collision center of mass LAB velocity vectors. This indicates that the MO products are scattered predominantly into the forward CM hemisphere.

As mentioned in Ch. I, reactions producing alkaline earth monohalide (MX) products are especially suited to crossed beams studies because electron bombardment ionization of MX produces MX^+ (rather than M^+) almost exclusively. However, the situation is less favorable for ionization of MO. Mass spectral data are unavailable on the M^+/MO^+ fragmentation ratio for ionization of CaO or SrO because vaporization of these solid oxides proceeds with appreciable decomposition to the M atom; data on BaO indicate[17] comparable yields of Ba^+ and BaO^+ ions. If this fragmentation ratio, M^+/MO^+, were strongly dependent on the internal excitation of MO, it could severely hamper the interpretation of the experiments reported here where only the MO^+ product ion signal is measured. In the usual case, the M^+/MO^+ ratio will increase with increasing MO internal excitation. In this case, the product recoil energy distribution derived from the measured MO^+ LAB angular distribution would be distorted so as to indicate too low a probability for low recoil energy (and the high product internal excitation) reactive events. Furthermore, the derived product CM angular distributions could also be distorted in the event of significant coupling of the θ and E' distributions. In the ionization of the alkali halides, this fragmentation ratio varies

Figure V-1 Results for Sr + NO_2. Upper panel shows LAB data (circles), calculated distribution of collision center of mass vectors (dotted curve), and fits to the data. Lower panel shows CM functions which generate the fits to the data. Parameters which generate the $T(\theta)$ and $U(u)$ functions are given in Table V. The type of curve (dash, solid, etc.) is consistent (i.e., solid CM functions generate solid curve LAB fit, etc.). $P(E')$ is obtained from $U(u)$ by $P(E') = U(u)/u$. The "B" LAB fit is not shown, but is of equal quality to the other two fits.

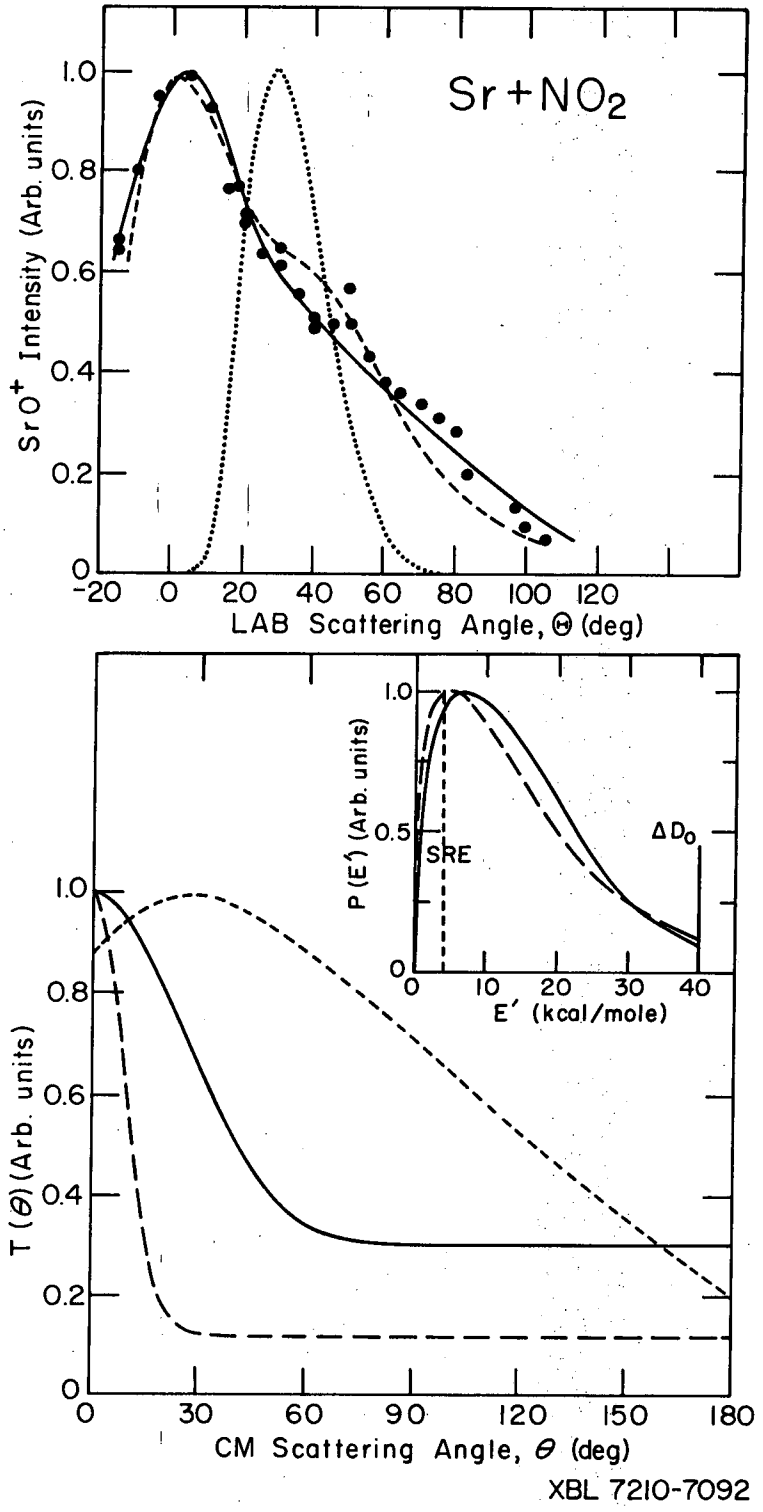
Sr+NO2
SrO+ Intensity (Arb. units)
LAB Scattering Angle, Θ (deg)
P(E') (Arb. units)
SRE
ΔD0
E' (kcal/mole)
T(θ) (Arb. units)
CM Scattering Angle, θ (deg)
XBL 7210-7092

Figure V-1

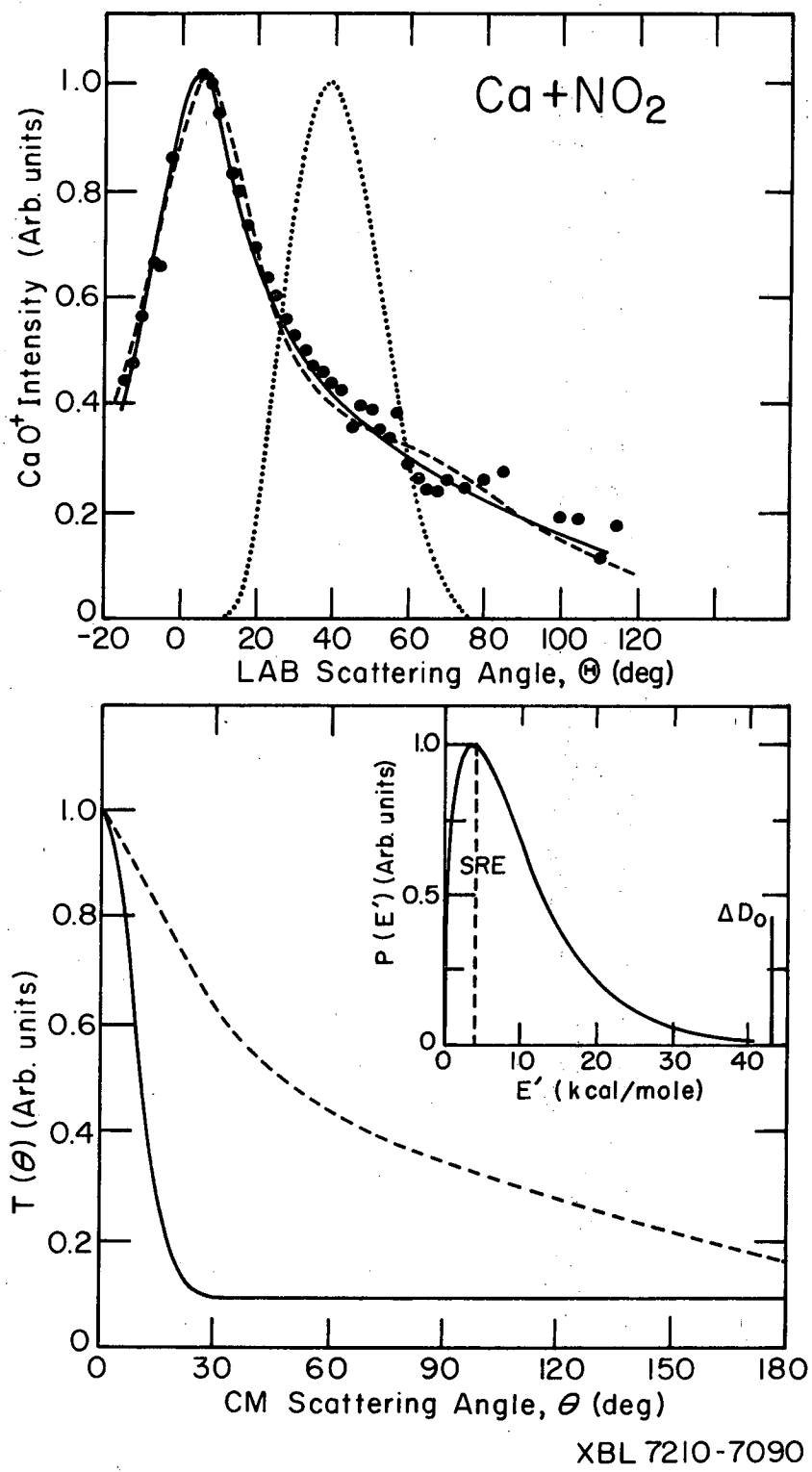

Figure V-2. LAB data, CM functions, and resulting LAB fits for $Ca + NO_2$.

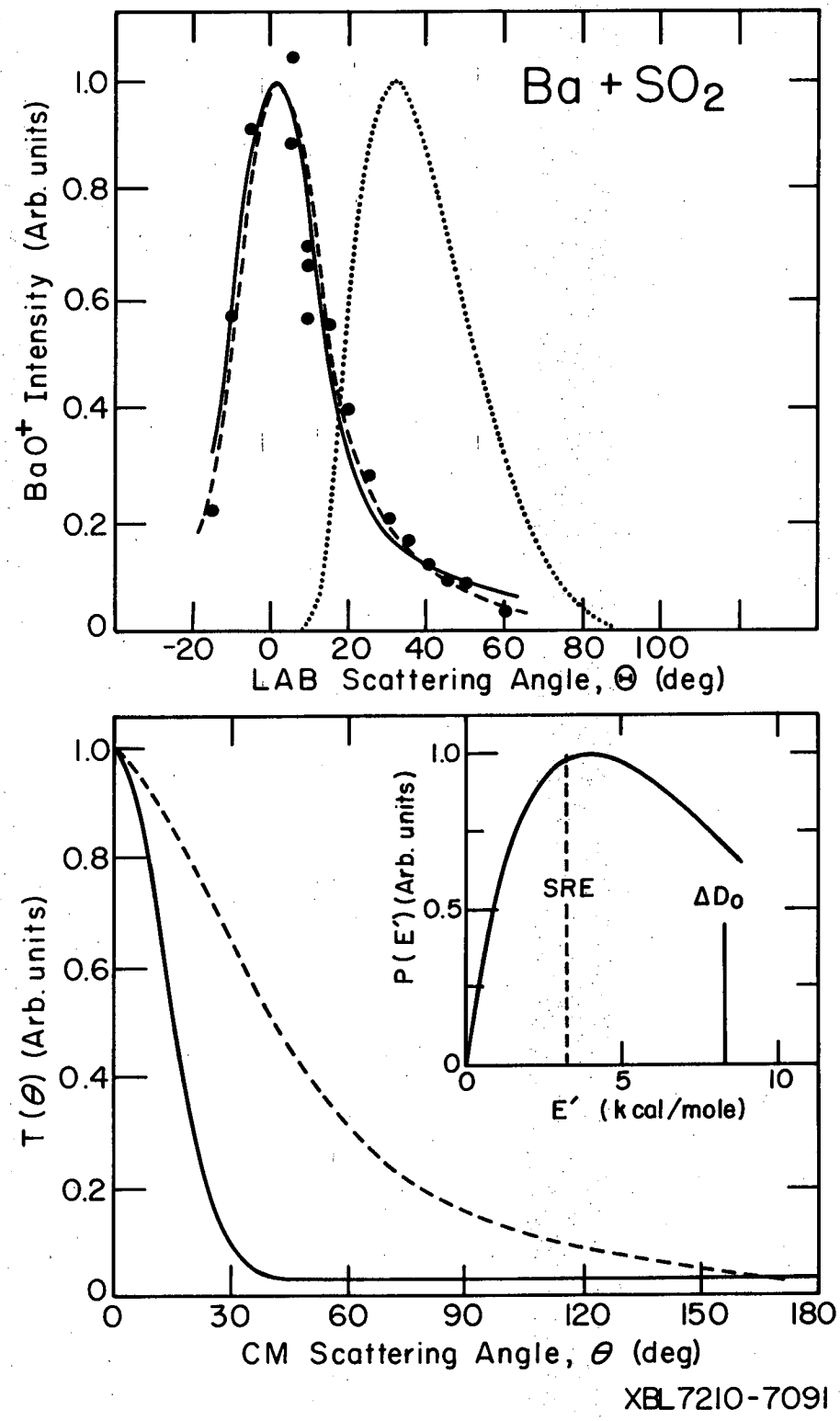

Figure V-3. LAB data and CM fits for Ba + SO_2.

drastically with AX internal excitation[18] so that it would be impractical to attempt to study alkali reactions with the equipment employed here.

However, the fragmentation ratio should be far less sensitive to internal excitation for ionization of alkaline earth mono-oxides because the MO^+ molecules should have appreciable dissociation energies (data in Ref. 17a suggest $D(BaO) \approx 70$ kcal/mole) whereas the alkali halide ions (AX^+) are bound predominantly by relatively weak ion-induced dipole forces. Other considerations also argue that the MO^+ distributions measured here should indicate the true CM reaction cross section behaviors. Thus, Table IV indicates that the $Ba+SO_2$ reaction is only marginally exoergic, so that the BaO product cannot be formed with appreciable internal excitation. Table IV does indicate considerably higher exoergicities for Ca and $Sr+NO_2$. However, the analyses of the measured MO^+ distributions which are presented in Figs. V-1 and V-2 and Tables V and VI indicate that the products prefer to separate with relatively small values of E'; any correction due to changing M^+/MO^+ fragmentation ratio would only further lower these E' estimates and would not alter the qualitative conclusions drawn here. Furthermore, Fig. V-4 indicates that the scattering of Sr from NO_2 produces an SrO^+ signal which exceeds that of Sr^+ at LAB angles > ~20° from the Sr beam. Since the detector sensitivity for Sr and SrO should be similar (indeed, probably favors Sr slightly), this clearly indicates a rather large (i.e., ~50-100 $Å^2$) cross section for the reaction. Furthermore, experience with the mass spectral cracking patterns of a variety of gases in this apparatus suggests that fragment ions are focussed through the massfilter with

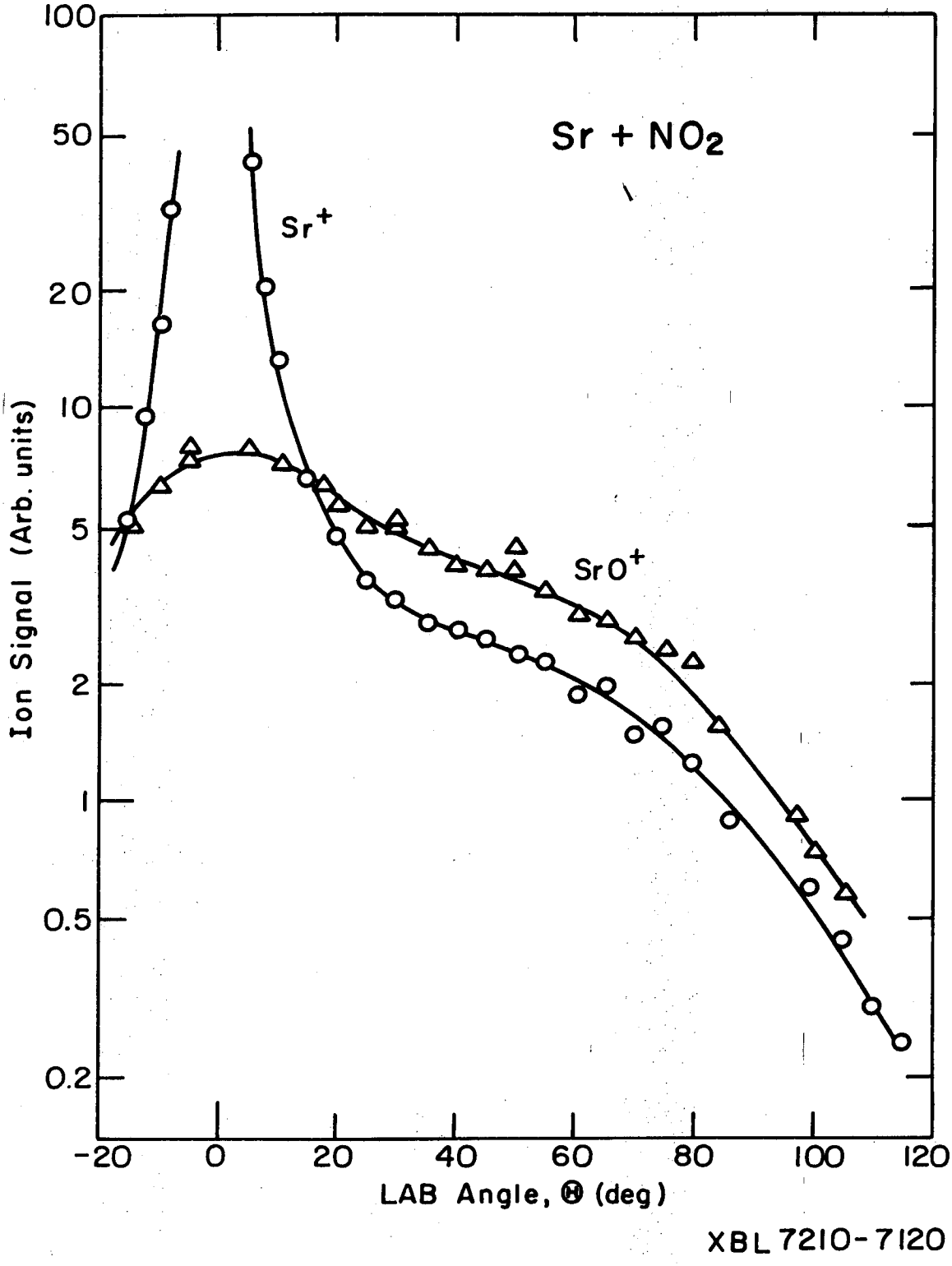

Figure V-4. LAB scattered intensities for both Sr^+ and SrO^+ ion signals from Sr + NO_2.

Table V. CM Cross Section Parameters[a]

Reaction	Legend	T(θ) H	T(θ) C	U(u) u_1	U(u) n_1, m_1, n_2, m_2
Sr + NO_2	SRE[b]	-	-	-	-
	A	30.	0.30	5.0	2, 2, 2, 3
	B	10.	0.12	4.5	2, $1\frac{1}{2}$, 2, 2
Ca + NO_2	SRE	-	-	-	-
	A	10.	0.09	6.0	2, 2, 2, 2
Ba + SO_2	SRE	-	-	-	-
	A	15.	0.03	2.8	3, 2, 2, 3
Ba + PCl_3	SRE	-	-	-	-
	A	20.	0.10	3.2	2, 1, 2, 2
	B[c]	90.	0.00	3.0	3, 2, 2, 3
Sr + PCl_3	SRE	-	-	-	-
	A	150.	0.00	3.5	4, 2, 2, 4
	B	20.	0.30	4.0	2, 1, 2, 2
Ba + SF_6	A(——)	20.	.40(.75)[d]	3.0	2, 1, 2, 2
	B(——)	20.	.40(1.0)	3.0	2, 1, 2, 2
	A(- - -)	250.	0.0	2.3	4, 2, 2, 4
	B(- - -)	∞	0.0	2.3	4, 2, 2, 4
Ba + $SnCl_4$	SRE	-	-	-	-
Sr + $SnCl_4$	SRE	-	-	-	-
Ca + $SnCl_4$	SRE	-	-	-	-

[a] Parameters defined in Eq.(4) for CM cross sections.

[b] SRE fits are not restricted to the form of Eq.(4).

[c] Fit not shown in figures, but gives equally satisfactory fit.

[d] Gaussian part of T(θ) reflected about θ = 90° and multiplied by number in parentheses.

Table VI. CM Cross Section Characteristics

Reaction	Legend	Q_f[a]	$\bar{E}'$[b]	$\langle E' \rangle$[c]
$Sr + NO_2$	SRE	.61	4.0	4.0
	A	.59	6.9	10.0
	B	.54	4.4	8.4
$Ca + NO_2$	SRE	.64	4.0	4.0
	A	.55	3.5	6.5
$Ba + SO_2$	SRE	.82	3.3	3.3
	A	.72	4.0	3.7
$Ba + PCl_3$	SRE	.72	2.8 (5.2)[d]	2.8 (5.2)
	A	.64	1.4 (2.5)	4.8 (8.7)
	B	.72	3.3 (6.0)	4.8 (8.7)
$Sr + PCl_3$	SRE	.58	2.0 (4.0)	2.0 (4.0)
	A	.59	2.9 (5.7)	3.7 (7.3)
	B	.55	1.3 (2.6)	3.9 (7.7)
$Ba + SF_6$	A (——)	.51	1.0 (1.3)	3.4 (4.5)
	B (——)	.50	1.0 (1.3)	3.4 (4.5)
	A (---)	.53	1.6 (2.6)	2.1 (2.8)
	B (---)	.50	1.6 (2.6)	2.1 (2.8)
$Ba + SnCl_4$	SRE	.72	4.0 (5.7)	4.0 (5.7)
$Sr + SnCl_4$	SRE	.72	4.0 (6.1)	4.0 (6.1)
$Ca + SnCl_4$	SRE	.71	4.0 (7.0)	4.0 (7.0)

[a] Q_f = fraction scattered into forward CM hemisphere, given by

$$\int_0^{\pi/2} T(\theta) \sin\theta \, d\theta \Big/ \int_0^{\pi} T(\theta) \sin\theta \, d\theta$$

[b] $\bar{E}'$ = maximum in P(E'), given by $dP(E')/dE' = 0$

[c] $\langle E' \rangle$ = average recoil translational energy, given by

$$\int_0^{\Delta D_o} P(E')E'dE' \Big/ \int_0^{\Delta D_o} P(E')dE'$$

[d] Numbers in parentheses are for assumed dihalide product.

efficiences comparable (i.e., within a factor of two) to those for parent ions, so that the data of Fig. V-4 also indicate that the Sr^+/SrO^+ fragmentation ratio for ionization of SrO is unity or less. Finally, the approximate correspondence of the shapes of the measured Sr^+ and SrO^+ curves for a wide range of LAB angles suggests that most of the Sr^+ signal in this range arises from fragmentation of SrO^+; this, in turn, further indicates that the Sr^+/SrO^+ ratio is independent of LAB angle, and thus is approximately constant for different product recoil paths.

The CM fits obtained for the $M+NO_2$ reactions are shown in Figs. V-1 and V-2, and the values of the parameters for the $T(\theta)$ and $U(u)$ functions which produce these fits are listed in Table V. The fractions of product scattered into the forward hemisphere, given by

$$Q_f = \int_0^{\pi/2} T(\theta) \sin\theta \, d\theta \Big/ \int_0^{\pi} T(\theta) \sin\theta \, d\theta ,$$

and E' and $\langle E' \rangle$, the peak and average translational recoil energies respectively, are tabulated in Table VI.

These data are in good agreement with the results reported in Ref. 19 for $Ba+NO_2$. The cross sections all peak sharply forward in the CM system with a rather small fraction of the exoergicity appearing as translational recoil energy. One cannot conclude from these data whether the CaO cross section is narrower inasmuch as the A fit to the Ca data is very similar to the B fit to the Sr data. The wider range of fits obtained for $Sr+NO_2$ is probably simply due to poorer kinematics in this system.

The accuracy of the Ba + SO_2 data is somewhat in question due to high collision chamber pressures (~ 6×10^{-6}) during the experiment. This pressure was observed to attenuate the Ba beam by ~15%, or ~3 times as much as did a typical gas beam. If this background were due entirely to SO_2, and if it were all modulated at the gas beam chopping frequency, then a viewing factor correction would be necessary which would reduce the intensity at $\Theta = 0°$ by a factor of 3 relative to that at $\Theta = 90°$. Even this would not be enough to change the qualitative shape of the measured angular distribution (i.e., the peak at small LAB angles). Furthermore, the pumpout time of the collision chamber (i.e., chamber volume divided by pumping speed) is 100 msec. This is slow compared to the gas beam chopping cycle (25 msec) so that even if all the background originated in the chopped beam, less than 25% would be modulated. Moreover, most of the non-condensible background would enter from the open bottom of the gas oven cold shield, and therefore not be modulated in the first place. It is possible that even higher pressures inside the gas beam cold shield could have broadened the gas beam considerably. In view of its short path length compared to that of the metal beam, however, it is hard to imagine a gas beam attenuation of more than 15%. This would not distort the beam profile sufficiently to produce any noticeable viewing factor problems. Thus, it seems unlikely that the measured SO^+ distribution in Fig. V-3 is appreciably distorted by a viewing factor error.

The CM fits to the data obtained by applying no viewing correction are shown in Fig. V-3, and the parameters for these functions are given in Table V. As shown, this reaction is also fit by a sharply forward

peaked angular distribution. Although the calculated recoil energy is rather low, it is a major portion of the estimated reaction exoergicity.

3. The M + polyhalide results

The LAB data for Ba + SF_6 are presented in Fig. V-5. As shown, the BaF^+ angular distribution is rather broad and shows comparable intensities on either side of the calculated distribution of centroids. In view of the results obtained with alkali metals, attempts were made to fit the data with $T(\theta)$ distributions which were symmetric about 90°. This behavior is predicted for a reaction which proceeds by a "sticky complex" mechanism (a collision complex which lives for several rotational periods). The form of the CM angular cross section in the case of a long-lived complex is determined solely by angular momentum considerations. Two distributions were used, one of which is flat and is the result predicted when the complex has no "memory" of the direction of the initial velocity vector.[20] The other $T(\theta)$ distribution used is noticeably forward-backward peaked and is similar to the result obtained for Cs + SF_6. This form is predicted if the complex has some memory of the initial relative velocity vector and if critical configuration for separation to products has prolate top symmetry.[20] The resulting fits (B) are shown in Fig. V-5. These indicate that the calculated LAB intensities are slightly too high at wide angles. If the CM curves are attenuated in the backward hemisphere, the resulting fits to the data (A) are quite good. The parameters for these fits are given in Table V and the E' and Q_f values are listed in Table VI.

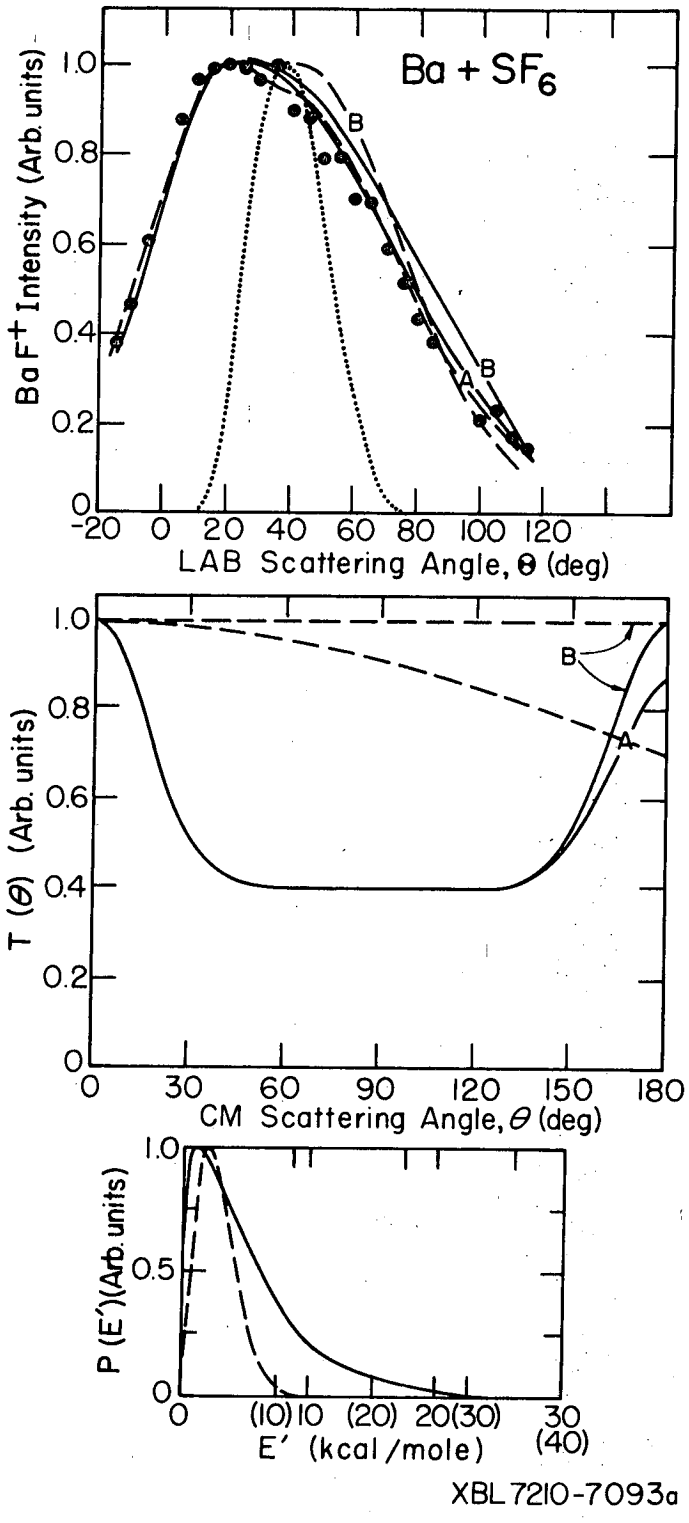

Figure V-5. LAB data and CM functions which generate LAB fits for Ba + SF_6. The "B" curves are symmetric about $\theta = 90°$.

The "A" T(θ) curves are consistent with the result predicted for a collision complex which "lives" for up to several rotational periods. These so-called "osculating" complexes have been observed in various metal-salt and salt-salt reactions.[21]

There are sufficient uncertainties in the data analysis to prevent the elimination of a symmetric CM cross section for this reaction (i.e., unequivocally state that the "A" distributions of Fig. V-5 better describe the reaction than do the "B" distributions). The high apparatus pressure (4×10^{-6}) might have introduced a viewing factor which slightly emphasized the scattering at small LAB angles. The smooth behavior of the data near $\Theta = 0°$ and discussions presented in connection with the SO_2 results argue against this, however. A more serious uncertainty is that connected with the SF_6 beam velocity distribution. Auxiliary calculations indicate that if the a_2 parameter in Eq.(1) for SF_6 were reduced to 1.0 (from 1.4), the data could be fit by the symmetric "A" T(θ) curves.

The P(E') curves are also shown on Fig. V-5. The U(u) curves used in the fits correspond to different P(E') curves for different assumed reaction channels due to the difference in the corresponding mass factors in Eq.(5). The abscissa numbering scheme which is enclosed in parentheses on the P(E') plots of Fig. V-5 shows E' values for scattering of $BaF_2 + SF_4$ products; the second abscissa numbering scheme plots E' values for scattering of $BaF + SF_5$ products. Due to the mass factors involved, the difference is rather small for this reaction. In either case, the E' values correspond to a very small fraction of the available energy.

The LAB angular distributions of MCl^+ from the reactions Ba and Sr + PCl_3 are shown in Figs. V-6 and V-7. The $SrCl^+$ signal was much weaker than the $BaCl^+$ intensity. A weak $CaCl^+$ signal was observed from Ca + PCl_3 as well, but the intensity was too weak to allow a meaningful angular distribution measurement. Derived CM distributions and the corresponding fits to the data are shown in Figs. V-6 and V-7; the parameters are given in Table V. As for Fig. V-5, Figs. V-6 and V-7 include E' scales for both MX + PCl_2 and MX_2 + PCl product channels. As is shown in these figures and in the Q_f value in Table VI, the Sr reaction is fit by a broader $T(\theta)$ curve than is the Ba reaction. Again, the E' values represent a small part of the reaction exoergicity for either assumed product channel.

The MCl^+ LAB angular distributions from the Ba, Sr, and Ca + $SnCl_4$ reactions are given in Fig. V-8. They all peak at values of Θ near the alkaline earth beam, indicating a preference for forward scattering. The arrows indicate the location of the maxima in the calculated centroid vector distributions. The wide angle data for Sr + $SnCl_4$ were unobtainable due to a high background level in the detector.

Unfortunately, there are experimental uncertainties in these data also. An attempt to measure beam velocity distributions for $SnCl_4$ gave spurious results which suggested that the $SnCl_4$ beam was significantly broader than the profile calculated for the collimation employed. Subsequent beam profile measurements indicated that the beam was broad and shifted ~5° in LAB angle from all other gas beams. The beam profile was measured with AC detection. Since the beam was modulated,

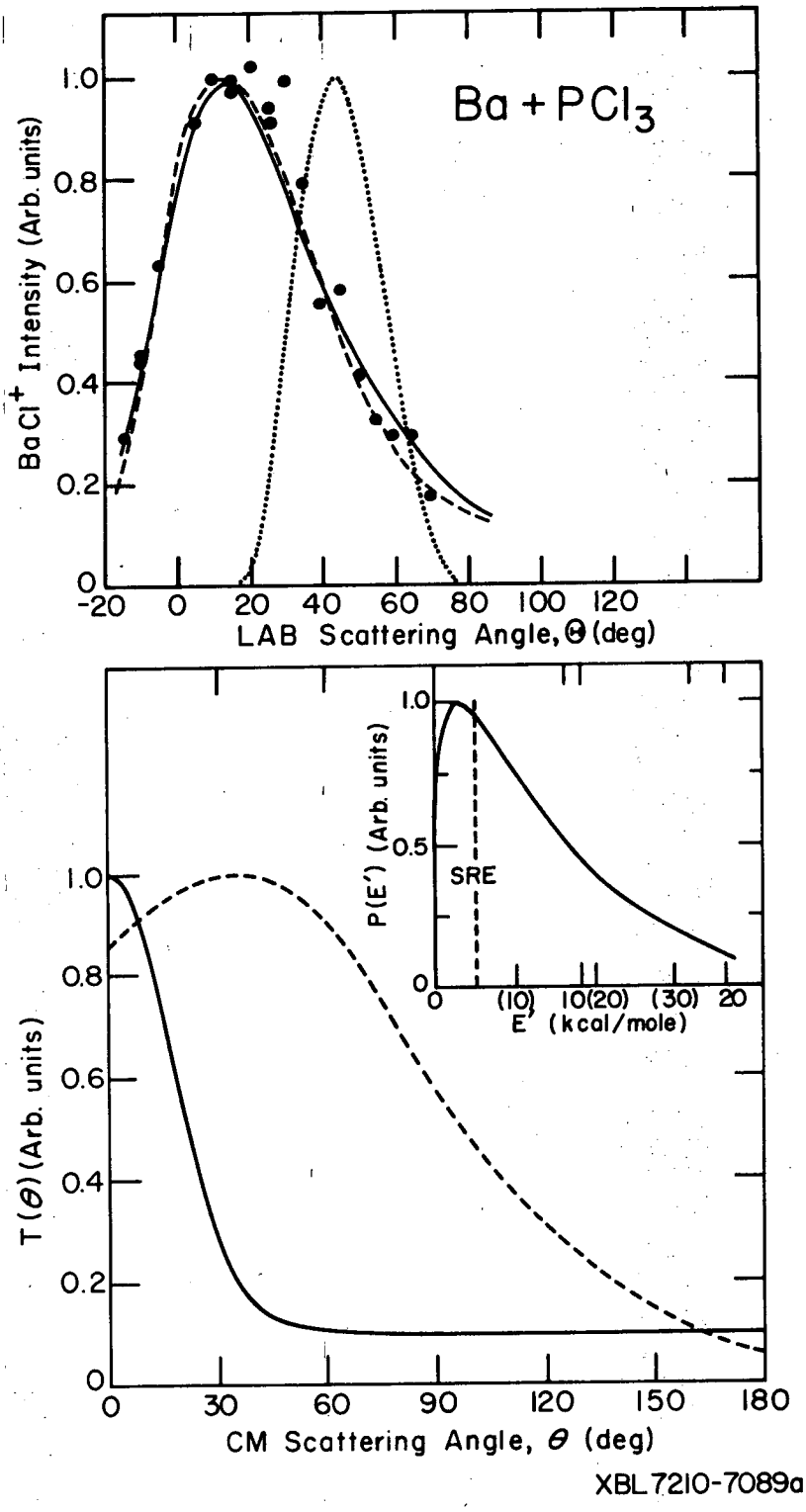

Figure V-6. Measured LAB data and derived CM distributions for $Ba + PCl_3$.

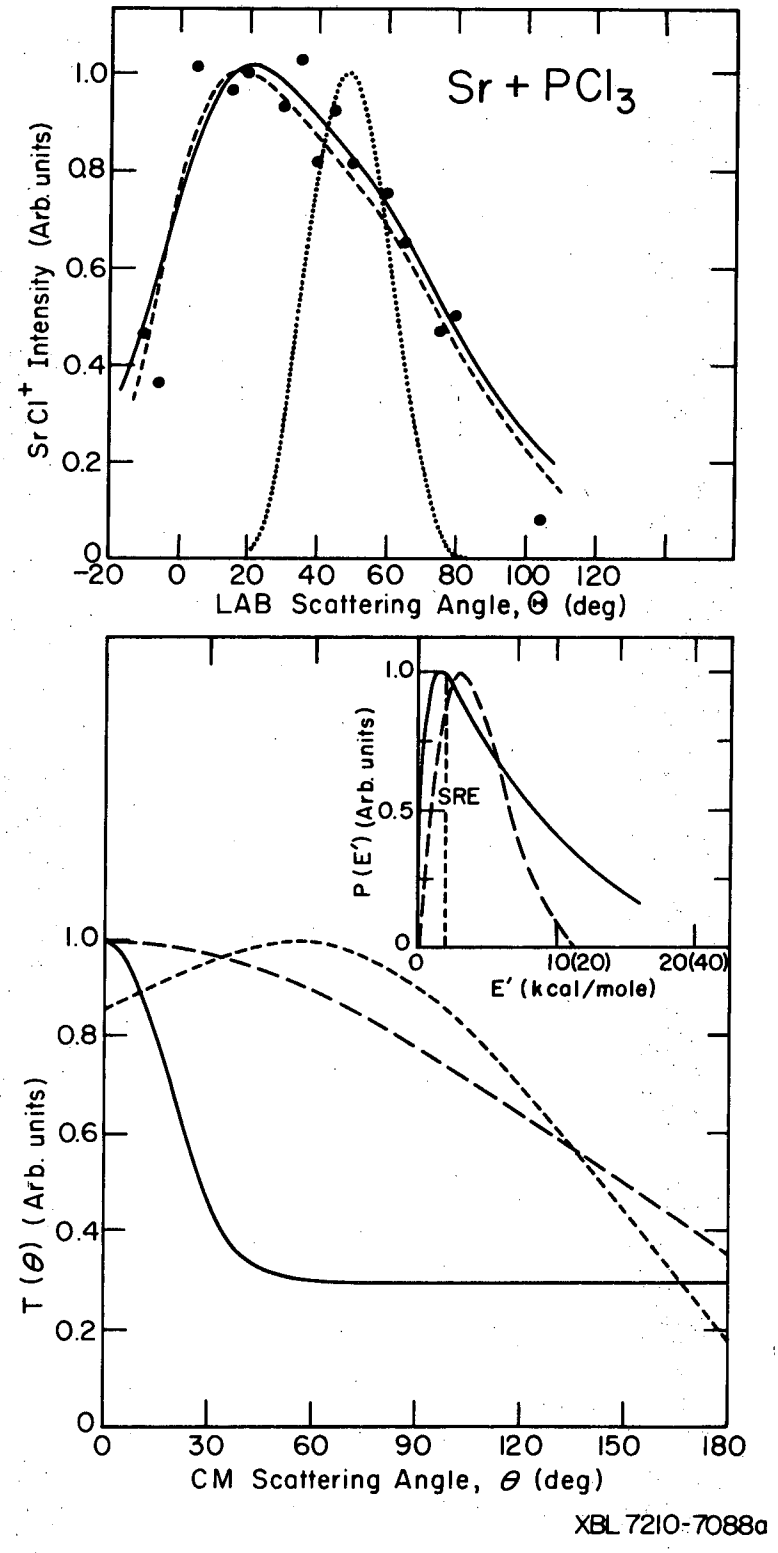

Figure V-7. Results for Sr + PCl_3. The "A" LAB fit is not shown but is equal in quality to the other two.

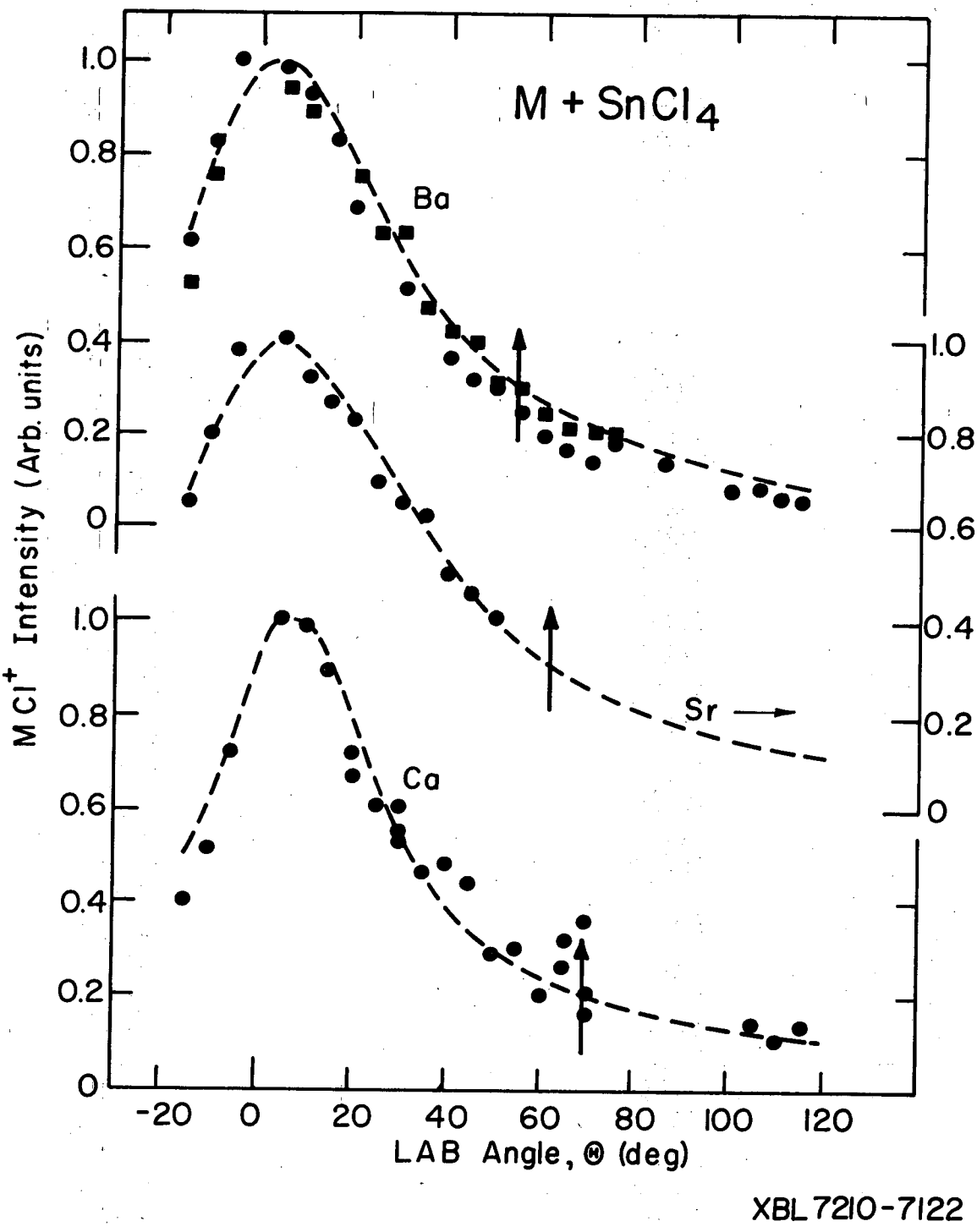

Figure V-8. Measured MCl^+ LAB angular distributions for Ba, Sr, and Ca + $SnCl_4$. Also shown are SRE fits to the data (dashed curves) and angles of the most probable collision center of mass vectors (arrows).

it must have come through the collimator slit , because the chopping wheel is behind it. Given the fact that the beam passed through the collimator, the 5° shift corresponds to a 0.1 cm misalignment at the collision zone. As shown in Fig. II-7, this prescribes a 20% correction to the narrow angle data. This would not significantly alter the shape of the angular distributions. However, because of the detector collimator, any molecules which "miss" the collision zone by more than ~0.12 cm cannot be seen by the detector. The beam profile had not dropped significantly in intensity at angles corresponding to this misalignment, thus implying an appreciable beam intensity invisible to the detector with even greater misalignment. If this were true, there is a good possibility of the measured LAB distributions being qualitatively wrong.

In view of this uncertainty, only the SRE analyses was performed on these data. The resulting CM curves which provide the fits to the data are shown on Fig. V-9. They all peak rather sharply in the forward hemisphere, in contrast to the results obtained in the alkali metal reactions.

D. Discussion

$M + NO_2$

The results obtained here for Sr and Ca + NO_2 are very similar to the results for Ba + NO_2 reported in Ref. 19. They are also in agreement with the only reliable[4] angular distribution for reactive scattering of NO_2 from an alkali metal. Although the electron affinity of NO_2 is in

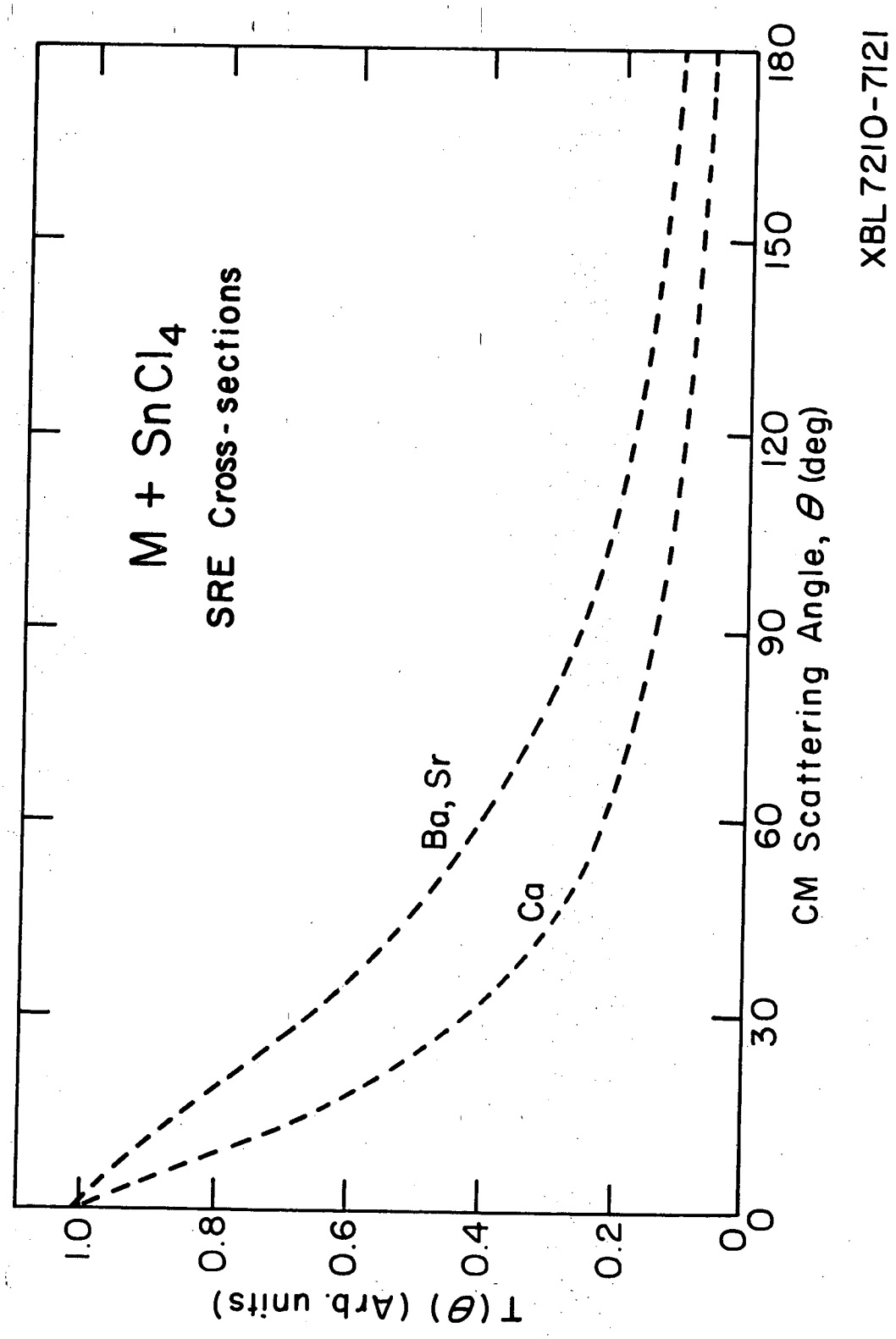

Figure V-9. SRE CM angular distributions which generate the fits to the data shown in Figure V-8.

dispute, it is certainly greater than 2.0 eV,[22] and an electron transfer is expected to take place at relatively large reactant separations for reactions of NO_2 with metal atoms. Total reaction cross sections for Ba and Ca + NO_2 are close to those predicted by the electron jump model.[23] The CM cross sections measured here exhibit the phenomenological behavior that was observed in the reactions of halogens with alkali metals. This behavior was also observed in the Li + NO_2[4] study despite the small reaction exoergicity and the seemingly ideal situation for formation of a collision complex. Therefore, it seems likely that NO_2 behaves much like the halogen molecules, with the electron transfer forming a weakly bound NO_2^- negative ion which is pulled apart by the metal positive ion early in the reaction trajectory. In this light it is not surprising that the more exoergic reactions with alkaline earths show behavior similar to that found with Li.

Ba + SO_2

Although the reported value for the electron affinity of SO_2 is lower (1.1 eV),[24] the electron transfer model has been used to explain its collisional quenching of the fluorescence of electronically excited sodium.[25] The large cross sections for the formation of collision complexes in the system K + SO_2 can also be understood in this way. The situation here is presumably similar to that of Li + NO_2 with the possibility of a chemical well and limited energetics. Similar results are obtained as evidenced by the sharply forward peaked cross section.

Ba + SF_6

The T(θ) functions here suggest the formation of a collision complex. The reactive scattering differential cross sections of K, Rb, and Cs with SF_6 are consistent with collision complex formation.[7] Furthermore, vibrational[9] state distributions of the CsF product from Cs + SF_6 are consistent with those predicted from the statistical breakup of a $CsSF_6$ complex. When the SF_6 was heated in Ref. 9a, the additional initial internal energy thus introduced was also partitioned into CsF vibration in accord with statistical complex theory.

According to transition state theory, the final translational energy distribution of the products[26] (ignoring effects of the centrifugal barrier in the exit channel) is given by

$$P(E') = N^{\dagger}(\mathcal{E}-E') \qquad (7)$$

where E' and $\mathcal{E}$ are defined in Eq.(6). $N^{\dagger}$ is the energy level density of active vibrations in the complex and in the classical limit is given by

$$P(E') = (\mathcal{E}-E')^{n} , \qquad (8)$$

The number of active modes, n, depends upon the geometry and "looseness" of the complex, but is of the order of 16 for any assumed form for $BaSF_6^*$. The average product translational energy <E'> (defined in Table VI) for a distribution given by Eq.(8) is simply

$$\langle E' \rangle = \mathcal{E}/(n+2) \qquad (9)$$

The inclusion of exit barrier effects would only serve to raise this value.

Using a value of n of 16 for the Ba + SF_6 reaction, one predicts values of <E'> of ~3 and ~9 kcal/mole for reaction to form BaF and BaF_2 products, respectively. The value for formation of BaF is in reasonable agreement with the <E'> values associated with the CM fits obtained here. The prediction for BaF_2 formation is clearly too high to be consistent with these results.

Preliminary results of a laser induced fluorescence study[27] of the BaF product of this reaction indicate a Boltzmann distribution in vibrational excitation characterized by a temperature of 1400°K. This is also in excellent agreement with the predictions of statistical complex theory. This, along with the present results, indicates the formation of a collision complex which decays statistically to form BaF + SF_5.

As stated before, the BaF^+ signal in this experiment could have come from either BaF or BaF_2. The formation of BaF_2 liberates around three times the energy that formation of BaF does. If two product channels exist with $\mathcal{E}_1$ and $\mathcal{E}_2$ total energy available respectively, RRKM theory predicts[13] that the ratios of the rate constants for the formation of the two products will be

$$(\mathcal{E}_1/\mathcal{E}_2)^{s-1} \quad . \tag{10}$$

The ratio of frequency factors for passage through the barrier has been set equal to unity and the number of oscillators, s, is given by $3N-5\frac{1}{2}$. For the Ba + SF_6 reaction the above formula predicts the BaF_2 channel should dominate by a factor of 3^{17}. As has been noted, the results are not consistent with the formation of BaF_2 from a complex.

Perhaps BaF_2 is the major product, but the translational recoil mode is not receiving its share of the total available reaction energy. This might be caused either by the formation of one of the products in an excited electronic state or by a direct reaction mechanism which nevertheless gives a broad angular distribution. The prediction of branching ratios based on Eq.(10) assumes the same activated complex for both product channels. This is probably not true and the existence of a steric or energetic barrier in the BaF_2 product channel could account for BaF being a major product. The laser induced fluorescence results[27] indicate an appreciable cross section to form the BaF product. No fluorescence attributable to BaF_2 was seen, although its detection would depend on BaF_2 having an absorption spectrum in the region scanned by the laser.

Again, the electron affinity of SF_6 is small (~1.5 eV),[28] and electron transfer separations are small as evidenced by the presence of rainbow structure in the elastic scattering of $K+SF_6$,[29] and glory maxima in the scattering of $Na+SF_6$.[30] Arguments pertaining to the molecular orbitals of SF_6^- are used in Ref. 7 to explain the propensity of alkali + SF_6 reactions to form collision complexes, showing that the electron transfer model is useful in describing the interaction in the SF_6 + metal atom reactions.

M + PCl_3

The electron affinity of PCl_3 is probably smaller as evidenced by the smaller reactive cross sections with alkali metals.[10] At this time, no velocity analysis results of $A+PCl_3$ reactive scattering have been

reported. The CM cross sections derived for reactions of the heavier alkali metals from measured primitive product angular distributions indicated that the reaction proceeded by a forward peaking, direct mechanism.[5,8] Reference 5, however, was the same one that erroneously reported that A+$SnCl_4$ proceeds by a similar mechanism. Product angular distribution measurements from Li+PCl_3[10] indicated that the cross section is approximately symmetric about $\theta = 90°$ in the CM system.

The Ba+PCl_3 results here show a definite preference of the products for the forward hemisphere, while the result for Sr shows much less preference. This coupled with the much smaller reactive signal for Sr reaction can be rationalized by taking into account the large ionization potential of Sr. In the electron transfer picture, this implies smaller reactant separations when attractive ionic chemical forces become dominant, and, as a result, smaller reaction cross sections. In fact, the separations calculated for electron transfer in these systems are small enough (~3 Å for Sr+PCl_3)[31] to render the picture shaky. However, there might be a potential barrier in the "neutral-neutral" surface which is avoided in the Ba reaction by shifting of a charge from the Ba earlier in the reaction trajectory. The smaller cross section for Sr could also imply more complicated reaction trajectories and therefore broadened CM angular distribution. Carrying this trend further, one can also explain the very weak signal from the Ca+PCl_3 reaction. It would be interesting to see if the Ca reactive scattering continued the trend to broader or backward peaking behavior.

The identity of the product is in doubt here, as MCl^+ could arise from either MCl or MCl_2 or both. The present data do not aid in determining the product identity.

$M + SnCl_4$

As has been noted, the data for the $M + SnCl_4$ reactions are somewhat uncertain, and, therefore, a terse discussion is in order here. If the strongly forward peaking behavior indicated here is correct, this is in contrast to the results with alkali metals, whose reactions showed "sticky complex" behavior. This might occur because of the ability of alkaline earth metals to extract two chlorine atoms. The photodissociation process, $SnI_4 + h\nu \rightarrow SnI_2 + I_2^*$, is known.[32] Perhaps a similar dissociative state in $SnCl_4$ is excited upon reaction with alkaline earth metals, thus allowing exchange of two halogen atoms in a direct mechanism. This would be a very interesting occurrence, and therefore this system warrants more study.

Also interesting here is the absence of any evidence of an $MSnCl_3$ product, despite careful searches for any evidence of it in the Ba, Sr and Ca reactions. Because of kinematic considerations discussed in Ch. IV, the apparatus is more sensitive to this heavier product than to a mono- or dihalide product if both are scattered with comparable recoil energies. The fact that no $MSnCl_3$ is seen implies that the cross section for its formation is very small compared to that for the halide products. The yields of MCl and $MSnCl_3$ were comparable in Ref. 7. Due to comparable energetics, one might expect similar branching ratios

from the alkaline earth reactions, therefore providing another indirect suggestion that the energetically more favorable MCl_2 product is the dominant one formed.

In all of these reactions of the alkaline earth metals with polyhalides, the inability to determine the identity of the product seriously hampers the data analysis (see also Ref. 33). The systems certainly warrant further study. Magnetic deflection analysis of the products would answer the important question of mono- versus dihalide product.

In conclusion, this series of reactions has provided interesting additions to the kinds of behavior seen in metal-oxidant reactions. More careful study of these systems is warranted, as well as extension of the study to trivalent and transition metals, as has been done in beam chemiluminescence experiments.[34]

References

1. For a recent review of molecular beam reactive scattering studies see J. L. Kinsey, Ch. 6, MTP International Review of Science Physical Chemistry Series One, Vol. 9 Chemical Kinetics (Butterworth, London, 1972).
2. D. O. Ham and J. L. Kinsey, J. Chem. Phys. 53, 285 (1970).
3. R. R. Herm and D. R. Herschbach, J. Chem. Phys. 52, 5783 (1970).
4. D. D. Parrish and R. R. Herm, J. Chem. Phys. 54, 2518 (1971).
5. K. R. Wilson and D. R. Herschbach, J. Chem. Phys. 49, 2676 (1968).
6. R. R. Herm, Ph.D. thesis, Harvard University (1965).
7. S. J. Riley and D. R. Herschbach, J. Chem. Phys. 58, 27 (1973).
8. J. C. Whitehead, D. R. Hardin, and R. Grice, Mol. Phys. 23, 787 (1972) also reported evidence for $ASnCl_3$ product.
9. a. S. Freund, G. A. Fisk, D. R. Herschbach, and W. Klemperer, J. Chem. Phys. 54, 2510 (1971).
   b. H. G. Bennewitz, R. Haerten, and G. Müller, Chem. Phys. Lett. 12, 335 (1971).
10. D. Parrish and R. R. Herm, J. Chem. Phys. 51, 5467 (1969).
11. a. D. L. Hildebrand, J. Chem. Phys. 48, 3657 (1968); 52, 5751 (1970).
    b. J. Berkowitz and J. R. Marquart, J. Chem. Phys. 37, 1853 (1962).
12. T. M. Sloane, S. Y. Tang, and J. Ross, J. Chem. Phys. 57, 2745 (1972).
13. H. S. Johnston, Gas Phase Reaction Rate Theory (Ronald, New York, 1966) pp. 142-145.

14. K. T. Gillen, A. M. Rulis and R. B. Bernstein, J. Chem. Phys. 54, 2831 (1971).

15. A. M. Rulis and R. B. Bernstein, J. Chem. Phys. 57, 5497 (1972).

16. S. J. Riley, Ph.D. Thesis, Harvard University (1970).

17. a. M. G. Inghram, W. A. Chupka, and R. F. Porter, J. Chem. Phys. 23, 2159 (1955).

b. V. A. Medvedev, Russ. J. Phys. Chem. 35, 729 (1961).

c. R. S. Newbury, G. W. Barton, Jr., and A. W. Searcy, J. Chem. Phys. 48, 793 (1968).

18. H. J. Loesch and D. R. Herschbach, J. Chem. Phys. 57, 2038 (1972).

19. J. A. Haberman, K. G. Anlauf, R. B. Bernstein, and F. J. Van Itallie, Chem. Phys. Lett. 16, 442 (1972).

20. W. B. Miller, S. A. Safron, and D. R. Herschbach, Disc. Faraday Soc. 44, 108 (1967) and references cited therein.

21. a. G. H. Kwei, A. N. Lees, and J.A. Silver, J. Chem. Phys. 55 456 (1971).

b. G. A. Fisk, J. D. McDonald, and D. R. Herschbach, Disc. Faraday Soc. 44, 228 (1967).

22. J. Berkowitz, W. Chupka, and D. Gutman, J. Chem. Phys. 55, 2733 (1971).

23. C. D. Jonah, R. N. Zare, and Ch. Ottinger, J. Chem. Phys. 56, 263 (1972).

24. K. Kraus, W. Muller-Dzying, and H. Neuert, Z. Naturforsch. 16a, 1385 (1961).

25. B. L. Earl, R. R. Herm, S.-M. Lin and C. A. Mims, J. Chem. Phys. 56, 867 (1972).

26. For a discussion of translational energy distribution in collision complexes see: S. A. Safron, N. D. Weinstein, D. R. Herschbach, and J. C. Tully, Chem. Phys. Letters 12, 564 (1972) and references cited therein.

27. H. Cruse, Columbia University, private communication.

28. J. Kay and F. M. Page, Trans. Faraday Soc. 60, 1042 (1964).

29. J. R. Airey, E. F. Greene, G. P. Reck, and J. Ross, J. Chem. Phys. 46, 3295 (1967).

30. E. A. Gislason and G. H. Kwei, J. Chem. Phys. 46, 2838 (1967).

31. E. A. taken from that predicted from harpoon model; see Fig. 15 of Ref. 10.

32. A Terenin and R. Tshubarov, Acta Physicochimia U.R.S.S. 7, 1 (1937).

33. S.-M. Lin, Ph.D. Thesis, University of California, Berkeley (1972).

34. J. L. Gole and R. N. Zare, J. Chem. Phys. 57, 5331 (1972).

ACKNOWLEDGMENTS

I consider it a privilege to have worked with Professor Ronald Herm. His availability, scientific insight, and relaxed manner encourage individual personal development which is the essence of graduate education.

I am also lucky to have worked with Shen-Maw Lin. Few people could have been as easy to work with as he was during the long dry spell before the beast finally produced data.

The superb support of both Chemistry Department and LBL facilities made this project possible. Funding of this work by the Atomic Energy Commission is gratefully acknowledged.

My stay at Berkeley produced a large treasure of good friendships, for which I am most thankful.

Special thanks to Boyd Earl for tying up the loose ends and carefully preafrooding this manuscript.

Finally, I would like to thank my wife Amanda and my son Jason, whose incipient birth made the writing of this thesis much more interesting than it needed to be.

TECHNICAL INFORMATION DIVISION
LAWRENCE BERKELEY LABORATORY
UNIVERSITY OF CALIFORNIA
BERKELEY, CALIFORNIA 94720